



Facultad de Ciencias Exactas
Departamento de Ciencias Físicas

TESTEANDO SUPERNOVAS DE TIPO II COMO INDICADORES DE DISTANCIA EN EL INFRARROJO CERCANO

Tesis para optar al grado de Doctor en Astrofísica

Autor:
Ósmar Alí Rodríguez Suárez

Profesor Guía:
Dr. Giuliano Pignata

Comisión Evaluadora:
Dr. Alejandro Clocchiatti
Dr. Francisco Förster
Dr. José Prieto

Santiago, Chile
Junio 2019

RESUMEN

Motivado por las ventajas de observar en longitudes de onda de infrarrojo cercano, en este trabajo investigo a las supernovas de tipo II (SNs II) como indicadoras de distancia en esas longitudes de onda mediante el método de la magnitud fotosférica (PMM). Para el análisis uso fotometría *BVIJH* y espectroscopía óptica de 24 SNs II durante la fase fotosférica. Para corregir la fotometría por efectos de extinción y corrimiento al rojo, calculo las extinciones en bandas anchas total-a-selectiva y las correcciones K hasta $z = 0.032$. Para estimar excesos de color en la galaxias huéspedes, uso el método de la curva color color con $V-I$ versus $B-V$ como combinación de color. Calibro el PMM usando cuatro SNs II en galaxias con distancias medidas con la punta de la rama gigante roja (TRGB). Entre las 24 SNs II, nueve están a $cz > 2000 \text{ km s}^{-1}$, las que uso para construir diagramas de Hubble (DHs). Para explorar más a fondo la precisión de las distancias PMM, incluyo en los DH las cuatro SNs usadas para la calibración y otras dos en galaxias con distancias medidas con Cefeidas o SN Ia. Con un conjunto de 15 SNs II obtengo un valor rms en el DH de 0.13 mag para la banda J , que se compara con el valor rms de 0.15–0.26 para bandas ópticas. Esto refleja los beneficios de medir distancias PMM con fotometría en infrarrojo cercano en vez de fotometría óptica. Con esta evidencia, puedo establecer la precisión de las distancias PMM con la banda J bajo un 10 por ciento con un nivel de confianza de un 99 por ciento.

Para probar el resultado anterior, llevé a cabo una campaña observacional para obtener curvas de luz ópticas y en infrarrojo cercano junto con al menos un espectro óptico por SN. De esta nueva muestra de SNs, seleccioné una submuestra de 24 SNs II ($0.013 < z < 0.033$) las que son ideales para calcular distancias PMM. Complemento esta submuestra con siete SNs II ($z > 0.013$) usadas en Rodríguez et al. (2019). Con este conjunto de 31 SNs II, encuentro que una corrección por el término de color $V-I$ para dar cuenta de la extinción en la galaxia huésped funciona mejor que los excesos

de color obtenidos con el método de la curva color-color. Construyendo DHs, obtengo valores rms de 0.24–0.26 mag con las bandas *BVI* mientras que con *JH* obtengo valores rms de 0.21 mag. Esto refuerza los beneficios de medir distancias PMM con fotometría en infrarrojo cercano en vez de fotometría óptica. Con esta nueva evidencia, puedo establecer la precisión de las distancias PMM con bandas en infrarrojo cercano en $9.7^{+2.6}_{-2.4}$ por ciento con un nivel de confianza del 95 por ciento. Calibrando las distancias PMM con cuatro SNs II en galaxias con distancias TRGB, y usando el DH en la banda *H*, mido una constante de Hubble de $H_0 = 69.8 \pm 1.6(\text{stat}) \pm 2.8(\text{sys}) \text{ km s}^{-1} \text{ Mpc}^{-1}$ (un 4.6 por ciento de error) usando la calibración TRGB de Jang and Lee (2017b).

Para analizar el efecto de los valores atípicos sobre las SNs II como indicadores de distancias con el PMM, en este trabajo presento fotometría óptica e infrarroja de tres SNs II, a saber, SN 2008bm, SN 2009aj y SN 2009au. Estas SNs muestran las siguientes características comunes: signos de interacción temprana del material eyectado con material circunestelar (CSM), colores *B–V* azules, debilidad de líneas metálicas, bajas velocidades de expansión y magnitudes absolutas en la banda *V* 2–3 mag más brillantes que las esperadas para SNs II basado en sus velocidades de expansión. Dos SNs más reportadas en la literatura (SN 1983K y LSQ13fn) comparten propiedades similares a nuestra muestra. Analizando este set de cinco SNs II luminosas con bajas velocidades de expansión (LLEV), encuentro que sus propiedades pueden ser reproducidas asumiendo interacción entre el material eyectado y el CSM que dura entre 3–6 semanas después de la explosión. La contribución de esta interacción al campo de radiación parece ser la componente dominante que determina la debilidad de líneas metálicas observada en los espectros en vez de la metalicidad del progenitor. Basado en simulaciones hidrodinámicas, Encuentro que la interacción del material eyectado con un CSM de $\sim 3.6 M_{\odot}$ puede reproducir las curvas de luz y las velocidades de expansión de la SN 2009aj. Usando datos recogidos por la encuesta CHASE, Estimo un límite superior para la fracción de LLEV SNs II de 1.9–4.7 por ciento de todas las SNs II normales. Con la muestra actual, no es claro si los eventos LLEV presentan un nuevo subtipo de SNs II o si son el extremo de un continuo, mediado por la interacción con un CSM, con el resto de la población de SNs II normales. Basado en la muestra actual, encuentro que las LLEV SNs II no deberían representar un contaminante severo en el uso de SNs II normales como indicadores de distancias con el PMM.

ABSTRACT

Motivated by the advantages of observing at near-IR wavelengths, in this work I investigate Type II supernovae (SNe II) as distance indicators at those wavelengths through the Photospheric Magnitude Method (PMM). For the analysis, I use *BVIJH* photometry and optical spectroscopy of 24 SNe II during the photospheric phase. To correct photometry for extinction and redshift effects, I compute total-to-selective broadband extinction ratios and *K*-corrections up to $z = 0.032$. To estimate host galaxy colour excesses, I use the colour-colour curve method with the $V-I$ versus $B-V$ as colour combination. I calibrate the PMM using four SNe II in galaxies having Tip of the Red Giant Branch (TRGB) distances. Among the 24 SNe II, nine are at $cz > 2000 \text{ km s}^{-1}$, which I use to construct Hubble diagrams (HDs). To further explore the PMM distance precision, I include into HDs the four SNe used for calibration and other two in galaxies with Cepheid and SN Ia distances. With a set of 15 SNe II I obtain a HD rms of 0.13 mag for the *J*-band, which compares to the rms of 0.15–0.26 mag for optical bands. This reflects the benefits of measuring PMM distances with near-IR instead of optical photometry. With this evidence, I can set the PMM distance precision with *J*-band below 10 per cent with a confidence level of 99 per cent.

To test the previous result, I carried out an observational campaign to obtain optical and near-IR light curves of SNe II along with at least one optical spectrum per SN. From this new SN sample, I selected a subsample of 24 SNe II ($0.013 < z < 0.033$) which are suitable to compute PMM distances. I complement this subsample with seven SNe II ($z > 0.013$) used in Rodríguez et al. (2019). With this set of 31 SNe II, I find that a $V-I$ colour-term correction to account for host galaxy extinction works better than the colour excesses obtained with the colour-colour curve method. Constructing Hubble diagrams (HDs), I obtain rms values of 0.24–0.26 mag with *BVI* bands, while with *JH* I obtain a rms of 0.21 mag. This reinforces the benefits of measuring PMM distances with

near-IR instead of optical photometry. With this new evidence, I can set the PMM distance precision with near-IR bands to be $9.7^{+2.6}_{-2.4}$ per cent at a confidence level of 95 per cent. Calibrating the PMM distances with four SNe II in galaxies with Tip of the Red Giant Branch (TRGB) distances, and using the H -band HD, I measure a Hubble constant of $H_0 = 69.8 \pm 1.6(\text{stat}) \pm 2.8(\text{sys}) \text{ km s}^{-1} \text{ Mpc}^{-1}$ (a 4.6 per cent error) using the TRGB calibration of Jang and Lee (2017b).

In order to analyse the effect of outliers over SNe II as distance indicators with the PMM, in this work I present optical and near-IR photometry of three Type II supernovae (SNe II), namely SN 2008bm, SN 2009aj, and SN 2009au. These SNe display the following common characteristics: signs of early interaction of the ejecta with circumstellar material (CSM), blue $B-V$ colours, weakness of metal lines, low expansion velocities, and V -band absolute magnitudes 2–3 mag brighter than those expected for normal SNe II based on their expansion velocities. Two more SNe reported in the literature (SN 1983K and LSQ13fn) share properties similar to our sample. Analysing this set of five luminous with low expansion velocities (LLEV) SNe II, I find that their properties can be reproduced assuming ejecta-CSM interaction that lasts between 3–6 weeks post explosion. The contribution of this interaction to the radiation field seems to be the dominant component determining the observed weakness of metal lines in the spectra rather than the progenitor metallicity. Based on hydrodynamic simulations, I find that the interaction of the ejecta with a CSM of $\sim 3.6 M_{\odot}$ can reproduce the light curves and expansion velocities of SN 2009aj. Using data collected by the CHASE survey, I estimate an upper limit for the LLEV SNe II fraction to be 1.9–4.7 per cent of all normal SNe II. With the current data-set, it is not clear whether LLEV events present a new sub-type of SNe II, or whether they are the extreme of a continuum mediated by CSM interaction with the rest of the normal SN II population. Based on the current sample, I find that the LLEV SNe II should not represent a severe contaminant in the use of normal SNe II as distance indicators with the PMM.

Contents

RESUMEN	i
ABSTRACT	iii
1 INTRODUCTION	1
2 TYPE II SUPERNOVAE AS DISTANCE INDICATORS AT NEAR-IR WAVELENGTHS	4
2.1 INTRODUCTION	4
2.2 OBSERVATIONAL MATERIAL	7
2.2.1 Near-IR Photometric Data	7
2.2.2 Sample of Supernovae	8
2.3 PHOTOSPHERIC MAGNITUDE METHOD	8
2.4 LIGHT CURVE FITS	10
2.5 GALACTIC BROADBAND EXTINCTION	13
2.6 K-CORRECTION	16
2.7 HOST GALAXY BROADBAND EXTINCTION	18
2.8 EXPLOSION EPOCH AND PHOTOSPHERIC VELOCITY	21

2.8.1	Photospheric Velocities	21
2.8.2	Explosion Epoch	23
2.9	APPLYING THE PMM	25
2.9.1	Calibration	25
2.9.2	Hubble Diagrams	28
2.10	DISCUSSION	33
2.10.1	Statistical significance of the result	33
2.10.2	Comparison with other methods	34
2.10.3	Error budget	34
2.10.4	Diminishing systematics	35
2.11	CONCLUSIONS	36
3	AN UPDATED NEAR-IR HUBBLE DIAGRAM FOR TYPE II SUPERNOVAE	37
3.1	INTRODUCTION	37
3.2	OBSERVATIONAL CAMPAIGN	38
3.2.1	Photometric Data	39
3.2.2	Spectroscopic Data	40
3.2.3	Sample of Supernovae	40
3.3	METHODOLOGY	43
3.3.1	Photospheric Magnitude Method	43
3.3.2	Light-curve interpolation	44

3.3.3	Photospheric velocities	44
3.3.4	Explosion epochs	45
3.3.5	Host galaxy colour excess	45
3.3.6	PMM calibration	47
3.4	HUBBLE DIAGRAMS	49
3.4.1	Hubble constant	50
3.4.2	Dependence on $V-I$	51
3.4.3	Second-order dependences	52
3.4.4	Statistical significance of the result	55
3.5	DISCUSSION	56
3.5.1	Error budget	56
3.5.2	Photometric systematics	57
3.6	CONCLUSIONS	57
4	LUMINOUS TYPE II SUPERNOVAE WITH LOW EXPANSION VELOCITIES	59
4.1	INTRODUCTION	59
4.2	SUPERNOVAE AND HOST GALAXIES	60
4.2.1	SN 2008bm	60
4.2.2	SN 2009aj	61
4.2.3	SN 2009au	62
4.3	OBSERVATIONAL MATERIAL	63

4.3.1	Sample of supernovae	65
4.4	PHOTOMETRIC PROPERTIES	65
4.4.1	Peak magnitude versus decline rate	65
4.4.2	Pseudo-bolometric light curves	67
4.4.3	Colour evolution	69
4.4.4	Nickel mass	71
4.5	SPECTROSCOPIC PROPERTIES	72
4.5.1	Early ejecta-CSM interaction	72
4.5.2	Weakness of metal lines	76
4.5.3	Expansion velocities	80
4.6	DISCUSSION	80
4.6.1	A break in the magnitude-velocity relation	80
4.6.2	Interaction of the ejecta with a massive CSM	83
4.6.3	The observed fraction of LLEV SNe II	85
4.6.4	Impact on SNe II as distance indicators	86
4.7	CONCLUSIONS	87
5	CONCLUSIONS	89
	APPENDIX	92
A	MODEL SELECTION	92
B	SN II SPECTRA LIBRARY	94

C	C3 LINEARITY	96
D	SNID EXPLOSION EPOCHS	98
E	THE DISTANCE TO NGC 6946	102
F	AKA CORRECTION	103
G	ADDITIONAL TABLES	106
BIBLIOGRAPHY		118

List of Tables

2.1	SN II sample.	9
2.2	Parameters for the PMM calibration.	26
2.3	Hubble diagram parameters.	32
2.4	Distance precision of different methods.	34
2.5	Error budget for the PMM J -band distances.	35
3.1	Telescopes and instruments	39
3.2	SN sample.	42
3.3	SN II parameters.	46
3.4	PMM parameters using C3 reddenings	49
3.5	Hubble diagram parameters.	51
3.6	PMM parameters using $V-I$ correction.	52
3.7	CMB redshifts and PMM distance moduli.	54
3.8	HD rms for different PMM correction terms.	55
3.9	Error budget for the PMM J -band distances.	57
4.1	SN and host galaxy parameters of the LLEV SN II sample.	61

5.1	Result of SNID simulations.	102
5.2	Observed quantities of SN 1980K and SN 2002hh.	103
5.3	Fits parameters for $\mathcal{R}_{x,(B-V)_A}^G$	105
5.4	Fits parameters for $\mathcal{K}_{x,(B-V)_{AK}}^s$	105
5.5	Fits parameters for $\mathcal{R}_{x,(B-V)_A}^h$	105
5.6	Akaike and Bayesian weights, and evidence ratios for R_x^G , K_x^s/z , R_x^h , and $f_{x,\Delta t}$	107
5.7	Fits parameters for R_x^G , K_x^s/z , and R_x^h	108
5.8	SN II parameters.	109
5.9	CMB redshifts and PMM distance moduli.	110
5.10	SN II spectra library.	111
5.11	SNID templates.	112
5.12	CSP photometry of SN 2008bm.	113
5.13	CSP photometry of SN 2009aj.	114
5.14	CHASE photometry of SN 2009aj.	115
5.15	CSP photometry of SN 2009au.	116
5.16	CHASE photometry of SN 2009au.	117

List of Figures

2.1	Light curves of SNe II used in this work. The estimated explosion epoch of each SN is used as reference time. Orange ticks mark the epochs of the spectroscopy. Solid lines and shaded regions correspond to the light curve fits and its 80 per cent CIs, respectively.	12
2.2	Galactic total-to-selective broadband extinction ratios for <i>BVI</i> (left) and <i>JHK</i> (right) for SNe II as a function of the intrinsic $B-V$ colour, along with residuals. Solid black lines correspond to the polynomial fits, red short-dashed lines correspond to loess regressions to the residuals, while blue long-dashed lines correspond to residuals between the m15mlt3 model (Dessart et al. 2013) and polynomial fits from observations. Gray regions indicate values within one rms, while black dash-dotted lines are the inner fences.	14
2.3	Selective term of the K -correction over redshift for <i>BVI</i> (left) and <i>JHK</i> (right) for SNe II as a function of the intrinsic $B-V$ colour, along with residuals. Solid black lines correspond to the polynomial fits. Red short-dashed lines correspond to loess regressions to the residuals, while blue long-dashed lines correspond to residuals between the m15mlt3 model (Dessart et al. 2013) and polynomial fits from observations. Gray regions indicate values within one rms, while black dash-dotted lines are the inner fences.	17
2.4	Values of $\xi_{S,i}$ for different combinations of c_x and c_y , using $B-V = 0.0$ (top values) and 1.4 (bottom values). Empty spaces indicate superfluous colour combinations. .	20

2.5	Comparison between $E_h(B-V)$ obtained with the spectrum-fitting method (y-axis) and those obtained with the $V-I$ versus $B-V$ C3 method (x-axis). Dashed line represents the one-to-one correlation, with a median offset of -0.01 mag.	22
2.6	Left: values of a_x^* as a function of Δt for $BVIJH$. Black solid lines correspond to the parametric fits. Red dashed lines correspond to loess regressions. Dotted lines indicate values within one rms, while blue dash-dotted lines are the inner fences. Right: ZP_x values for $BVIJH$ derived with four SNe II in galaxies with TRGB distances.	27
2.7	Hubble diagrams for SNe II with PMM distances and CMB redshifts (left) and redshifts corrected for the Virgo and Great Attractor infall (right). Solid lines correspond to Hubble law fits. Residuals are plotted at bottom of each panel.	30
2.8	Hubble diagrams for SNe II with distances computed with the PMM, using the nine SNe II at $cz > 2000 \text{ km s}^{-1}$ (left) and including the six SNe II in galaxies with distance measured with TRGB, Cepheids, or SN Ia (right), where the H_0 values are those computed with the nine SNe II at $cz > 2000 \text{ km s}^{-1}$, and used to convert distances of the six nearest SNe II to redshifts. Solid lines correspond to the Hubble law fits. Residuals are plotted at the bottom of each panel.	31
3.1	Light curves of the SNe II observed during our follow-up campaign. The estimated explosion epoch of each SN is used as reference time. Orange ticks mark the epochs of the spectroscopy. Solid lines and shaded regions correspond to the light curve fits and the 10th–90th percentile ranges, respectively.	41
3.2	Values of a_x^* as a function of Δt for $BVIJH$ for seven SNe presented in this work (coloured symbols) and 19 SNe used in the R19 calibration (gray circles). Black solid lines correspond to the parametric fits. Dotted lines indicate values within one rms.	48

3.3	Hubble diagrams for 31 SNe II with PMM distances corrected for host galaxy colour excess measured with the C3 method (left) and corrected for the $V-I$ colour-term (right). Solid lines correspond to Hubble law fits. Dotted lines indicate values within one rms.	53
4.1	Light curves of SN 2008bm (top), SN 2009aj (middle), and SN 2009au (bottom). Bands and magnitude shifts with respect to the original values are in the legend. Arrows indicate upper limits, while orange ticks mark the epochs of the spectroscopy.	64
4.2	Absolute V -band magnitude at maximum versus V -band decline rate during the plateau (s_2), showing the LLEV SNe II in our set (blue squares) and the normal SNe II in the A14 sample corrected for E_{B-V}^{host} (empty circles). The solid line corresponds to the Gaussian process fit, where dashed lines indicate the 3σ error around the fit.	66
4.3	$BVRI$ (top) and $UVOIR$ (bottom) pseudo-bolometric light curves of the LLEV SNe II in our set (filled symbols) and a selection of normal SNe II that share some of the properties seen on LLEV SNe II (empty symbols).	68
4.4	Top: evolution of the $B-V$ colour, corrected for E_{B-V}^{host} , during the first ~ 100 d of the LLEV SNe II in our set (filled symbols) compared with the normal SNe II in the D18 sample (empty circles). Bottom: evolution of the $B-V$ colour, corrected for E_{B-V}^{host} , during the radioactive tail of SN 1983K (filled triangle) and of normal SNe II from the literature with B - and V -band photometry during 190–350 d since explosion. We also include SN II/In 1998S (top, cyan crosses) and SN II 2010jl (top and bottom, magenta stars) to depict the effect of a long lasting ejecta-CSM interaction over the $B-V$ colour.	70
4.5	Nickel mass versus absolute V -band magnitude at 50 d since explosion, showing the SNe II in the A14 sample (empty circles) and the LLEV SNe II in our set (blue squares). The solid line corresponds to a power law fit, where dashed lines indicate the 3σ error around the fit.	73

4.6	Earliest spectra showing emission lines (top left) along with the first spectra showing Balmer absorptions (bottom left) for our LLEV SN II sample, and zooms around $H\delta$, $H\gamma$, and $H\beta$ (middle panels) and $H\alpha$ (right panels). Epochs on left panels are since the explosion. Spectra were corrected for redshift and colour excess.	74
4.7	Spectra at around 50 d since explosion of the LLEV SNe II in our set. We also include spectra of SN 2002gw and SN 2003bl (gray lines), which have H II region oxygen abundances similar to the LLEV SNe II in our set. Spectra were corrected for redshift and reddening. Values in parenthesis are the epoch since the explosion, the oxygen abundance, and the $B-V$ colour, respectively.	75
4.8	pEW of the Fe II $\lambda 5018$ line at 50 d since explosion, as a function of the oxygen abundance and the $B-V$ colour (corrected for redshift and reddening) at 50 d since explosion, for the LLEV SNe II in our set (blue squares) and the normal SNe II in the A14 sample (circles).	78
4.9	Comparison of the spectrum of SN 2009aj at 39 d since explosion (red line) with a composite spectrum (blue line), which is the sum of the SN 2008M spectrum at 38 d since explosion (gray line) and a blackbody continuum (dashed line).	79
4.10	Evolution of the expansion velocities, measured through the Fe II $\lambda 5169$ minimum absorption lines, of the LLEV SNe II in our set (filled symbols) and the normal SNe II in the G17 sample (empty circles). Black solid and dotted lines correspond to the mean values and standard deviations, respectively, of the expansion velocities in the G17 sample. Orange dashed line correspond to the expansion velocities for SN 1999br.	81
4.11	Absolute V -band magnitude versus expansion velocity, both at 50 d since explosion, showing the LLEV SN II set (blue squares), the normal SNe II in the A14 sample (empty circles), and some luminous SNe II with evidence of ejecta-CSM interaction from the literature (red diamonds). The solid line corresponds to the Gaussian process fit, while dashed lines indicate the 3σ error around the fit. We also plot the location of our SN II model (see Section 4.6.2) without (orange star) and with (circled yellow star) CSM.	82

4.12	Absolute <i>UBVRI</i> light curves (top) and expansion velocities (bottom) of our model with CSM (solid lines) and of SN 2009aj (empty symbols). The same model but without CSM (dashed lines) is displayed for comparison.	84
5.1	Differences between photometric and spectroscopic colours, along with the intrinsic $B-V$ colour. Dashed lines indicate differences within ± 0.1 mag.	96
5.2	Fraction of linear C3s (colourbar) for different colour combinations, along with the median (M) and the rms (R) of the C3 slopes measured from N SNe in our set. Empty spaces correspond to superfluous colour combinations.	97
5.3	Top: $V-I$ versus $B-V$ C3 slopes distribution for the SNe in our set. Red ticks mark the specific slope values, and black dashed line marks the median of the slopes. Bottom: $V-I$ versus $B-V$ diagram showing the 24 SNe II dereddened using host halaxy colour excesses from the C3 method, along with residuals. In both panels, blue dash-dotted lines are the inner fences.	99
5.4	Phase distribution of the templates in our SNID SN II library. The dashed line indicates the average of spectra per bin, while dark gray and light gray regions contain values within ± 1 rms and ± 2 rms around the mean, respectively.	100
5.5	2D histogram of differences between phases since explosion estimated from last non-detection ($t-t_{0,\text{ln}}$) and from SNID ($t-t_0$) _{SNID} versus the r_{lap} parameter (top), and the rms of phase differences versus r_{lap} (bottom).	101

Chapter 1

INTRODUCTION

Type II supernovae (SNe II) are the explosive end of massive stars ($M_{\text{ZAMS}} > 8M_{\odot}$) that retain an important amount of hydrogen in their envelopes at the moment of the explosion. These events, consequence of the gravitational collapse of their iron cores, are characterized by a luminosity comparable to the total luminosity of their host galaxies. This characteristic, along with the high fraction of these events (~ 42 per cent of all SNe Li et al. 2011; Smith et al. 2011), make them interesting objects for distance measurements.

The pionering work of Kirshner and Kwan (1974) marked the beginning of SNe II as distance indicators. Their method, called Expanding Photosphere Method (EPM), allows to measure distances using photometry and spectroscopy during the photospheric phase (the phase between the maximum light and the transition to the radioactive tail) to estimate angular and physical sizes, respectively. Since then, many efforts have been done to improve the EPM performance (e.g., Schmidt et al. 1992; Hamuy 2001; Dessart et al. 2008), along with the development of new methods to measure SN II distances (e.g., “Angular Diameter Determinations of Radio Supernovae and the Distance Scale”; Baron et al. 1995; Hamuy and Pinto 2002; Rodríguez et al. 2014; Pejcha and Prieto 2015; de Jaeger et al. 2015). Among the latter, the Standardized Candle Method (e.g., Hamuy and Pinto 2002) is currently the method most used to measure distance to SNe II (e.g., see Nugent et al. 2006; Poznanski et al. 2009; Olivares E. et al. 2010; D’Andrea et al. 2010; de Jaeger et al. 2015; de Jaeger et al. 2017a; Gall et al. 2018). The SCM allows to estimate distances using photometry and expansion velocities interpolated/extrapolated at 50 days since explosion with a precision of about

12–14 per cent.

Despite the apparent differences between the EPM and the SCM, Kasen and Woosley (2009) showed that the SCM is a recasting of the EPM at 50 days since explosion. Additionally, by means of SN II models, they proposed a generalization of the SCM, which can be applied in any epoch during the photospheric phase. In R14 I investigated the same idea but empirically, calling Photospheric Magnitude Method (PMM) to the SCM generalization. Measuring distances with all expansion velocities available during the photospheric phase decreases observational errors and reduces uncertainties introduced by the interpolation/extrapolation at a certain fiducial epoch.

Most of the distance measurements with the latter methods have been performed with optical photometry. However, observing at near-IR wavelengths has two clear benefits that, in principle, can improve their use as distance indicators:

- (1) Near-IR light is less affected by dust. Methods to measure colour excess due to SNe II host galaxies (e.g., Schmidt et al. 1992; Krisciunas et al. 2009; Olivares E. et al. 2010; Poznanski et al. 2012; R14; Pejcha and Prieto 2015) are still not well established. Therefore, it is propitious to observe at near-IR wavelengths in order to reduce the effect of miscalculation of the colour excess.
- (2) Contamination by metal lines is less severe at near-IR wavelengths. Among the few metal lines identified in the near-IR, we remind: in the *J*-band range there is a feature at $\lambda = 1.2 \mu\text{m}$ possibly due to an Si I multiplet (Valenti et al. 2015), Mg I $\lambda 1.53 \mu\text{m}$ is detected in the *H*-band range (Maguire et al. 2010a; Valenti et al. 2015; Yuan et al. 2016), while in the *K*-band range the Brackett γ is possibly blended with Na I (Dall’Ora et al. 2014). The low number and weakness of metal lines reduce the risk of systematic effects produced by differences in progenitor metallicity (e.g., Dessart et al. 2014; Anderson et al. 2016).

Schmidt et al. (1992) had already pointed out the benefits of measuring distances to SNe II using near-IR photometry. However, at present, there have been very few systematic studies (e.g., Schmidt et al. 1992, Hamuy et al. 2001 for the EPM; Maguire et al. 2010b, de Jaeger et al. 2015 for the SCM). In particular, Maguire et al. (2010b) suggested that it may be possible to reduce the scatter in the Hubble Diagram (HD) to 0.1–0.15 mag (distance precision of 5–7 per cent) using near-IR instead of optical photometry. However, this result is based on the analysis of a set of 12 SNe II, 11

of them at $z < 0.01$, so being highly affected by peculiar velocities. To test this promising result, de Jaeger et al. (2015) applied the SCM to a set of 24 SNe II at $0.01 < z < 0.04$, obtaining an HD rms of 0.28 mag (distance precision of 13 per cent) for the J -band and therefore questioning the improvements of the SCM distance precision using near-IR photometry.

In this work I present an in-depth analysis of the PMM, focused mainly on answering the following question: Are the near-IR bands better than the optical ones to measure PMM distances? What is the PMM distance precision? Can we compute an accurate Hubble constant value using PMM distances? are there SNe II being outliers for the PMM distance measurements? What is the impact of outliers on the PMM distance precision?

This work is organized as follows. In Chapter 2 I present all the tools I develop in order to compute the observables needed to estimate PMM distances, where I test these tools using a small sample SNe II with $BVIJH$ photometry and optical spectroscopy. In Chapter 3 I present a new set of SNe II at $0.013 < z < 0.033$, which I observed during 2015–2018 for the development of this work, and which increases in a factor of 3 the number of SNe II at $z > 0.013$ used in Chapter 2. In Chapter 4 I present the study of SNe II showing interaction of the ejecta with a massive circumstellar medium (CSM) and being 2–3 mag brighter than the expected from their expansion velocities, which could introduce systematics in future works on cosmology using SNe II.

Chapter 2

TYPE II SUPERNOVAE AS DISTANCE INDICATORS AT NEAR-IR WAVELENGTHS

2.1 INTRODUCTION

Type II supernovae (SNe II) are the explosive end of massive stars ($M_{\text{ZAMS}} > 8 M_{\odot}$) that retain an important amount of hydrogen in their envelopes at the moment of the explosion. These events, consequence of the gravitational collapse of their iron cores, are characterized by a luminosity comparable to the total luminosity of their host galaxies, which make them interesting objects for distance measurements.

The pioneering work of Kirshner and Kwan (1974) marks the beginning of the use of SNe II as distance indicators. In their work they applied the Expanding Photosphere Method (EPM, a variant of the Baade-Wesselink method) to two SNe II, using optical photometry and spectroscopy during the photospheric phase (the phase between the maximum light and the transition to the radioactive tail) to estimate angular and physical sizes, respectively. For the first implementation of the EPM, Kirshner and Kwan (1974) assumed SNe II emit like blackbodies. Years after, Wagoner (1981) demonstrated that the flux of SNe II is diluted as a consequence of their scattering-dominated atmospheres, making necessary SN II atmosphere models to quantify that effect and thus to correct derived distances. Since then, the EPM has been applied using different theoretical atmosphere

models (e.g., Eastman et al. 1996; Dessart and Hillier 2005) to an ample number of SNe II (e.g., Schmidt et al. 1992; Schmidt et al. 1994; Hamuy 2001; Dessart et al. 2008; Jones et al. 2009; Bose and Kumar 2014; Gall et al. 2016; Gall et al. 2018), where the typical EPM distance precision is found to be about 15 per cent.

Empirically, Hamuy and Pinto (2002) found a correlation between the bolometric luminosity at 50 d since explosion and the expansion velocity of the photosphere at the same epoch. This is due to the fact that a more energetic explosion corresponds to a more luminous SN with higher envelope expansion velocities. The latter correlation is the basis of the Standardized Candle Method (SCM), which allows to estimate distances using photometry and expansion velocities inter- or extrapolated at 50 d since explosion. The SCM has been applied to several SN II sets (e.g., Nugent et al. 2006; Poznanski et al. 2009; Olivares E. et al. 2010; D’Andrea et al. 2010; de Jaeger et al. 2015; de Jaeger et al. 2017a; Gall et al. 2018), yielding a distance precision about 12–14 per cent.

Despite apparent differences between the EPM and the SCM, Kasen and Woosley (2009) showed that the SCM is a recasting of the EPM at 50 d since explosion. Additionally, by means of SN II models, they proposed a generalization of the SCM, which can be applied in any epoch during the photospheric phase. The same idea was investigated empirically by Rodríguez et al. (2014, hereafter R14), who called it the Photospheric Magnitude Method (PMM) to the SCM generalization. Measuring distances with all expansion velocities available during the photospheric phase, decreases observational errors and reduces uncertainties introduced by the interpolation/extrapolation at a certain fiducial epoch. The PMM distance precision is around 6–11 per cent (R14).

For the EPM, SCM, and PMM, optical spectroscopy is necessary in order to estimate expansion velocities. Since the spectroscopy is more time consuming than photometry, expansion velocities are not always available. For this reason, de Jaeger et al. (2015) proposed a method based solely on photometry to standardize SNe II, known as the Photometric Colour Method (PCM). de Jaeger et al. (2017a) applied the PCM to a SN II sample with redshift up to 0.5, finding that the PCM distance precision is around 17 per cent.

Most of distances measurements with the latter methods have been performed with optical photometry. However, observing at near-IR wavelengths has two clear benefits that in principle can improve

their use as distance indicators:

1. *Near-IR light is less affected by dust.* Methods to measure colour excess due to SNe II host galaxies (e.g., Schmidt et al. 1992; Krisciunas et al. 2009; Olivares E. et al. 2010; Poznanski et al. 2012; R14; Pejcha and Prieto 2015) are still not well established. Therefore, it is propitious to observe at near-IR wavelengths in order to reduce the effect of miscalculation of the colour excess. Moreover, the estimation of a representative extinction curve along the SN II line of sight is still controversial. Assuming the family of extinction curves of Cardelli et al. (1989), some studies are in favour of a Galactic $R_V = 3.1$ (e.g., Pejcha and Prieto 2015), while other authors found results in favour of lower values (Poznanski et al. 2009; Olivares E. et al. 2010; de Jaeger et al. 2015). Since the choice of a certain extinction curve has more impact at optical than at near-IR wavelengths (e.g., Schlafly et al. 2016), it is preferable to perform photometric observations at those wavelengths in order to diminish systematics induced by the assumption of an incorrect extinction curve.

2. *Contamination by metal lines is less severe at near-IR wavelengths.* Among the few metal lines identified in the near-IR, we remind: in the J -band range there is a feature at $\lambda = 1.2 \mu\text{m}$ possibly due to a Si I multiplet (Valenti et al. 2015), Mg I $\lambda 1.53 \mu\text{m}$ is detected in the H -band range (Maguire et al. 2010a; Valenti et al. 2015; Yuan et al. 2016), while in the K -band range the Brackett γ is possibly blended with Na I (Dall’Ora et al. 2014). The low number and weakness of metal lines reduce the risk of systematics effects produced by differences in progenitor metallicity (e.g., Dessart et al. 2014; Anderson et al. 2016).

Schmidt et al. (1992) had already pointed out the benefits of measuring distances to SNe II using near-IR photometry. However, at present, there have been very few systematic studies (e.g., Schmidt et al. 1992, Hamuy et al. 2001 for the EPM; Maguire et al. 2010b, de Jaeger et al. 2015 for the SCM). In particular, Maguire et al. (2010b) suggested that it may be possible to reduce the scatter in the Hubble Diagram (HD) to 0.1–0.15 mag (distance precision of 5–7 per cent) using near-IR instead of optical photometry. However, this result is based on the analysis of a set of 12 SNe II, 11 of them at $z < 0.01$, so being highly affected by peculiar velocities. To test this promising result, de Jaeger et al. (2015) applied the SCM to a set of 24 SNe II at $0.01 < z < 0.04$, obtaining a HD rms of 0.28 mag (distance precision of 13 per cent) for the J -band and therefore questioning the improvements of the SCM distance precision using near-IR photometry.

The goal of this study is to investigate the PMM distance precision using near-IR photometry.

We organize our work as follows. In Section 2.2 we describe the photometric and spectroscopic data. In Section 2.3 we present the PMM developed in R14. In Section 2.4 we develop an algorithm to achieve nonparametric light curve fitting. In section 2.5 and 2.6 we compute Galactic total-to-selective broadband extinction ratios and K -corrections for $BVIJHK$ bands, respectively. In Section 2.7 we compute host galaxy total-to-selective broadband extinction ratios and host galaxy colour excesses through the analysis of colour-colour curves. In Section 2.8 we estimate expansion velocities and explosion epochs. In Section 2.9 we apply the PMM to our SN II sample, constructing HDs for $BVIJH$ bands. Discussion about the PMM distance precision and systematics are in Section 2.10. In Section 2.11 we present our conclusions.

2.2 OBSERVATIONAL MATERIAL

We base our work on data obtained over the course of the Carnegie Type II Supernova Survey (CATS; PI: Hamuy, 2002–2003), a program whose main objective was to study nearby ($z < 0.05$) SNe II. Optical photometry and spectroscopy, along with some near-IR photometry, were obtained with the 1-m Swope, 2.5-m du Pont, and 6.5-m Magellan Baade and Clay telescopes at Las Campanas Observatory. A few additional optical images were obtained with the 0.9-m and 1.5-m telescopes at Cerro Tololo Inter-American Observatory. During the CATS survey, 34 SNe II were observed. Optical photometry and spectroscopy of these SNe II, along with the description of the data reduction, is presented in Galbany et al. (2016) and Gutiérrez et al. (2017), respectively. Next, we briefly summarize the general techniques used to obtain the near-IR photometric data, which will be released in a forthcoming publication.

2.2.1 Near-IR Photometric Data

The near-IR photometric observations were obtained with the JHK bands mounted in the Swope Telescope IR camera and the Wide Field IR Camera on the du Pont Telescope. Images where

processed with a collection of IRAF¹ tasks. These include dark subtraction, flat field correction, sky subtraction, image registration and stacking. Instrumental magnitudes were obtained using the point spread function (PSF) technique, implemented in the SNOOPY² package. The near-IR magnitudes of the reference stars were calibrated using standard star fields obtained soon before or after the target field with an airmass similar to the target field.

2.2.2 Sample of Supernovae

Among the 34 SNe II observed over the course of the CATS survey, we select a subset of 10 SNe II which comply with the following requirements: (1) having at least two photometric measurements in the *BVIJH* bands at 35–75 d since explosion (see Section 2.9), and (2) having at least one measurement of the expansion velocity at an epoch covered by the photometry mentioned in point 1. To this sample, we add 14 SNe II from the literature. Table 2.1 lists our final sample of 24 SNe II, which includes the SN name (Column 1), the name of the host galaxy and its type (Column 2 and 3), the heliocentric SN redshift and its source (Column 4 and 5), host galaxy distance measured with Cepheids, the Tip of the Red Giant Branch (TRGB), or SN Ia (Column 6), Galactic colour excess (Column 7), and references for the data (Column 8). We also use optical and near-IR spectra of SNe II with the purpose of computing total-to-selective broadband extinction ratios (Section 2.5 and 2.7) and *K*-corrections (Section 2.6), and to estimate explosion epochs (Section 2.8.2).

2.3 PHOTOSPHERIC MAGNITUDE METHOD

The absolute magnitude of a SN II during the photospheric phase depends strongly on the temperature and the size of the photosphere (e.g., Kasen and Woosley 2009; R14; Pejcha and Prieto 2015). The latter can be estimated from the velocity of the material instantaneously at the photosphere (hereafter, photospheric velocity, v_{ph}) and the time since the SN explosion epoch t_0 , under the assumption of homologous expansion (e.g., Kirshner and Kwan 1974). R14 found that the time since explosion

¹IRAF is distributed by the National Optical Astronomy Observatory, which is operated by the Association of Universities for Research in Astronomy (AURA) under cooperative agreement with the National Science Foundation.

²SNOOPY is a package for SN photometry using PSF fitting and/or template subtraction developed by E. Cappellaro. A package description can be found at <http://sngroup.oapd.inaf.it/snoopy.html>

SN	Host Galaxy	Host Type [†]	$c z_{\text{helio}}$ (km s ⁻¹)	Source [‡]	μ_{host}^* (mag)	$E_G(B-V)^\diamond$ (mag)	References*
1999em	NGC 1637	SAB(rs)c	800±50	L02	30.21 ± 0.15 ^{⊙,◁}	0.035±0.006	a, b, c, d, e
2002gd	NGC 7537	SABc?	2536±59	here	...	0.058±0.009	a, f, g, h
2002gw	NGC 922	SB(s)cd	3143±31	here	...	0.016±0.003	a, f
2002hj	NPM1G +04.0097	...	7079±20	here	...	0.101±0.016	a, f
2003B	NGC 1097	SB(s)b	1141±52	here	...	0.023±0.004	a, f
2003E	MCG -4-12-4	Sc?	4484±21	here	...	0.041±0.007	a, f
2003T	UGC 4864	SA(r)ab	8368±6	NED	...	0.027±0.004	a, f
2003bl	NGC 5374	SB(r)bc?	4295±41	here	...	0.023±0.004	a, f
2003bn	LEDA 831618	...	3897±25	here	...	0.056±0.009	a, f
2003ci	UGC 6212	Sb	9052±21	here	...	0.051±0.008	a, f
2003cn	IC 849	SAB(rs)cd	5430±162	NED	...	0.018±0.003	a, f
2003hn	NGC 1448	SAcd?	1305±35	S05	31.25 ± 0.07 [⊗]	0.012±0.002	a, d, f, i
2004et	NGC 6946	SAB(rs)cd	40±2	NED	29.39 ± 0.14 [⊗]	0.293±0.047	h, j, k, l, m, n
2005ay	NGC 3938	SA(s)c	850±26	here	...	0.018±0.003	h, o
2005cs	M51a	SA(s)bc	463±3	NED	29.66 ± 0.06 [⊗]	0.032±0.005	h, p, q, r
2008in	M61	SAB(rs)bc	1566±2	NED	...	0.019±0.003	f, o, s
2009N	NGC 4487	SAB(rs)cd	905±21	here	...	0.018±0.003	t
2009ib	NGC 1559	SB(s)cd	1304±162	NED	31.72 ± 0.20 [△]	0.026±0.004	u, v
2009md	NGC 3389	SA(s)c	1308±162	NED	...	0.023±0.004	w
2012A	NGC 3239	IB(s)m	753±162	NED	...	0.027±0.004	x
2012aw	M95	SB(r)b	778±4	NED	29.89 ± 0.07 [⊗]	0.024±0.004	y, z, aa
2012ec	NGC 1084	SA(s)c	1407±162	NED	...	0.023±0.004	bb
2013ej	M74	SA(s)c	657±1	NED	29.95 ± 0.06 [⊗]	0.060±0.010	r, cc, dd, ee
2014G	NGC 3448	I0	1160±84	here	...	0.010±0.002	ff

[†] From NASA/IPAC Extragalactic Database (NED).

[‡] Source of the heliocentric SN redshift. L02: Leonard et al. (2002); S05: Sollerman et al. (2005); here: this work.

* Host galaxy distance moduli measured with Cepheids (⊙), TRGB (⊗) with the Jang and Lee (2017a) calibration, or with SN Ia (△).

◊ Galactic colour excesses from Schlafly and Finkbeiner (2011), with an error of 16 per cent (Schlegel et al. 1998).

◁ Saha et al. (2006) distance was shifted by -0.19 ± 0.13 mag to be consistent with the Riess et al. (2016) calibration (Section 2.9.1).

* (a) Galbany et al. (2016); (b) Hamuy et al. (2001); (c) L02 (d) Krisciunas et al. (2009); (e) Saha et al. (2006); (f) Gutiérrez et al. (2017); (g) Spiro et al. (2014); (h) Faran et al. (2014b); (i) Hatt et al. (2018); (j) Sahu et al. (2006); (k) Maguire et al. (2010a); (l) Tikhonov (2014); (m) Murphy et al. (2018); (n) Anand et al. (2018); (o) Hicken et al. (2017); (p) Pastorello et al. (2006); (q) Pastorello et al. (2009); (r) McQuinn et al. (2017); (s) Roy et al. (2011); (t) Takáts et al. (2014); (u) Takáts et al. (2015); (v) Brown et al. (2010); (w) Fraser et al. (2011); (x) Tomasella et al. (2013); (y) Bose et al. (2013); (z) Dall’Ora et al. (2014); (aa) Rizzi et al. (2007); (bb) Barbarino et al. (2015); (cc) Yuan et al. (2016); (dd) Dhungana et al. (2016); (ee) Bose et al. (2015); (ff) Terreran et al. (2016).

Table 2.1: SN II sample.

works better than the $V-I$ colour (used as a proxy for temperature) to standardize the brightness of SNe II (see Fig. 9 in R14), showing that for a given band x the absolute magnitude in any moment t_i during the photospheric phase, $M_{x,\Delta t_i,v_{\text{ph},i}}$, can be parametrized as

$$M_{x,\Delta t_i,v_{\text{ph},i}} = a_{x,\Delta t_i} - 5 \log \left(\frac{v_{\text{ph},i}}{5000 \text{ km s}^{-1}} \right). \quad (2.1)$$

Here, $\Delta t_i \equiv (t_i - t_0)/(1+z)$ is the elapsed time since the explosion in the SN rest frame at redshift z , and $a_{x,\Delta t_i}$ is a function that can be calibrated empirically. Previously, Kasen and Woosley (2009) found similar results for the SN II brightness standardization, but using SN II models.

With the knowledge of t_0 and a measurement of v_{ph} in any stage of the photospheric phase, we can compute the absolute magnitude at t_i (equation 2.1) and, therefore, compute the SN distance modulus given by

$$\mu_{x,i} = m_{x,i}^{\text{corr}} - a_{x,\Delta t_i} + 5 \log \left(\frac{v_{\text{ph},i}}{5000 \text{ km s}^{-1}} \right), \quad (2.2)$$

$$m_{x,i}^{\text{corr}} = m_{x,i} - A_{x,i}^{\text{G}} - K_{x,i} - A_{x,i}^{\text{h}}. \quad (2.3)$$

Here, $m_{x,i}$ is the apparent magnitude, $A_{x,i}^{\text{G}}$ and $A_{x,i}^{\text{h}}$ are the Galactic and host galaxy broadband extinction, respectively, and $K_{x,i}$ is the K -correction. If more than one measurement of v_{ph} is available, then we compute the distance modulus through a likelihood maximization (see Section 2.9.1).

2.4 LIGHT CURVE FITS

In equation (2.2) we need all quantities at the same epoch. Being more time consuming, spectroscopy is in general less abundant than photometry, so performing photometric interpolations is a reasonable choice. Previous efforts to fit SN II light curves use both parametric and nonparametric methods. Parametric methods assume parametric functions that capture the behaviour of the light curve from early to late stages, where parameters are obtained through least-square minimization (e.g., Olivares E. et al. 2010) or through Bayesian methodologies (e.g., Sanders et al. 2015). Nonparametric methods are based on nonparametric regressions (NPR) like local regressions (e.g., Olivares 2008) and Gaussian processes (e.g., de Jaeger et al. 2017b). Since the light curves of the SNe in our sample are in general well sampled, we prefer to use NPR methods for the light curve fitting, thus avoiding the use of heuristic models.

In this work we make use of `loess`, a NPR method that performs polynomial fits over local intervals along the domain (Cleveland et al. 1992). To perform a `loess` fit, we have to specify: (1) the class of the local polynomial, which can be linear or quadratic, (2) the smoothing parameter, which defines the neighbourhood size around each element of the independent variable, where data can be well approximated by the aforementioned local polynomial, and (3) the distribution of random errors, which can be normal or symmetric (for more details, see Cleveland et al. 1992). We assume the null hypothesis that residuals are normally distributed, which can be checked with a normality test. An optimal value for the smoothing parameter can be obtained from data using the “an” information criterion (AIC, Akaike 1974, see Appendix A). Therefore, to perform a `loess` fit, we only have to decide the local polynomial. We choose a quadratic polynomial in order to give more freedom to the `loess` fitting procedure. When the `loess` routine cannot perform a fit (e.g., for light curves with less than six points), we perform a low-order (linear or quadratic) polynomial fit.

To test whether photometry errors can account for the observed dispersion around the light curve fit, $f_{x,t}^{\text{fit}}$ (in flux units), we compute its log-likelihood given by

$$\ln \mathcal{L} = -0.5 \sum_i \left(\ln(\sigma_{f_{x,i}}^2 + \sigma_{x,\text{int}}^2) + \frac{(f_{x,i} - f_{x,t_i}^{\text{fit}})^2}{\sigma_{f_{x,i}}^2 + \sigma_{x,\text{int}}^2} \right), \quad (2.4)$$

where $f_{x,i}$ and $\sigma_{f_{x,i}}$ are the apparent magnitude and its error in flux units, respectively, and $\sigma_{x,\text{int}}$ is the intrinsic error. If an intrinsic error is necessary to maximize the log-likelihood, then we add it in quadrature to the photometry errors and perform again the light curve fitting. We repeat this process until an intrinsic error is not necessary.

To test the normality of the residuals, we use the Rescaled Moment (RM; Imon 2003) test (see Appendix A). Among all light curves fits, 80 per cent have residuals with RM p -values ≥ 0.05 , for which the hypothesis that residual are normally distributed cannot be rejected within a confidence level (CL) of 95 per cent. For the remaining 20 per cent, light curve fits are still unbiased and consistent, but the confidence interval (CI) of the parameters may be untrustworthy (Doane and Seward 2016). Anyway, in this work, to prevent any shortcoming related to the non-normality of the residuals, we perform simulations to compute CIs.

To compute the CI around a light curve fit, we perform 10^4 simulations varying randomly the photometry according to its error. For each realization we perform a `loess` (or a low-order polynomial)

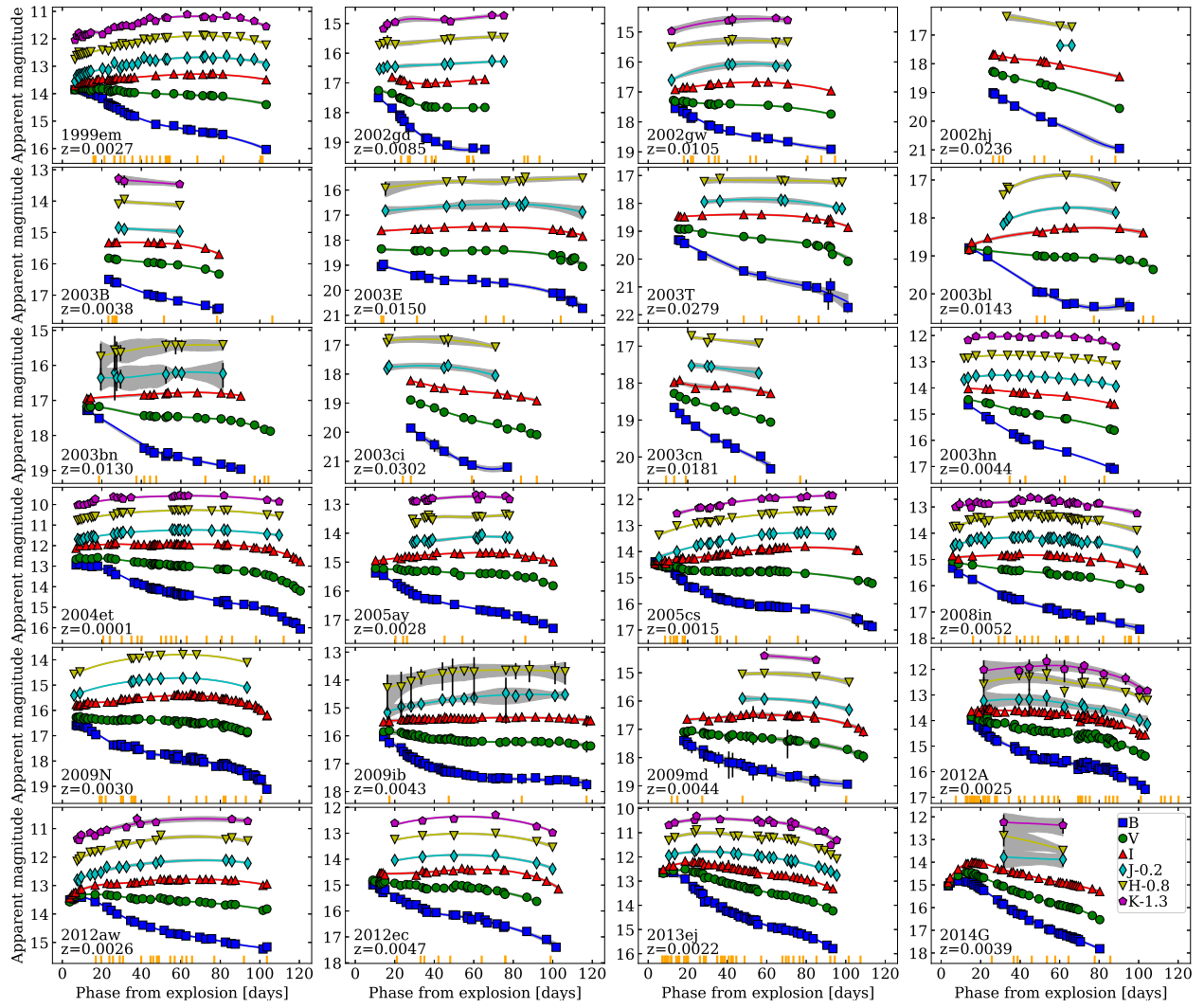


Figure 2.1: Light curves of SNe II used in this work. The estimated explosion epoch of each SN is used as reference time. Orange ticks mark the epochs of the spectroscopy. Solid lines and shaded regions correspond to the light curve fits and its 80 per cent CIs, respectively.

fit, thus obtaining 10^4 simulated light curves per band. These simulations will allow us to compute its probability density function (pdf) at different epochs.

Fig. 2.1 shows results of the aforementioned fitting procedure applied to the SN II light curves used in this work, where solid lines are the `loess` (or low-order polynomial) fits, while shaded regions indicate values between the 10th and the 90th percentile, i.e., the 80 per cent CI.

2.5 GALACTIC BROADBAND EXTINCTION

In equation (2.3), the Galactic broadband extinction in a photometric band x is given by

$$A_{x,i}^G \equiv -2.5 \log \left(\frac{\int d\lambda_0 S_{x,\lambda_0} F_{\lambda_r,i} \lambda_r 10^{-0.4(A_{\lambda_r}^h + A_{\lambda_0}^G)}}{\int d\lambda S_{x,\lambda_0} F_{\lambda_r,i} \lambda_r 10^{-0.4A_{\lambda_r}^h}} \right) \quad (2.5)$$

(Olivares 2008). Here, λ_0 is the wavelength in the observer's frame, $\lambda_r = \lambda_0 / (1+z)$ is the wavelength in the SN rest frame at redshift z , S_{x,λ_0} is the x -band transmission function, $F_{\lambda_r,i}$ is the spectral energy distribution (SED) of the SN at epoch t_i . $A_{\lambda_0}^G$ and $A_{\lambda_r}^h$ are the Galactic and host galaxy monochromatic extinctions, respectively, given by

$$A_{\lambda_0}^G = R_{\lambda_0}^G \cdot E_G(B-V), \quad (2.6)$$

$$A_{\lambda_r}^h = R_{\lambda_r}^h \cdot E_h(B-V), \quad (2.7)$$

where $R_\lambda \equiv A_\lambda / E(B-V)$ is the extinction curve for our Galaxy (R_λ^G) and hosts (R_λ^h), and $E_G(B-V)$ and $E_h(B-V)$ are the Galactic and host galaxy colour excess, respectively.

Since the SED of SNe II evolve with time, we expect that the broadband extinction $A_{x,i}^G$ also evolve with time³. As the SED of SNe II has a blackbody nature, hereafter we use the intrinsic $B-V$ colour (a proxy for temperature) to represent its evolution.

In a previous work, Olivares (2008) computed the dependence of A_V^G on $B-V$. In this work, in order to convert Galactic colour excesses directly into Galactic broadband extinctions suitable for SNe II, we compute the Galactic total-to-selective broadband extinction ratios $R_{x,i}^G$, such that

$$A_{x,i}^G \equiv R_{x,i}^G \cdot E_G(B-V). \quad (2.8)$$

With the purpose of obtaining representative $R_{x,i}^G$ values for a local SN II sample through equation (2.8) and (2.5), we use: (1) a library of dereddened and deredshifted SN II spectra (see Appendix B), (2) colour excesses and redshifts from the following representative ranges: $E_G(B-V) = 0.0-0.36$ mag, $E_h(B-V) = 0.0-0.83$ mag, which were taken from the SN sample reported in R14, and $z = 0.0-0.032$, and (3) an extinction curve to redden the spectra for both our Galaxy and hosts. For

³We remark the difference between a monochromatic extinction A_λ , which is constant for a fixed wavelength λ , and a broadband extinction $A_{x,i}$, which depends on the SED and the x -band transmission function.

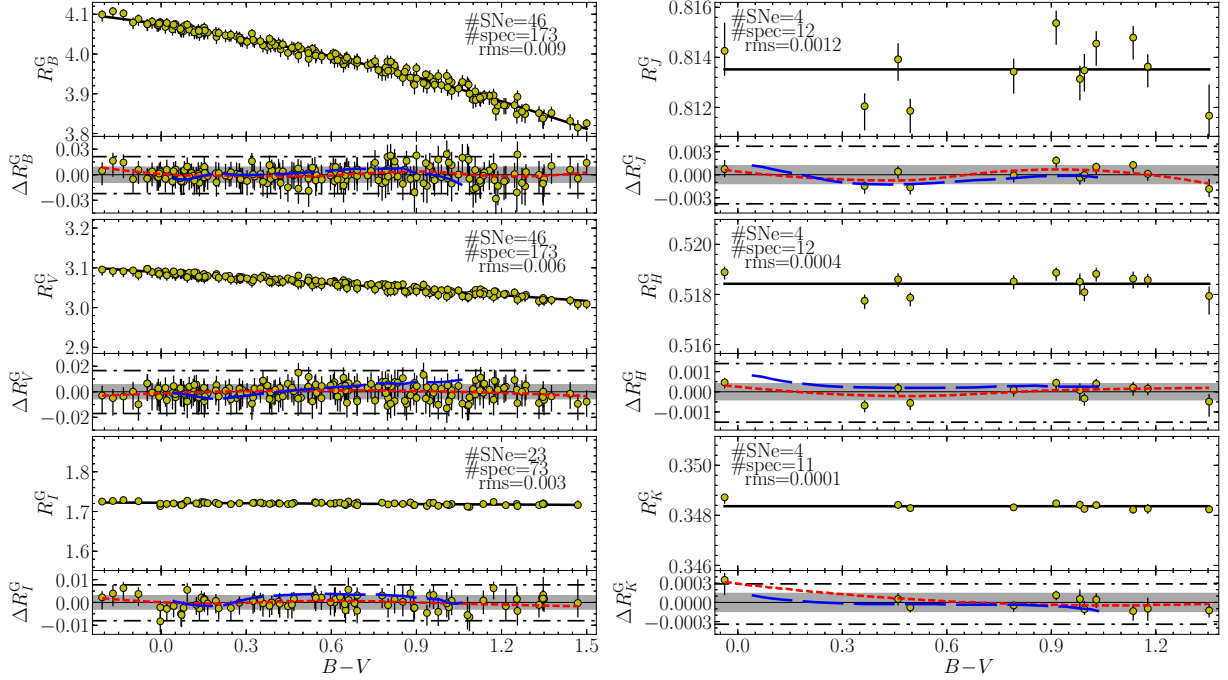


Figure 2.2: Galactic total-to-selective broadband extinction ratios for *BVI* (left) and *JHK* (right) for SNe II as a function of the intrinsic $B-V$ colour, along with residuals. Solid black lines correspond to the polynomial fits, red short-dashed lines correspond to 1oess regressions to the residuals, while blue long-dashed lines correspond to residuals between the m15mlt3 model (Dessart et al. 2013) and polynomial fits from observations. Gray regions indicate values within one rms, while black dash-dotted lines are the inner fences.

the latter, since a representative extinction curve along the line of sight of SNe II is still controversial, we adopt the Fitzpatrick (1999) extinction curve with $R_V = 3.1$. For each spectrum, we perform 10^4 simulations picking randomly values of $E_G(B-V)$, $E_h(B-V)$, and z from the aforementioned ranges, adopting the median as the $R_{x,i}^G$ representative value and the 80 per cent CI as its error.

The left side of Fig. 2.2 shows the $R_{x,i}^G$ values as a function of $B-V$ for *BVI* bands. There is a clear dependence of $R_{B,i}^G$ and $R_{V,i}^G$ on $B-V$. The y-axis scale at the left of Fig. 2.2 is the same in the three panels, so we can see that the redder the band the less the dependence on $B-V$, with $R_{I,i}^G$ being nearly constant. This behaviour is due to the blackbody nature of the SN II SED, where for the longer wavelengths the less the dependence of the SED slope on temperature.

To express the dependence of $R_{x,i}^G$ on $B-V$ we perform polynomial fits. The latter, unlike NPR methods like 1oess, allow to perform corrections in an easy and less time-consuming way (see Appendix C).

To determine the optimal degree for the polynomial fit, we consider two criteria: the AIC and the Bayesian information criterion (BIC, Schwarz 1978). For more details, see Appendix A. Based on evidence ratios (Table 5.6), for the B -, V -, and I -band, the AIC favours degrees ≥ 3 , ≥ 1 , and ≥ 1 , respectively, while the BIC favours degrees between 2 and 6, 1 and 3, and 1 and 4, respectively. Results for both criteria are consistent. By the principle of parsimony (a.k.a. Occam’s razor), we adopt the lowest degrees, i.e., 2, 1, and 1 for the B -, V -, and I -band, respectively. For JHK bands (right of Fig. 2.2) we adopt constant values. Although the small number of near-IR spectra means that the results are not fully statistically robust, we are confident about the negligible dependence of $R_{x,i}^G$ on $B-V$ for JHK bands based on the small rms values we obtained ($\lesssim 0.001$).

Once the optimal polynomial degrees for R_x^G versus $B-V$ are determined, we perform 10^4 bootstrap resampling of the data in order to compute the polynomial fit parameters and their errors, adopting the median as the representative value. Results are summarized in Table 5.7.

The bottom of each panel in Fig. 2.2 shows the residuals of the polynomial fit. To identify possible outliers we use the Tukey (1977) rule, where values below $Q1 - 1.5(Q3 - Q1)$ or above $Q3 + 1.5(Q3 - Q1)$ (known as inner fences, where $Q1$ and $Q3$ are the first and third quartile, respectively) are considered outliers. The few points detected as outliers are consistent with being within inner fences considering their errors, so we do not discard them from the analysis. To analyse possible trends not captured by the polynomial fit, we perform a loess regression (red short-dashed line) to the residuals. Variations in the loess fits are mostly within one rms, meaning that the evolution of R_x^G on $B-V$ can be well represented by a polynomial fit of degree determined with the AIC/BIC. For all bands we obtain RM p -values > 0.05 , which means that we cannot reject the null hypothesis that residual are normally distributed (95 per cent CL). Based on this, we can treat the R_x^G rms error as a normal one.

For comparison, we compute R_x^G for $BVIJHK$ bands using synthetic spectra of the m15mlt3 model of Dessart et al. (2013). Residuals between the m15mlt3 model and polynomial fits from observations (blue long-dashed lines in Fig. 2.2) are mostly contained within one rms.

2.6 K-CORRECTION

The K -correction in a photometric band x is given by

$$K_{x,i} \equiv -2.5 \log(1+z) + K_{x,i}^s, \quad (2.9)$$

$$K_{x,i}^s = 2.5 \log \left(\frac{\int d\lambda_o S_{x,\lambda_o} F_{\lambda_o,i} \lambda 10^{-0.4A_{\lambda_o}^h}}{\int d\lambda_r S_{x,\lambda_o} F_{\lambda_r,i} \lambda_r 10^{-0.4A_{\lambda_r}^h}} \right) \quad (2.10)$$

(Olivares 2008), being $K_{x,i}^s$ the selective term. We proceed in the same way than in Section 2.5, but now the evolving SED is modified by SN host galaxy colour excess and redshift.

As in Section 2.5 we aim for an analytical expression for K_x^s , for which we perform polynomial surface fits as a function of $B-V$ and z . Since $K_x = 0$ for $z = 0$, any z -independent term on the K_x^s polynomial fit is zero. Dividing by z , the polynomial surface to adjust will be of the form

$$K_x^s/z = \sum_{j_1=0}^{\mathcal{O}_{B-V}} \sum_{j_2=0}^{\mathcal{O}_{z,j_1}} a_{j_1,j_2} z^{j_2} (B-V)^{j_1}, \quad (2.11)$$

being \mathcal{O}_{B-V} and \mathcal{O}_{z,j_1} the orders in $B-V$ and z , respectively, and a_{j_1,j_2} the fit parameters.

To determine the orders \mathcal{O}_{B-V} and $\mathcal{O}_{z,i}$, we generate 10^5 spectral samples, where for each sample we assign to each spectrum a random redshift up to 0.032. For each realization, we obtain optimal order values using the AIC/BIC and the principle of parsimony. In all cases we obtain that K_x^s/z depends only on $B-V$, i.e., it is z -independent for $z \leq 0.032$.

Fig. 2.3 shows the K_x^s/z values as a function of $B-V$ for BVI (left) and JHK (right). We perform the same analysis than in Section 2.5. For BVI bands we adopt straight lines, while for JHK bands we fit constant values (see Table 5.6). Results are summarized in Table 5.7. Variations of the loess fits to the residuals are within one rms, meaning that the dependence of K_x^s/z on $B-V$ can be well represented by the polynomial fit of degree determined with the AIC/BIC. For all bands we obtain RM p -values > 0.05 , which means that we cannot reject the null hypothesis that residual are normally distributed (95 per cent CL). Based on the latter, we can treat the K_x^s/z rms error as a normal one.

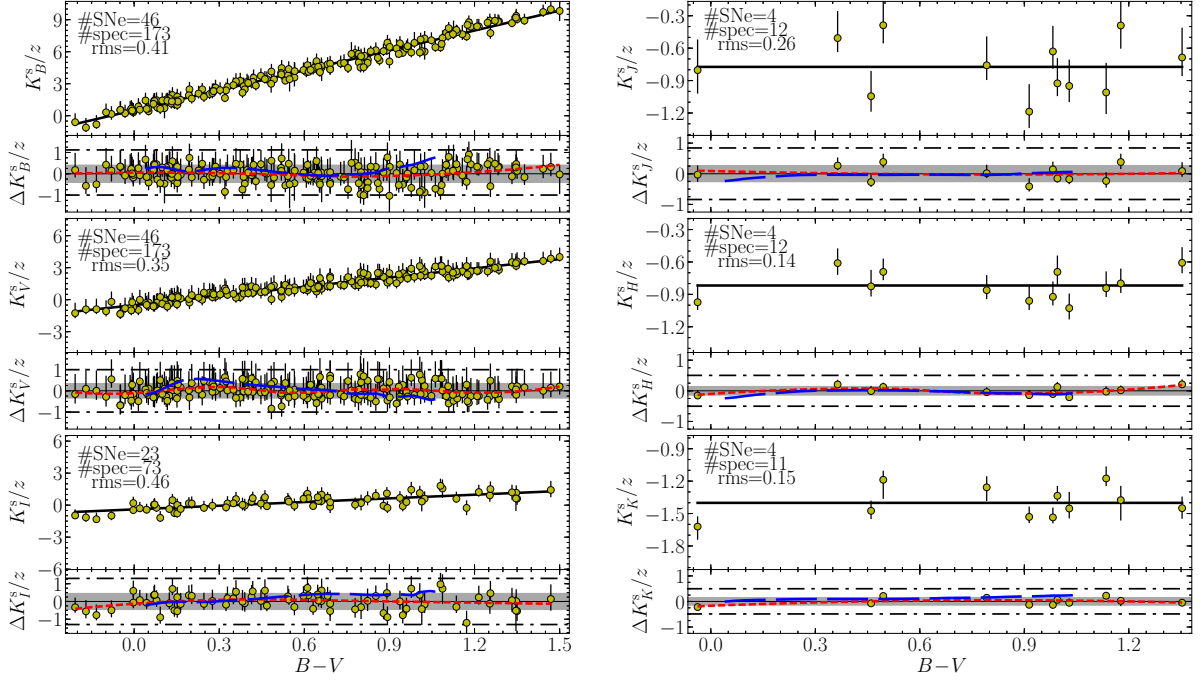


Figure 2.3: Selective term of the K -correction over redshift for BVI (left) and JHK (right) for SNe II as a function of the intrinsic $B-V$ colour, along with residuals. Solid black lines correspond to the polynomial fits. Red short-dashed lines correspond to 1oess regressions to the residuals, while blue long-dashed lines correspond to residuals between the m15mlt3 model (Dessart et al. 2013) and polynomial fits from observations. Gray regions indicate values within one rms, while black dash-dotted lines are the inner fences.

2.7 HOST GALAXY BROADBAND EXTINCTION

In equation (2.3), the host galaxy broadband extinction in a photometric band x is given by

$$A_{x,i}^h \equiv -2.5 \log \left(\frac{\int d\lambda S_{x,\lambda_0} F_{\lambda_0,t} \lambda_0 10^{-0.4A_{\lambda_0}^h}}{\int d\lambda_0 S_{x,\lambda_0} F_{\lambda_0,t} \lambda_0} \right) \quad (2.12)$$

(Olivares 2008). We proceed in the same way than in Section 2.5 and 2.6, but now the evolving SED is modified only by the SN host galaxy colour excess.

Similar to Section 2.5, we define the host galaxy total-to-selective broadband extinction ratios $R_{x,i}^h$, such that

$$A_{x,i}^h \equiv R_{x,i}^h \cdot E_h(B-V). \quad (2.13)$$

The optimum R_x^h versus $B-V$ polynomials and their parameters are summarized in Table 5.7.

R14 showed that for SNe II the $B-V$ versus $V-I$ colour-colour curve (C3) can be used to estimate $E_h(B-V)$ through the method proposed by Natali et al. (1994), which was originally developed to estimate interstellar colour excess for open clusters.

The C3 method states that, under the assumptions that (1) the C3 can be well-represented by a straight line, and (2) all SNe II have the same C3 (which means the same slope and intercept), the host galaxy colour excess can be estimated with the formula

$$E_{h,i}(B-V) = \frac{1}{R_{c_x,i}^h} \frac{n_{S,i} - n_{S,zp}}{\gamma_{S,i} - M\{m_S\}} \quad (2.14)$$

(e.g., Munari and Carraro 1996; R14). Here, $S \equiv \{c_x, c_y\}$ indicates the colours used as x - and y -axis in the colour-colour diagram, corrected for Galactic colour excess and K -correction. $M\{m_S\}$ is the median of a set of SN II C3 slopes $\{m_S\}$, $n_{S,i} = c_{y,i} - M\{m_S\} \times c_{x,i}$ and $n_{S,zp}$ are the y -intercept of the C3 linear fit using a fixed slope $M\{m_S\}$ and that of the SN II less affected by colour excess, respectively. $R_{c,i}^h = R_{x_1,i}^h - R_{x_2,i}^h$ for a colour $c = x_1 - x_2$, and $\gamma_{S,i} = R_{c_y,i}^h / R_{c_x,i}^h$ is the slope of the reddening vector. The subindex i in equation (2.14) denotes the dependence of $R_{x,i}^h$ on the intrinsic $B-V$, so equation (2.14) must be evaluated separately at each point of the C3. In principle, one colour-colour observation is enough to estimate the colour excess, however more observations allow to check internal consistency and reduce observational errors.

The C3 method relies strongly on the aforementioned two assumptions. In a previous work, R14 assumed the linearity of C3s based on the blackbody nature of the SED of SNe II during the photospheric phase, while assumption 2 was adopted based on the dependence of the emergent flux mainly on temperature displayed by SN II atmosphere models (e.g., Eastman et al. 1996; Jones et al. 2009). In this work we show that C3s can indeed be expressed as straight lines for several colour combinations (see Appendix C). Therefore, the major source of systematics comes from assumption 2. There are indeed some effects, like the line blanketing, that modify the SED continuum shape. In addition, differences in photometric systems (*S*-correction; Stritzinger et al. 2002) are expected to produce further changes on C3 parameters. Therefore it is propitious to search for a colour combination where the effect of a colour excess on a C3 is greater than the effect of systematics.

An analysis of the effect of systematics on the C3 *y*-intercept is beyond the scope of this work because it requires an ample set of unreddened SNe II. However, the effect of systematics on C3 slopes and its consequent effects on the $E_h(B-V)$ estimation through the C3 method can be quantified in a simple way.

The presence of dust along the line of sight produces a vertical displacement of the C3 (for a graphical representation, see R14) where, following equation (2.14), the magnitude of the displacement and its rms error are

$$|n_{S,i} - n_{S,zp}| = E_h(B-V) \cdot R_{c_x,i}^h \cdot |\gamma_{S,i} - M\{m_S\}|, \quad (2.15)$$

$$\text{rms}(|n_{S,i} - n_{S,zp}|) \approx E_h(B-V) \cdot R_{c_x,i}^h \cdot \text{rms}\{m_S\}, \quad (2.16)$$

respectively. In equation (2.16), we do not include the error induced by errors in $\gamma_{S,i}$, which is lower than 17 per cent of the uncertainty induced by the error in $M\{m_S\}$. In order to find the colour combination that maximizes the dust effect (equation 2.15) and minimizes its error (equation 2.16), we define the quantity (a signal-to-noise ratio)

$$\xi_{S,i} \equiv \frac{|n_{S,i} - n_{S,zp}|}{\text{rms}(|n_{S,i} - n_{S,zp}|)} \approx \frac{|\gamma_{S,i} - M\{m_S\}|}{\text{rms}\{m_S\}}. \quad (2.17)$$

Therefore, the most appropriate colour set *S* to compute $E_h(B-V)$ with the C3 method is one that maximizes $\xi_{S,i}$.

Fig. 2.4 shows the $\xi_{S,i}$ values for all possible independent colours combinations with the *BVIJH*

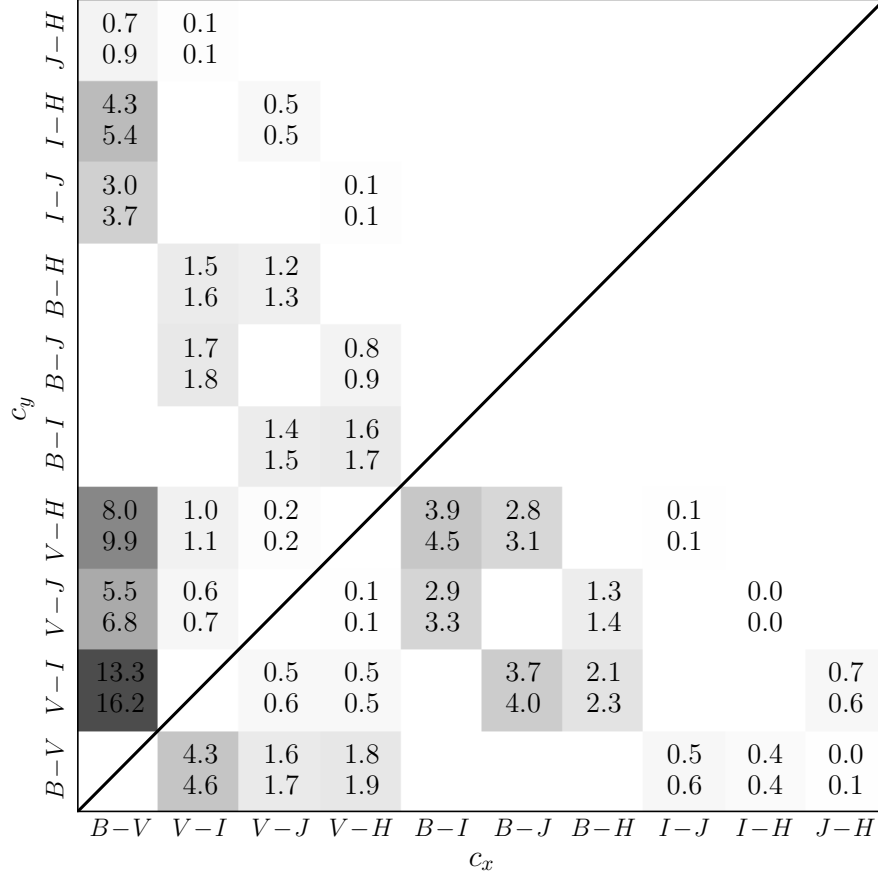


Figure 2.4: Values of $\xi_{S,i}$ for different combinations of c_x and c_y , using $B-V = 0.0$ (top values) and 1.4 (bottom values). Empty spaces indicate superfluous colour combinations.

bands, using the $M\{m_S\}$ and $\text{rms}\{m_S\}$ values computed with our SN II sample (see Appendix C), and using $B-V = 0.0$ and 1.4, which are typical colours at the start and end of the photospheric phase, respectively. We do not include the K -band in this analysis because of the scarcity of SNe II with photometry in that band. The best colours combinations, independent of the intrinsic $B-V$, are those involving $B-V$, with $V-I$ versus $B-V$ the best. For this combination we obtain $M\{m_S\} = 0.45 \pm 0.07$. We remark that colours combinations that do not include the B -band have $\xi_{S,t} \lesssim 1.0$, which indicates that the noise induced by intrinsic differences of C3 slopes is greater than the effect of host galaxy dust, and therefore those combinations are not suitable for $E_h(B-V)$ measurement through the C3 method. We point out that colours combinations under the diagonal correspond to those above the diagonal but with the axes exchange. In principle they give the same information. However, by construction, they maximize displacement in x -axis instead of y -axis.

To compute the pdf of $n_{S,zp}$ for $S = \{B-V, V-I\}$, we use the data of SN 2003bn and SN 2013ej, which are affected by a negligible host galaxy colour excess (R14), maximizing the likelihood of a straight line with slope 0.45 ± 0.07 . With this process, we obtain a pdf with median of 0.107 mag and rms = 0.053 mag. Since the RM p -value for the latter distribution is > 0.05 , we treat it as a normal distribution.

To estimate $E_h(B-V)$, we use equation 2.14 and each point in the $V-I$ versus $B-V$ colour-colour plot. The pdf of $E_h(B-V)$ is obtained in a similar way than the pdf of $n_{S,zp}$, but maximizing the likelihood of a constant-only model. We include in the final pdf of $E_h(B-V)$ the error induced by errors on $n_{S,zp}$ and $M\{m_S\}$. Median values and errors of $E_h(B-V)$ are listed in Column 2 of Table 5.8. For our SN set we obtain $E_h(B-V)$ rms errors between 0.082 and 0.128 mag, with a median of 0.097 mag.

Fig. 2.5 shows the comparison between host galaxy colour excesses computed with $S = \{B-V, V-I\}$ with those obtained by Olivares E. et al. (2010), $E_h(B-V)_{\text{spec}}$ (Column 5 of Table 5.8), which are based on the fit between observed spectra and SN II models. We measure a median offset of -0.01 mag, meaning that our estimations of $E_h(B-V)$ are slightly lower than those estimated by Olivares E. et al. (2010). Both methods are consistent within ± 0.05 mag.

2.8 EXPLOSION EPOCH AND PHOTOSPHERIC VELOCITY

The explosion epoch and the photospheric velocity are, under the assumption of homologous expansion, the unique parameters determining the actual size of the photosphere (Kirshner and Kwan 1974).

2.8.1 Photospheric Velocities

The most widely used method to estimate SN photospheric velocities consists of measuring the blueshift of P Cygni absorption minima in SN spectra (Kirshner and Kwan 1974; Eastman and Kirshner 1989). Weak lines, like those from Fe II species, are typically used under the assumption

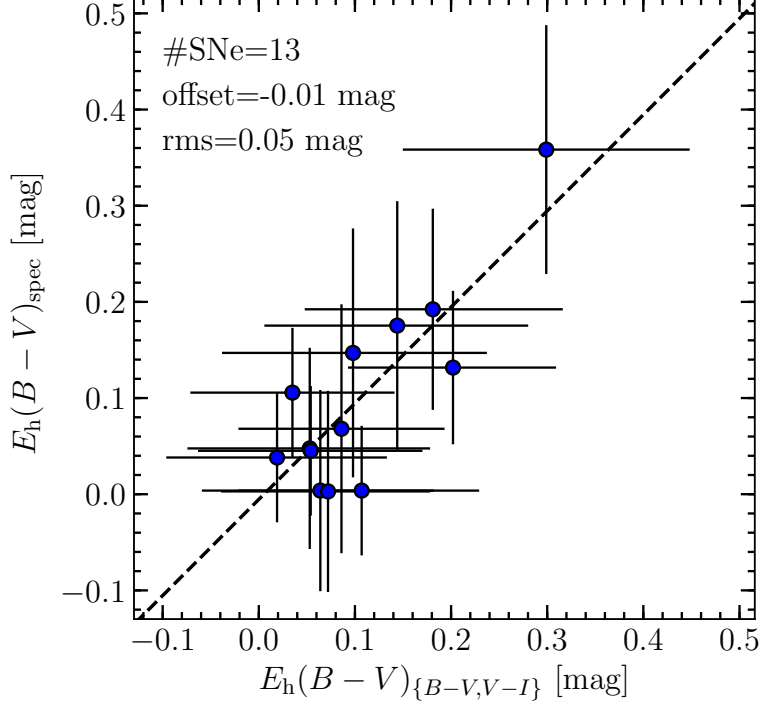


Figure 2.5: Comparison between $E_h(B-V)$ obtained with the spectrum-fitting method (y-axis) and those obtained with the $V-I$ versus $B-V$ C3 method (x-axis). Dashed line represents the one-to-one correlation, with a median offset of -0.01 mag.

that they are formed near the photosphere (e.g., Leonard et al. 2002). A more confident method to estimate photospheric velocities is through the cross-correlation technique (Hamuy et al. 2001; Takáts and Vinkó 2012), where observed spectra are compared to those from SN models which have known photospheric velocities. The application of the latter method is beyond the scope of this work, therefore we will use velocities derived from the Fe II $\lambda 5169$ line absorption minima as a proxy for the photospheric velocity.

To estimate Fe II $\lambda 5169$ absorption minima with appropriate errors, we have to consider the uncertainties induced by the noise and spectral resolution ($\Delta\lambda$) of each spectrum, and also by the endpoints we choose for the line profile.

We estimate the noise on the Fe II $\lambda 5169$ line profile of each spectrum performing a `loess` fit and then removing it to the observed line profile. Then we generate 10^4 simulated line profiles, varying randomly the noise over the `loess` fit, wavelengths within $\Delta\lambda$, and endpoints. For each realization we apply a `loess` fit, registering the minimum value. The output of this process is a distribution of

absorption minima, which we convert to velocities using the relativistic Doppler equation. With this process we obtain typical v_{ph} rms errors between 30 and 230 km s^{-1} , with a median of 76 km s^{-1} .

Photospheric velocities are estimated from spectroscopic data, corrected for the SN heliocentric redshift.

In some cases, SN II spectra shows narrow emission lines as result of a superposed H II region at the SN position. These narrow lines allow a good estimation of the SN heliocentric redshift, under the assumption that the SN is spatially close to the H II region (e.g., Anderson et al. 2014a). When those lines are not present in the SN spectra, the heliocentric redshift of the host galaxy is used as a proxy for the SN heliocentric redshift. However, since most of the SNe II in our set explode in spiral galaxies, the SN heliocentric redshift has a component due to the galaxy rotation. Anderson et al. (2014a) computed heliocentric redshifts of 72 SNe II using H II region narrow emission lines, and comparing with heliocentric redshifts of the host galaxy nucleus, they obtained a zero-centred distribution with a rms of 162 km s^{-1} , which is attributed to the galaxy rotation effect.

In our sample, 11 SNe II (SN 2002gd, SN 2002gw, SN 2002hj, SN 2003B, SN 2003E, SN 2003bl, SN 2003bn, SN 2003ci, SN 2005ay, SN 2009N, and SN 2014G) show H II region narrow emission lines in the spectra, which we use to estimate the heliocentric redshift. Another six SNe (SN 2003T, SN 2004et, SN 2005cs, SN 2008in, SN 2012aw, and SN 2013ej) exploded within nearly face-on galaxies, in which case we adopt the redshift of the host galaxy nucleus. For SN 1999em we adopt the value from Leonard et al. (2002), and for SN 2003hn we use the average of the Na I D velocities measured by Sollerman et al. (2005). The remaining five SNe (SN 2003cn, SN 2009ib, SN 2009md, SN 2012A, and SN 2012ec) did not occur within nearly face-on galaxies, and do not show H II region narrow emission lines in the spectra. For those cases we adopt the redshift of the host galaxy nucleus, with an error of 162 km s^{-1} (that we assume normal) to take into account the host galaxy rotational velocity. Adopted SN heliocentric redshifts are listed in Table 2.1.

2.8.2 Explosion Epoch

The SN explosion epoch can be estimated by means of photometric information; it can be constrained between the last non-detection t_{ln} and the first detection t_{fd} (e.g., Nugent et al. 2006; Poznanski

et al. 2009; D’Andrea et al. 2010; R14; Valenti et al. 2016), or estimated through a polynomial fit to the rise-time photometry when it is available (e.g., González-Gaitán et al. 2015; Gall et al. 2015). The spectroscopy of a SN can also provide information about its explosion epoch by means of the comparison with other spectra of SNe with explosion epoch estimated through photometric information (e.g., Anderson et al. 2014b; Gutiérrez et al. 2017).

Column 4 and 5 of Table 5.8 lists the t_{ln} and t_{fd} values of the SNe in our set, respectively. The explosion epochs for our set are typically constrained within 14 d using photometric information, which is twice the range suggested by R14 (namely, 7 d) to reduce errors induced by t_0 errors over PMM distances. We need, therefore, to include spectroscopic information in order to better constrain the explosion epochs.

As was done by Anderson et al. (2014b) and Gutiérrez et al. (2017), to estimate t_0 we use optical spectroscopy along with the Supernova Identifier code (SNID; Blondin and Tonry 2007), which finds by cross-correlation the spectra from its SN library that are more similar to the input spectrum. For a good estimation of t_0 with SNID, we need a library with spectra of an ample amount of SNe II that sample the high spectral diversity displayed by SNe II (e.g., Gutiérrez et al. 2017) and with t_0 constrained by photometric information. In this work, we compile optical spectroscopy of 59 SNe II with t_0 constrained within 10 d (for more details, see Appendix D).

To estimate the explosion epoch of a given SN (SN_{input}) with N spectra ($\{\text{spec}\}$) through SNID and using our SN II templates library, we perform the following procedure:

1. We run SNID using as input the N spectra of SN_{input} earlier than 40 d since the first detection. The SNID output for each spectrum is a list with the best-matching templates, their phase since explosion, and their r_{lap} parameter (which indicates the strength of the correlation).
2. We convert phases since explosion to explosion epochs (since we know the phase of each SN_{input} spectrum). The associated errors are derived from the r_{lap} values through a procedure described in Appendix D .
3. From each of the N lists, we select the first ten best-matching templates with $r_{\text{lap}} > 5.0$, compiling them in a unique list. From this list, we extract a sublist for each of the M best-

matching SNe (SN_{bm}). With each of the M sublist, we compute the SN_{in} explosion epoch as the average, taking the standard deviation as the associated error, and including the respective explosion epoch error of the SN_{bm} through a Monte Carlo error propagation. If a spectrum gives a median t_0 greater than 40 d, then we remove it from the analysis.

4. After that, we compute the likelihood $\mathcal{L}(t_0|\{\text{spec}\})$ with the M results, including an error of 4.1 d which is the rms obtained from the comparison between explosion epochs constrained with photometric information and those derived with SNID (see Appendix D).
5. Finally, we obtain the posterior pdf of t_0 , $p(t_0|\{\text{spec}\})$, combining $\mathcal{L}(t_0|\{\text{spec}\})$ with the uniform prior on t_0 , $p(t_0)$, provided by photometric information, i.e.,

$$p(t_0|\{\text{spec}\}) \propto \mathcal{L}(t_0|\{\text{spec}\})p(t_0). \quad (2.18)$$

Table 5.8 lists the medians and rms values of the explosion epochs obtained with SNID and without any prior on t_0 (Column 7), and the median of $p(t_0|\{\text{spec}\})$ of each SN along with the 80 per cent CI (Column 8).

2.9 APPLYING THE PMM

Once all observables required for the PMM are available, the next step is to prepare the data before applying the method. As was mentioned in Section 2.4, we interpolate photometry to the epochs of the photospheric velocities. Since we want to study the PMM distance precision at different photometric bands, i.e., changing only the photometry, we use epochs where spectroscopy is covered simultaneously by optical and near-IR photometry. In the case of SN 2002hj, it does not have spectroscopy covered by J -band photometry, so we interpolate photospheric velocities (using `loess`) and $BVIH$ photometry to the epochs of J -band photometry.

2.9.1 Calibration

For the PMM calibration, we express $a_{x,\Delta t}$ as

$$a_{x,\Delta t} = \text{ZP}_x + a_{x,\Delta t}^*, \quad (2.19)$$

x	$f_{x,\Delta t} = c_x \cdot \Delta t / (100 \text{ d}^{-1})$			zero-point	
	c_x	rms	$p(\text{RM})$	ZP_x	rms
B	$3.87^{+0.32}_{-0.26}$	0.09	0.05	$-19.51^{+0.52}_{-0.52}$	0.27
V	$2.78^{+0.31}_{-0.22}$	0.09	0.32	$-20.03^{+0.39}_{-0.39}$	0.19
I	$2.22^{+0.34}_{-0.24}$	0.10	0.70	$-20.36^{+0.23}_{-0.23}$	0.15
J	$2.13^{+0.29}_{-0.27}$	0.10	0.51	$-20.64^{+0.12}_{-0.12}$	0.10
H	$2.05^{+0.28}_{-0.28}$	0.09	0.92	$-20.77^{+0.09}_{-0.09}$	0.07

Parameters are valid for $35 \text{ d} < \Delta t < 75 \text{ d}$. Errors are the 99 per cent CI.

Table 2.2: Parameters for the PMM calibration.

where ZP_x is the zero-point of the PMM in the x -band, and $a_{x,\Delta t}^*$ is a function that represents the dependence of $a_{x,\Delta t}$ on Δt (without the constant term).

To estimate the evolution of $a_{x,\Delta t}^*$ with Δt , we use the $a_{x,\Delta t_i}^*$ values of the SNe in our set with two or more v_{ph} measurements during the photospheric phase. For each SN, the $a_{x,\Delta t_i}^*$ values are given by

$$a_{x,\Delta t_i}^* = m_{x,i}^{\text{corr}} + 5 \log \left(\frac{v_{\text{ph},i}}{5000 \text{ km s}^{-1}} \right) + \delta_{\text{SN}}, \quad (2.20)$$

where δ_{SN} is an additive term to normalize the $a_{x,\Delta t_i}^*$ values of each SN to the same scale. Based on the definition given in R14, the dependence of $a_{x,\Delta t}^*$ on Δt has the form

$$a_{x,\Delta t}^* = f_{x,\Delta t} - 5 \log \left(\frac{\Delta t}{100 \text{ d}} \right). \quad (2.21)$$

We express the dependence of $f_{x,\Delta t}$ on Δt through polynomials. We use the AIC/BIC to determine the optimum polynomial order for $f_{x,\Delta t}$ and the values of δ_{SN} , while to estimate the time range of applicability of the PMM, we group the $f_{x,\Delta t_i}$ values in bins of width 10 d and then we compute the rms of the points in each bin. We found that rms values are lower in a range 35–75 d since the explosion. Among all optimum orders for *BVIJH* bands (see Table 5.6), we select the order that the different bands have in common, i.e., order one. With this, we prevent that differences in the $\text{rms}(f_{x,\Delta t})$ value for different bands are due to differences in the order of the polynomial fit. To estimate error in the parameters, we perform 10^4 bootstrap resampling. Table 2.2 lists $f_{x,\Delta t}$ fits parameters for *BVIJH* bands.

The left half of Fig. 2.6 shows the values of $a_{x,\Delta t_i}^*$ as a function of Δt_i for *BVIJH* bands. The variation of the loess fits (red dashed lines) are within one rms (black dotted lines), which means that

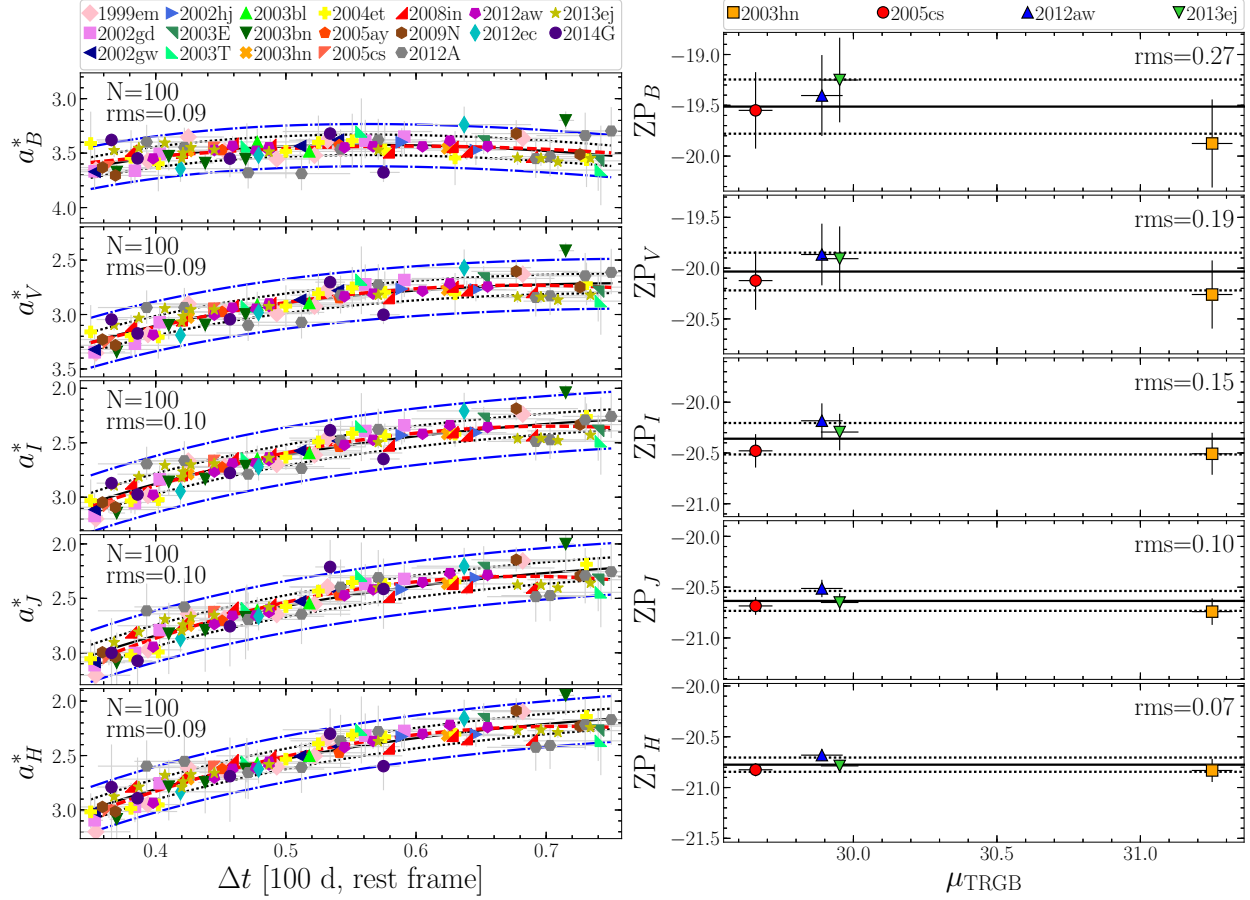


Figure 2.6: Left: values of a_x^* as a function of Δt for BV_{IIH} . Black solid lines correspond to the parametric fits. Red dashed lines correspond to 1oess regressions. Dotted lines indicate values within one rms, while blue dash-dotted lines are the inner fences. Right: ZP_x values for BV_{IIH} derived with four SNe II in galaxies with TRGB distances.

polynomial fits we adopted capture almost all the dependence on Δt . The PMM zero-points can be obtained using a sample of SNe II at known distances where, for each SN, we have

$$ZP_x^{\text{SN}} = \mu_x^* - \mu_{\text{host}}^{\text{SN}}. \quad (2.22)$$

Here, $\mu_{\text{host}}^{\text{SN}}$ is the SN host galaxy distance modulus and μ_x^* is the SN pseudo-distance modulus. The latter, for each measurement of v_{ph} at time t_i , is defined similar to equation 2.2 but with $a_{x,\Delta t_i}^*$ instead of $a_{x,\Delta t_i}$, i.e.,

$$\mu_{x,i}^* = m_{x,i}^{\text{corr}} - a_{x,\Delta t_i}^* + 5 \log \left(\frac{v_{\text{ph},i}}{5000 \text{ km s}^{-1}} \right). \quad (2.23)$$

The pdfs of $\mu_{x,i}^*$ are obtained through equation 2.23 using the pdfs of the observables for each photospheric velocity epoch. Finally, we combine the pdfs of $\mu_{x,i}^*$ in a unique μ_x^* pdf maximizing the likelihood (equation 5.1) for a constant-only model.

To compute accurate ZP_x values, we need SNe II in galaxies with distances measured with the best possible precision. Among the SNe that we compiled from the literature, there are only three (SN 1999em, SN 2003hn, and SN 2012aw) in galaxies with distances measured through Cepheid, and five (SN 2003hn, SN 2004et, SN 2005cs, SN 2012aw, and SN 2013ej) in galaxies with distances measured with TRGB. Cepheid distances for the hosts of SN 1999em and SN 2012aw were reported by Saha et al. (2006), while Riess et al. (2016) reported the Cepheid distance of the host of SN 2003hn. Comparing Cepheid distances of six galaxies in common between the two publications (NGC 1365, NGC 3370, NGC 3982, NGC 4536, NGC 4639, and NGC 5457) we found that Cepheid distances reported by Saha et al. (2006) are, on average, 0.19 mag greater than those reported by Riess et al. (2016), showing a rms of 0.13 mag. The latter could indicate a systematic difference between the two calibrations, which can introduce an undesirable noise on the ZP_x estimation if we rescale Saha et al. (2006) distances to the Riess et al. (2016) calibration. For this reason, we decide to use only SNe in galaxies with TRGB distances, that can be homogenized to the Jang and Lee (2017b) calibration, which is based on the distance to the Large Magellanic Cloud and NGC 4258. Recalibrated TRGB distances are listed in Column 6 of Table 2.1. From these five SNe II, we discard SN 2004et since the TRGB distance of its host is at least 0.59 mag higher compared to the distances we compute for SN 2004et and two other SNe II that exploded in the same galaxy (see Appendix E).

The right half of Fig. 2.6 shows the ZP_x^{SN} values for *BVIJH*. As in the case of μ_x^* , the pdf of ZP_x is obtained combining the pdfs of ZP_x^{SN} . Median values, 99 per cent CI, and rms values for ZP_x are summarized in Table 2.2.

Once the PMM zero-points are computed, we can estimate the distance modulus for each band as $\mu_x = \mu_x^* - ZP_x$. Median values, 80 per cent CI, and rms values for μ_x are summarized in Table 5.9, where we include the TRGB zero-point systematic error of 0.058 mag (Jang and Lee 2017b).

2.9.2 Hubble Diagrams

To investigate the PMM distance precision, we construct HDs. We convert heliocentric host galaxy redshifts to cosmological ones using as reference the cosmic microwave background (CMB) dipole

(Fixsen et al. 1996). Redshift errors are dominated by peculiar velocities, with a rms of 382 km s^{-1} for local SN Ia host galaxies ($z < 0.08$, Wang et al. 2006), followed by the error in the determination of the Local Group velocity (rms of 187 km s^{-1} , Tonry et al. 2000). CMB redshifts and their rms errors are listed in Table 5.9.

Taking into account the pdfs of the pseudo-distance moduli (μ_x^*) and the pdfs of the CMB redshifts (cz_{CMB}), we compute the Hubble diagram intercept ($a_{\text{HD},x}$) maximizing the likelihood (equation 5.1), where the model for the pseudo-distance modulus is given by the Hubble law

$$\mu_x^* = a_{\text{HD},x} + 5 \log(cz_{\text{CMB}}). \quad (2.24)$$

The left half of Fig. 2.7 shows HDs for *BVIJH* bands, using PMM distances for all SNe in our set. The rms, greater than 0.5 mag for all bands, is mostly produce by peculiar velocities of host galaxies at low redshift. In fact, the median redshift of the host galaxies in the HD is 1528 km s^{-1} , where a redshift error of 382 km s^{-1} translates into a magnitude error of 0.54 mag. Indeed, if we use redshifts corrected for the infall of the Local Group toward the Virgo cluster and the Great Attractor (cz_{corr}) instead of CMB redshifts, we obtain a HD rms of 0.34–0.38 mag for *VJH* bands (see the right half of Fig. 2.7). We note that even after infall corrections the scatter in the HDs is still mostly due to SNe in galaxies with $cz < 2000 \text{ km s}^{-1}$. Therefore, to estimate the PMM distance precision and the Hubble constant (H_0), given by

$$\log H_0 = (25 - a_{\text{HD},x} + \text{ZP}_x)/5, \quad (2.25)$$

we use only SNe II with $cz > 2000 \text{ km s}^{-1}$ and, as visible in the left half of Fig. 2.8, the HD rms decreases significantly. The corresponding values of H_0 and rms are listed in Table 2.3.

The values of H_0 range between 67.1 and $74.9 \text{ km s}^{-1} \text{ Mpc}^{-1}$. Taking into account that the ZP_x values were calibrated using TRGB distances in the scale of Jang and Lee (2017b), our H_0 values, as expected, are consistent within the errors with those reported in Jang and Lee (2017a), i.e., $71.17 \pm 1.66 \pm 1.87 \text{ km s}^{-1} \text{ Mpc}^{-1}$, which also use the Jang and Lee (2017b) calibration.

As visible in Column 4 of Table 2.3, all the H_0 values are compatible within their errors. However, we note that H_0 decreases moving from shorter to longer wavelengths, which could suggest a systematic introduced by: (1) our assumption of the R_V value for the SN host galaxies, or (2) an

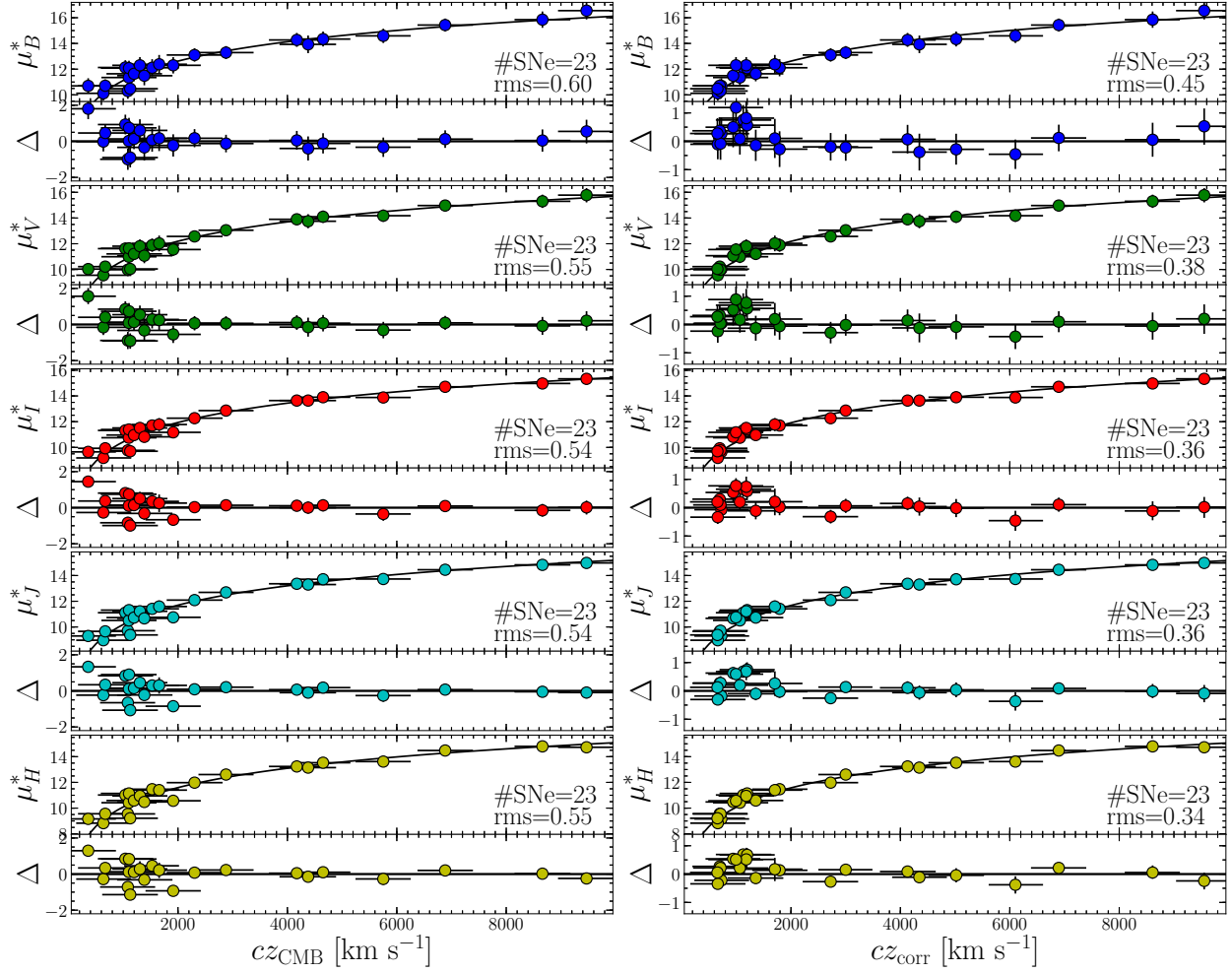


Figure 2.7: Hubble diagrams for SNe II with PMM distances and CMB redshifts (left) and redshifts corrected for the Virgo and Great Attractor infall (right). Solid lines correspond to Hubble law fits. Residuals are plotted at bottom of each panel.

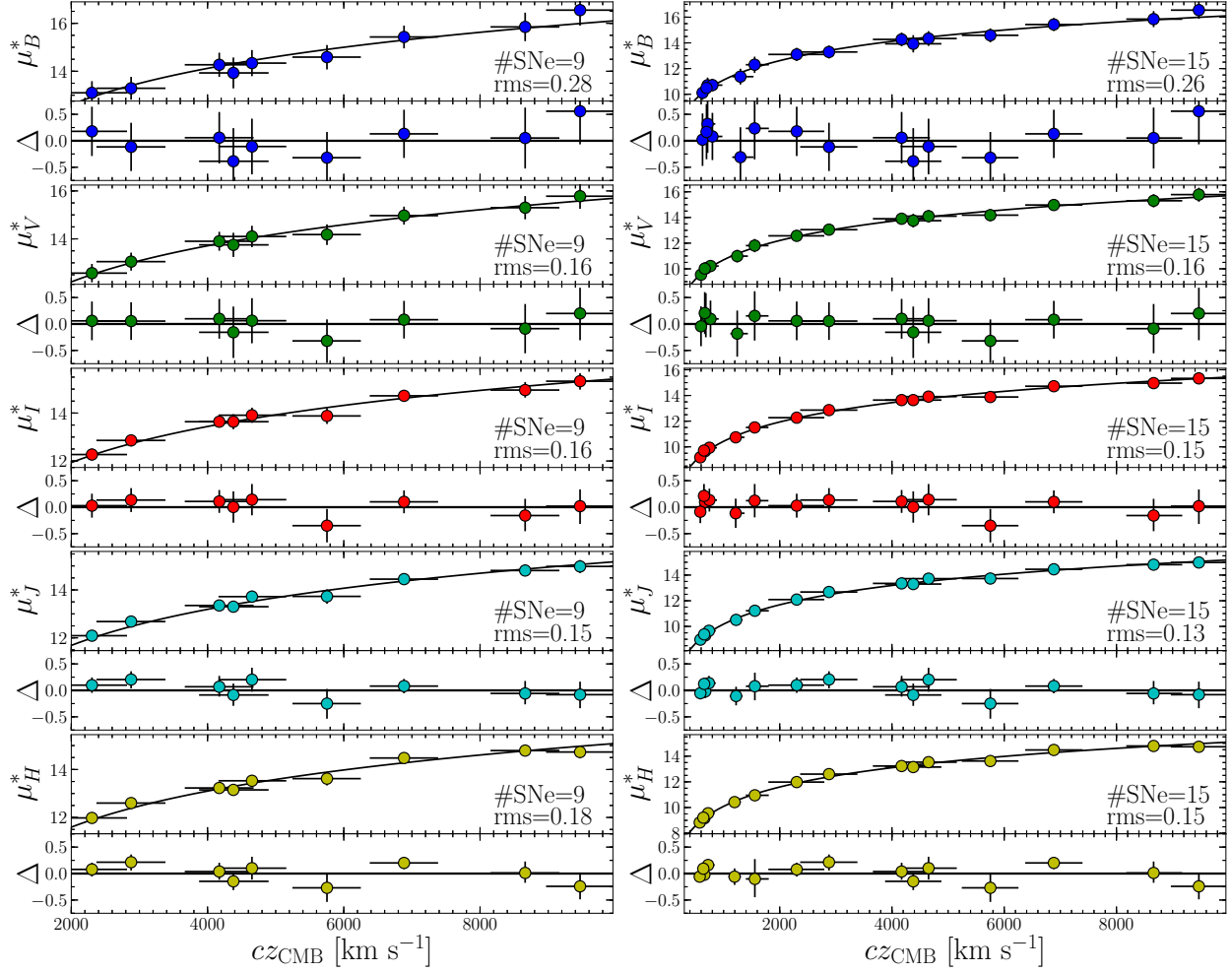


Figure 2.8: Hubble diagrams for SNe II with distances computed with the PMM, using the nine SNe II at $cz > 2000 \text{ km s}^{-1}$ (left) and including the six SNe II in galaxies with distance measured with TRGB, Cepheids, or SN Ia (right), where the H_0 values are those computed with the nine SNe II at $cz > 2000 \text{ km s}^{-1}$, and used to convert distances of the six nearest SNe II to redshifts. Solid lines correspond to the Hubble law fits. Residuals are plotted at the bottom of each panel.

Band	All ^a		$c\mathbf{z}_{\text{CMB}} > 2000 \text{ km s}^{-1}$				Final ^d
			$R_V = 3.1^b$		$R_V = 2.3^b$		
	$c\mathbf{z}_{\text{CMB}}$	$c\mathbf{z}_{\text{corr}}$	H_0^c	rms	H_0^c	rms	rms
<i>B</i>	0.60	0.45	$74.9^{+10.6}_{-9.2}$	0.28	$75.8^{+11.0}_{-9.6}$	0.30	0.26
<i>V</i>	0.55	0.38	$71.4^{+8.2}_{-7.3}$	0.16	$71.5^{+7.9}_{-7.1}$	0.16	0.16
<i>I</i>	0.54	0.36	$69.5^{+6.7}_{-6.1}$	0.16	$69.4^{+6.4}_{-5.8}$	0.16	0.15
<i>J</i>	0.54	0.36	$68.6^{+5.7}_{-5.2}$	0.15	$68.7^{+5.7}_{-5.2}$	0.15	0.13
<i>H</i>	0.55	0.34	$67.1^{+5.4}_{-5.0}$	0.18	$67.2^{+5.4}_{-5.0}$	0.18	0.15

^a We do not report the H_0 values for this SN set because they are severely affected by peculiar velocities.

^b R_V value adopted for SN II host galaxies.

^c In $\text{km s}^{-1} \text{ Mpc}^{-1}$. Errors are the 80 per cent CI, and include the TRGB zero-point systematic error and the error in the determination of the Local Group velocity.

^d Set of 15 SNe II: nine SNe at $cZ_{\text{CMB}} > 2000 \text{ km s}^{-1}$ plus six SNe in galaxies with TRGB, Cepheids, or SN Ia distances.

Table 2.3: Hubble diagram parameters.

underestimation and/or an overestimation of the host galaxy colour excesses for the four SNe in the PMM calibration set and the nine SNe at $cZ_{\text{CMB}} > 2000 \text{ km s}^{-1}$, respectively. To test the first possibility, we change the R_V adopted for SN II host galaxies to the lowest R_V value for which the Fitzpatrick (1999) extinction curve is defined ($R_V = 2.3$). As is visible in Column 6 of Table 2.3, there are no significant changes in the H_0 values. For the second possibility, we found that an underestimation of $E_h(B-V)$ for the SNe in the calibration set, or an overestimation of $E_h(B-V)$ for the SNe at $cZ_{\text{CMB}} > 2000 \text{ km s}^{-1}$, of 0.05–0.07 mag can erase the tension between the H_0 values for all bands. Given the typical statistical $E_h(B-V)$ error of 0.097 mag (see Section 2.7), the probability of obtaining an $E_h(B-V)$ underestimation of 0.05–0.07 mag with four objects is of 8 per cent, while to obtain an overestimation in a same amount for nine objects is of 5 per cent. It is worth mentioning that also the scatter in ZP_x decreases going from shorter to longer wavelengths, suggesting again a trend introduced by the combination of a large uncertainty in the colour excess estimation and the low number statistics.

Regarding the HD scatter, we note that the rms of 0.28 mag obtained with the *B*-band decreases to 0.15–0.18 mag for the *VIJH* bands. Despite the good results, the low number of SNe II within

galaxies at $cz_{\text{CMB}} > 2000 \text{ km s}^{-1}$ makes the result not statistically robust. Therefore, to check the PMM distance precision, it is necessary to include more SNe II into the analysis. Thus, we include the four SNe II used for the PMM calibration, plus other two in galaxies having Cepheid and SN Ia distances. The latter distances are converted to redshifts through the Hubble law (equation 2.24), where for each band we use the H_0 value listed in Column 4 of Table 2.3 and the ZP value given in Table 2.2.

The right half of Fig. 2.7 shows the HDs computed with the selected SNe II based on the aforementioned criterion, which correspond to our final sample. For *VI* bands we obtain a HD rms of 0.15–0.16 mag. The lowest HD rms is obtained with the *J*-band, whose rms of 0.13 mag translates into a distance precision of 6 per cent. This value, compared to the rms of 0.15–0.26 mag obtained for optical bands, suggests that using the *J*-band photometry instead of optical one to measure PMM distances can improve the precision by at least 0.07 mag.

For the *H*-band we expected a similar HD rms than for *J*-band since, among *BVIJH* bands, the *H*-band is the least affected by dust extinction. We, however, obtained a HD rms of 0.15 mag. The latter can be partially due to the higher photometry error of the *H*-band (of 0.07 mag) with respect to the error of the *J*-band (of 0.05 mag).

2.10 DISCUSSION

2.10.1 Statistical significance of the result

Given the small size of our SN sample, the HD rms of 0.13 mag we measured for the *J*-band is not statistically robust enough to be considered as a measure of the PMM distance precision in that band. In particular, we want to know the probability of measuring a $\text{rms} \leq 0.13 \text{ mag}$ with $N = 15$ values drawn from a parent distribution with standard deviation (σ) $\geq 0.13 \text{ mag}$. Assuming a normal parent distribution, the quantity $(N-1)(\text{rms}/\sigma)^2$ has a chi-square distribution with $N-1$ degrees of freedom. Using this, we found that there is a 1 per cent chance that the parent distribution has $\sigma = 0.23 \text{ mag}$. Therefore, with the evidence we have, we can set an upper limit on the PMM distance precision with the *J*-band of 10 per cent with a CL of 99 per cent.

Method	HD rms	Band	#SNe	Reference
PCM	0.43	<i>Y</i>	30	de Jaeger et al. (2015)
SCM	0.25	<i>B</i>	19	Olivares E. et al. (2010)
PMM	0.13	<i>J</i>	15	This work
PMM ^a	0.14	<i>J</i>	14	This work
PMM ^a	0.14	<i>H</i>	14	This work
SCM ^{a,b}	0.21	<i>J</i>	14	This work
SCM ^{a,b}	0.23	<i>H</i>	14	This work

^a Excluding SN 2002hj from the SN sample.

^b Using the PMM parameters evaluated at 50 d.

Table 2.4: Distance precision of different methods.

2.10.2 Comparison with other methods

For a consistent comparison of our results with those from other SN II distance measurement methods, we select results from works that uses a sample of SNe II at $z \approx 0.01$ – 0.03 .

Table 2.4 lists the best distance precisions reached by other SN II distance measurement methods along with results obtained in this work. We note that the precision we report in this work is significantly lower than the best dispersion obtained by other works with SCM and PCM.

We also compare PMM and SCM applied to the same sample for *J*- and *H*-band. For this comparison we discard SN 2002hj because there is not photometry in *J*-band at 50 d since explosion. As visible in Table 2.4, the dispersion is lower by ~ 30 – 40 per cent in both band.

2.10.3 Error budget

Taking into account that the lowest HD rms is obtained with the *J*-band, in Table 2.5 we show the statistical error budget for the distances measured for that band. We see that 88.6 per cent of the statistical error is induced by the errors of the first four terms: the host galaxy colour excess, the explosion epoch, the PMM zero-point, and the *J*-band photometry. Therefore, it is possible improve the performance of the PMM in the future developing a better method to estimate $E_h(B-V)$, selecting SNe II with explosion epoch constrained within a small range of time, including more SNe II in the PMM calibration set, and increasing the quality of the *J*-band photometry.

Error source	Typical error	Error on μ_J (mag)	% of total error
$E_h(B-V)$	0.097 mag	0.079	35.7
t_0	2.6 days	0.066	24.9
ZP_J	0.050 mag ^a	0.050	14.3
m_J	0.049 mag	0.049	13.7
v_{ph}	60 km s ⁻¹	0.040	9.2
cz_{hel}	29 km s ⁻¹	0.019	2.1
K_J	0.003 mag	0.003	0.05
$E_G(B-V)$	0.004 mag	0.003	0.05
Total		0.132	100.0

^a It does not include the TRGB zero-point systematic error.

Table 2.5: Error budget for the PMM J -band distances.

2.10.4 Diminishing systematics

Our results show that we are reaching a precision in distance modulus of ± 0.1 mag with the PMM at near-IR wavelengths. Therefore it is important to control systematics, and push them below 0.1 mag. For the latter in the following, we analyse sources of systematics affecting our results:

1. Explosion epoch: The dependence of the PMM calibration on explosion epoch (left half of Fig. 2.6) is stronger at early times, so t_0 errors have a strong effect at those epochs. In order to obtain errors lower than 0.1 mag for observations at $\Delta t \gtrsim 35$ d, we need SNe II with explosion epochs constrained within 5 d.

2. SN heliocentric redshift: When the host galaxy heliocentric redshift is used as a proxy of the SN heliocentric redshift, a systematic error of

$$\sigma(M_{x,\Delta t_i,v_{\text{ph},i}}) = \frac{5}{\ln 10} \frac{162 \text{ km s}^{-1}}{v_{\text{ph},i}} \quad (2.26)$$

is introduced into the absolute magnitude (equation 2.1). This effect increases when the photospheric velocity decreases, translating into errors $\gtrsim 0.1$ mag for photospheric velocities $\lesssim 3500$ km s⁻¹. Therefore, if optical spectra of a SN II do not show H II narrow emission lines due to a nearby H II region or if the SN is not within a nearly face-on galaxy, then epochs for which photospheric velocities are greater than 3500 km s⁻¹ are preferable.

3. Host galaxy redshift: A galaxy is believed to be within the Hubble flow when its redshift is

greater than 0.01. At that redshift, peculiar velocities are thought to be negligible compared with the velocities due to the Universe expansion. However, the typical error of 382 km s^{-1} translates into a distance modulus error of 0.28 mag for $z = 0.01$. Including the error in the determination of the Local Group velocity of 187 km s^{-1} , the redshift error increases to 425 km s^{-1} . Therefore, in order to reduce the error induced by redshift errors at a level lower than 0.1 mag, it is necessary to observe SNe II within galaxies at $z > 0.03$.

2.11 CONCLUSIONS

Our main results are the following:

1. Using nine SNe II at $cz > 2000 \text{ km s}^{-1}$, we obtained H_0 ranging between 67.1 and 74.9 $\text{km s}^{-1} \text{ Mpc}^{-1}$, and a HD rms of 0.15–0.28 mag.
2. Adding six SNe II with host galaxy distances measured with TRGB, Cepheids, or SN Ia (total 15), which distances were converted to redshifts through the Hubble law, we obtain a HD rms of 0.15–0.26 mag in the optical bands, which reduces to 0.13 mag in the J -band.

In order to test further the promising results we are obtaining in this work, it is necessary to carry out an optical and near-IR photometric follow-up of SNe II at $z > 0.03$ and with explosion epochs constrained within 5 d. For these SNe, it is necessary to take at least one optical spectrum at any epoch between 35–75 d since explosion.

Its evident from Fig. 2.1 that the quality of the near-IR photometry used in this work is in general lower than the optical one. Therefore, we expect that increasing the quality of the near-IR photometry will further improve our results.

Chapter 3

AN UPDATED NEAR-IR HUBBLE DIAGRAM FOR TYPE II SUPERNOVAE

3.1 INTRODUCTION

Distance measurements are important in astrophysics because with the knowledge of the distance we can infer intrinsic properties of astrophysical objects and structures, like their masses, absolute brightnesses, sizes, and matter distributions among others. In addition, measuring distances to objects at redshift $z > 0.01$ – 0.02 allows to infer properties of the Universe, like its expansion rate (also known as the Hubble constant, H_0) and, with objects at $z > 0.3$, the deceleration parameter. Distances of objects beyond $z = 0.01$ (~ 40 Mpc) can be measured with different methods, depending on the object. Among those methods we find the Tully-Fisher (TF) relation (Tully and Fisher 1977) for spiral galaxies, the Fundamental Plane (FP; Djorgovski and Davis 1987) and the Surface Brightness Fluctuation (SBF) method (Tonry and Schneider 1988) for early-type galaxies, the Phillips relation (Phillips 1993; Hamuy et al. 1996) and the multicolour light curve shapes (MLCS; Riess et al. 1996) for Type Ia SNe, and the Expanding Photosphere Method (EPM; Kirshner and Kwan 1974) and the Standardized Candle Method (SCM; Hamuy and Pinto 2002) for Type II SNe (SNe II).

In the case of SNe II, there are other five methods to measure distances: the Expanding Shock front Method (ESM; “[Angular Diameter Determinations of Radio Supernovae and the Distance Scale](#)”), the Spectral-fitting Expanding Atmosphere Method, (SEAM; Baron et al. 1995), the Photospheric Magnitude Method (PMM; Rodríguez et al. 2014), the global model of light curves and expansion

velocities (Pejcha and Prieto 2015), and the Photometric Colour Method (PCM; de Jaeger et al. 2015). Among the seven methods to measure SN II distances, the PMM gives the best distance precision. This method, which is a generalization of the SCM, needs only a measurement of the expansion velocity of the photosphere between 35 and 75 d since explosion to compute the absolute magnitude. Using *J*-band photometry, R19 set the PMM distance precision below 10 per cent at a confidence level (CL) of 99 per cent. Since the latter work was based on the analysis of 15 SNe II, with only seven at $z > 0.01$, the only way to really check the PMM distance precision is to carry out a new experiment with a bigger and better characterized SNe II sample.

The objective of this work is to establish the PMM distance precision for *BVIJH* bands, using a bigger SN II sample than the one used in R19.

This work is organized as follows: in Section 3.2 we describe the follow-up campaign we carried out along with the description of the photometric and spectroscopic data. We present the methodology to measure distances in Section 3.3. The construction and analysis of HDs are presented in Section 3.4. Discussion about the PMM distance precision and systematics are in Section 3.5. In Section 3.6 we present our conclusions.

3.2 OBSERVATIONAL CAMPAIGN

During three years, beginning in 2015 October, we carried out a follow-up campaign focused on obtaining optical and near-IR light curves of SNe II along with one optical spectrum per SN. The main objective is to measure distances through the PMM and construct HDs in order to compute a robust estimation of the precision of PMM distances and H_0 . Since 2017 September, we also include near-IR imaging and optical spectroscopy obtained during the extension of the Public ESO Spectroscopic Survey for Transient Objects (ePESSTO; Smartt et al. 2015). Telescopes and instruments used for this campaign are listed in Table 3.1.

For the follow-up campaign, we selected SNe II: (1) in galaxies at $z > 0.01$ in order to diminish the HD scatter induced by peculiar velocities, (2) observable in a range between 30 and 100 d since explosion, and (3) with explosion epochs constrained within one week, which allow to reduce the

Telescope	Optical imaging		Near-IR imaging		Optical spectroscopy		
	Instrument	Bands	Instrument	Bands	Instrument	Grating	Dispersion (Å/pixel)
TRAPPIST-S 0.6m	TRAPPISTCAM	<i>BVI</i>					
REM 0.6m	ROS2	<i>griz</i>	REMIR	<i>JH(K)</i>			
IRIS 0.8m			IRISCAM	<i>JH(K)</i>			
LCO 1.0m	Sinistro	<i>BVI</i>					
SMARTS 1.3m	ANDICAM	<i>BVI</i>	ANDICAM	<i>JH(K)</i>			
LCO 2.0m					FLOYDS	235 l/mm	3.5
MPG 2.2m	GROND	<i>griz</i>	GROND	<i>JHK</i>			
du Pont 2.5m	WFCCD	<i>BVI</i>	RetroCam	<i>JH</i>	WFCCD	blue grism	1.9
NTT 3.54m			SOFI	<i>JH(K)</i>	EFOSC2	gr#13	5.5
SOAR 4.1m			Spartan	<i>JH</i>	Goodman HTS	400 l/mm	2.0
Clay 6.5m					LDSS3	VPH-All	1.9
Gemini-S 8.1m					GMOS	R400	3.0
						B600	2.2

Table 3.1: Telescopes and instruments

error in the PMM distances.

3.2.1 Photometric Data

Images were processed with a collection of IRAF¹ tasks. For optical images, data reduction includes bias and dark subtraction, flat-field correction, cosmic rays rejection², and image combination in cases where more than one image was acquired. For near-IR images, data reduction consists on dark subtraction, flat-field division, sky subtraction, geometric alignment and combination of the dithered images. SOFI near-IR images were reduced with the PESSTO pipeline (Smartt et al. 2015).

Instrumental magnitudes were measured using the point spread function (PSF) technique along with a low-order polynomial fit to remove the host galaxy background, which are implemented in the SNOOPY³ package. Final magnitudes were computed with respect to a local sequence of stars. For the optical sequences we use stars with *gri* magnitudes provided by PanSTARRS1 (Chambers et al. 2016; Flewelling et al. 2016), which are converted to *BVI* magnitudes using the transformations given in Smith et al. (2002). In case of PanSTARRS1 magnitudes are not available for the sequence stars, we calibrate it using Landolt (1992) standard stars. For the near-IR sequences we use stars

¹IRAF is distributed by the National Optical Astronomy Observatory, which is operated by the Association of Universities for Research in Astronomy (AURA) under cooperative agreement with the National Science Foundation.

²using the Laplacian detection algorithm L.A.Cosmic (van Dokkum 2001).

³SNOOPY is a package for SN photometry using PSF fitting and/or template subtraction developed by E. Cappellaro. A package description can be found at <http://sngroup.oapd.inaf.it/snoopy.html>

with JH magnitudes provided by 2MASS (Skrutskie et al. 2006).

3.2.2 Spectroscopic Data

Low resolution optical spectra were taken for each SN followed by comparison lamp spectra taken at the same position in the sky. For WFCCD, EFOSC2, Goodman HTS, and LDSS3 spectra, we took 1–3 flux standard stars per night. For GMOS spectra, we took 3–5 standard stars and then we computed a sensitivity function, while for FLOYDS spectra a sensitivity function derived from flux standard star observations taken during commissioning is used. Spectra were taken with the slit along the parallactic angle (Filippenko 1982). Data reduction include bias subtraction, flat-field correction, cosmic rays rejection, one-dimensional spectrum extraction and sky subtraction, wavelength calibration, and flux calibration. FLOYDS spectra were reduced using its own pipeline (Valenti et al. 2014), while EFOSC2 spectra were reduced with the PESSTO pipeline (Smartt et al. 2015).

3.2.3 Sample of Supernovae

During the follow-up campaign, we obtained optical and near-IR images along with optical spectroscopy of several SNe II. From that sample, we select a subsample of 24 SNe II that comply with the following requirements: (1) being at $cz > 4000 \text{ km s}^{-1}$ in order to keep the HD rms induced by peculiar velocities below 0.2 mag, (2) having spectroscopy between 35 and 75 d since explosion, which is the range of applicability of the PMM (R19), and (3) with $BVIJH$ photometry, covering the epoch of the spectroscopy given in point (2). Fig. 3.1 shows the optical and near-IR light curves of the new SNe II observed during our campaign and used in this study. We complement this sample with the 7 SNe II at $cz > 4000 \text{ km s}^{-1}$ used in R19: SN 2002hj, SN 2003E, SN 2003T, SN 2003bl, SN 2003bn, SN 2003ci, and SN 2003cn. Table 3.2 summarizes the SN name (Column 1), the name of the host galaxy and its type (Column 2 and 3), the heliocentric SN redshift $z_{\text{helio}}^{\text{SN}}$ (Column 4), and the Galactic colour excess E_{B-V}^{G} (Column 5) of the final sample of 31 SNe II.

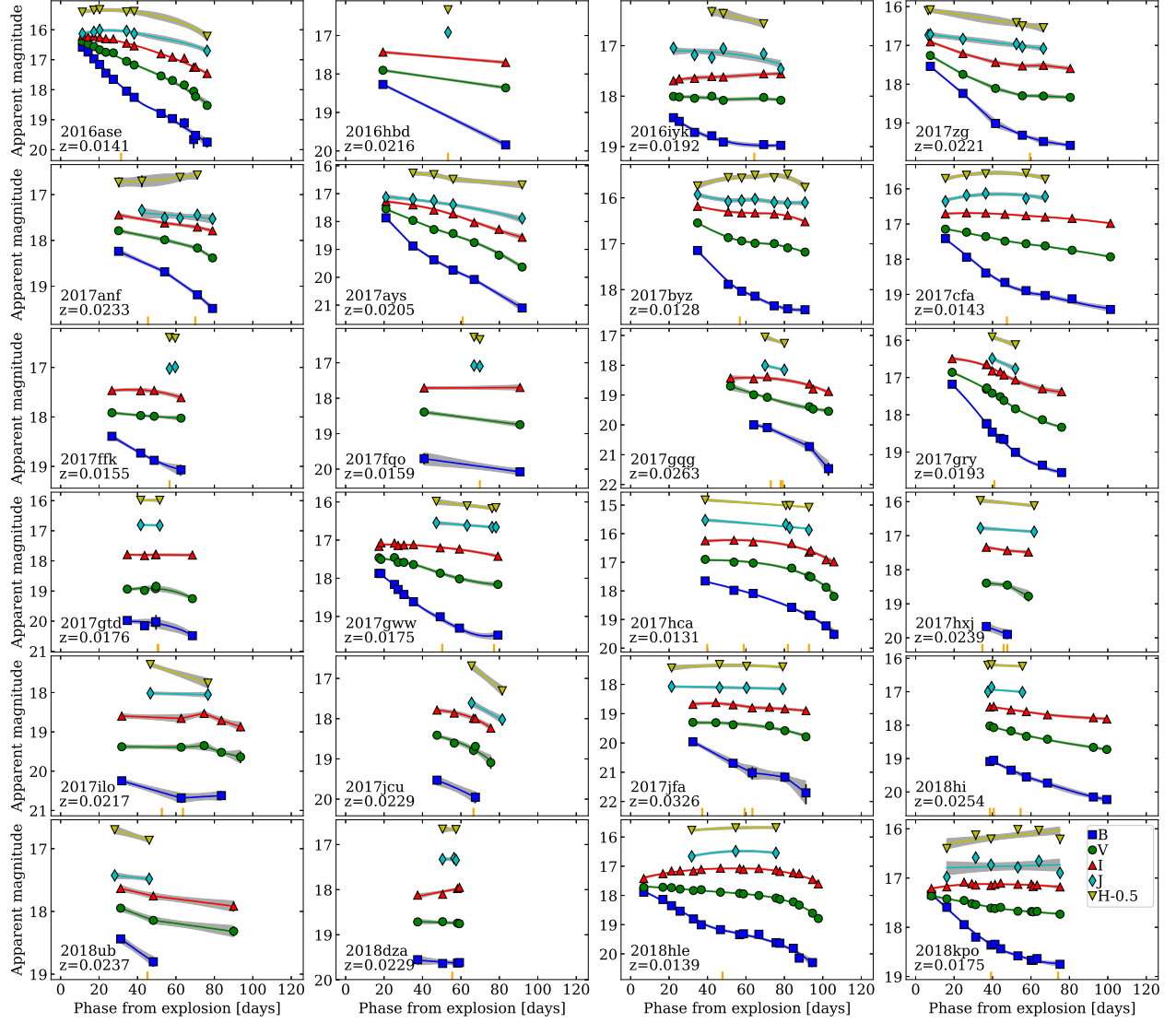


Figure 3.1: Light curves of the SNe II observed during our follow-up campaign. The estimated explosion epoch of each SN is used as reference time. Orange ticks mark the epochs of the spectroscopy. Solid lines and shaded regions correspond to the light curve fits and the 10th–90th percentile ranges, respectively.

SN	Host galaxy	Host type ^b	$z_{\text{helio}}^{\text{SN}}$ ^c	E_{B-V}^{G} ^d
2003bn ^a	LEDA 831618	–	$3897 \pm 25^*$	0.056 ± 0.009
2003E ^a	MCG –4–12–4	Sc?	$4484 \pm 21^*$	0.041 ± 0.007
2003bl ^a	NGC 5374	SB(r)bc?	$4295 \pm 41^*$	0.023 ± 0.004
2003cn ^a	IC 849	SAB(rs)cd	$5430 \pm 162^\dagger$	0.018 ± 0.003
2002hj ^a	NPM1G +04.0097	–	$7079 \pm 20^*$	0.101 ± 0.016
2003T ^a	UGC 4864	SA(r)ab	$8368 \pm 6^\ddagger$	0.027 ± 0.004
2003ci ^a	UGC 6212	Sb	$9052 \pm 21^*$	0.051 ± 0.008
2016ase	ESO 504–G9	dIrr	$4216 \pm 4^*$	0.041 ± 0.006
2016hbd	PGC 90644	Sdm	$6472 \pm 162^\dagger$	0.119 ± 0.019
2016iyk	AGC 203753	–	$5743 \pm 170^\dagger$	0.027 ± 0.004
2017zg	CGCG 7–19	Sb	$6615 \pm 163^\dagger$	0.114 ± 0.018
2017anf	SDSS J133313.38+080325.3	–	$6971 \pm 17^*$	0.023 ± 0.004
2017ays	SDSS J121246.44+002432.6	–	$6157 \pm 22^*$	0.024 ± 0.004
2017byz	NGC 3660	SB(r)bc	$3837 \pm 26^*$	0.035 ± 0.006
2017cfa	MCG –1–26–3	–	$4293 \pm 19^*$	0.083 ± 0.013
2017ffk	IC 991	SB(s)c?	$4652 \pm 162^\dagger$	0.066 ± 0.010
2017fqo	NGC 716	SBa?	$4757 \pm 22^*$	0.046 ± 0.007
2017gqg	6dF J2322161–234204	–	$7877 \pm 21^*$	0.021 ± 0.003
2017gry	ESO 155–G36	S0(r)?	$5797 \pm 163^\dagger$	0.022 ± 0.003
2017gtd	IC 221	Sc	$5277 \pm 26^*$	0.090 ± 0.014
2017gww	NGC 7816	Sbc	$5240 \pm 7^\ddagger$	0.055 ± 0.009
2017hca	2MASX J08494084–0805303	–	$3935 \pm 13^*$	0.036 ± 0.006
2017hxj	ESO 293–G22	S0?	$7160 \pm 15^*$	0.012 ± 0.002
2017ilo	2MASX J03312172+0408161	–	$6496 \pm 36^*$	0.177 ± 0.028
2017jcu	UGC 2705	SABcd	$6869 \pm 163^\dagger$	0.102 ± 0.016
2017jfa	CGCG 29–27	diffuse	$9785 \pm 164^\dagger$	0.056 ± 0.009
2018hi	2MASX J08533957–2503294	–	$7611 \pm 163^\dagger$	0.138 ± 0.022
2018ub	CGCG 40–65	–	$7099 \pm 43^*$	0.011 ± 0.002
2018dza	ESO 448–G4	Sc	$6853 \pm 127^*$	0.115 ± 0.018
2018hle	IC 340	dS0'0?	$4154 \pm 162^\dagger$	0.046 ± 0.007
2018kpo	MCG –1–10–19	SAB(r)cd	$5248 \pm 162^\dagger$	0.047 ± 0.007

^aPreviously studied in R19.

^bFrom NASA/IPAC Extragalactic Database (NED).

^cHeliocentric SN redshift, estimated through narrow H II emission lines in the spectra (*), or adopting the redshift of the host galaxy nucleus from NED (\ddagger), adding in quadrature an error of 162 km s^{-1} if the host galaxy is not face-on (\dagger).

^dGalactic colour excesses from Schlafly and Finkbeiner (2011), with an error of 16 per cent (Schlegel et al. 1998).

Table 3.2: SN sample.

3.3 METHODOLOGY

In R19 we presented an analysis based on the probability density function (pdf) of observables involved in the PMM distance measurements. In this work, with the aim to allow to compute PMM distances in an easy and less time-consuming way than working with pdfs, we present analytical expression for all quantities and errors we compute, assuming that observational errors are normals.

3.3.1 Photospheric Magnitude Method

As was shown in Rodríguez et al. (2014) and R19, the absolute magnitude of an SN II for a given x -band at time t_i , $M_{x,\Delta t_i,v_{\text{ph},i}}$, can be parametrized as a function of the photospheric velocity v_{ph} and the explosion epoch t_0 , as

$$M_{x,\Delta t_i,v_{\text{ph},i}} = a_{x,\Delta t_i}^* + \text{ZP}_x - 5 \log \left(\frac{v_{\text{ph},i}}{5000 \text{ km s}^{-1}} \right). \quad (3.1)$$

Here, $\Delta t_i \equiv (t_i - t_0)/(1 + z_{\text{helio}}^{\text{SN}})$ is the elapsed time since the explosion in the SN rest frame,

$$a_{x,\Delta t_i}^* = c_x \cdot \left(\frac{\Delta t_i}{100 \text{ d}} \right) - 5 \log \left(\frac{\Delta t_i}{100 \text{ d}} \right) \quad (3.2)$$

(R19) is a function that represents the dependence of $M_{x,\Delta t,v_{\text{ph}}}$ on Δt (without a constant term), and ZP_x is the zero-point of the PMM, which is estimated empirically with SNe II in galaxies with known distance. With this standardization, the knowledge of t_0 , a set of $v_{\text{ph},i}$ measurements within 35–75 d since explosion (R19) and measurements of the apparent magnitude at the same epochs of $v_{\text{ph},i}$, $m_{x,i}$, we can compute the SN II distance modulus μ_x using the following formulas:

$$m_{x,i}^{\text{AK}} = m_{x,i} - A_{x,i}^{\text{G}} - K_{x,i}, \quad (3.3)$$

where $A_{x,i}^{\text{G}}$ and $K_{x,i}$ are the Galactic broad-band extinction and the K -correction, respectively (see Appendix F),

$$\mu_{x,i}^{*,\text{AK}} = m_{x,i}^{\text{AK}} + 5 \log \left(\frac{v_{\text{ph},i}}{5000 \text{ km s}^{-1}} \right) - a_{x,\Delta t_i}^*, \quad (3.4)$$

$$\mu_{x,i}^* = \mu_{x,i}^{*,\text{AK}} - A_{x,i}^{\text{h}}, \quad (3.5)$$

where $A_{x,i}^{\text{h}}$ is the host galaxy broad-band extinction, and

$$\mu_x^* = \langle \mu_{x,i}^* \rangle. \quad (3.6)$$

Here, angle brackets denote a weighted average, where the weights $w_{x,i}$ are

$$w_{x,i} = \left[\sigma_{m_{x,i}}^2 + \left(\frac{5}{\ln 10} \frac{\sigma_{v_{ph,i}}}{v_{ph,i}} \right)^2 \right]^{-1}, \quad (3.7)$$

while the error on μ_x^* (the pseudo-distance modulus) is given by

$$\begin{aligned} \sigma_{\mu_x^*}^2 = & \frac{1}{\sum w_{x,i}} + \left(\mathcal{R}_{x, \langle (B-V)_{A,i} \rangle}^G \right)^2 \sigma_{E_{B-V}^G}^2 + \left[\mathcal{K}_{x, \langle (B-V)_{AK,i} \rangle}^s + z_{\text{helio}}^{\text{SN}} \frac{\text{rms}(\mathcal{K}_x^s)}{\sigma_{z_{\text{helio}}^{\text{SN}}}} + \frac{5c/\ln 10}{\langle v_{ph,i} \rangle} \right]^2 \sigma_{z_{\text{helio}}^{\text{SN}}}^2 \\ & + \left[\frac{5/\ln 10}{\langle \Delta t_i \rangle / 100 \text{d}} - c_x \right]^2 \left[\frac{1/100 \text{d}}{1 + z_{\text{helio}}^{\text{SN}}} \right]^2 \sigma_{t_0}^2 + \left(\mathcal{R}_{x, \langle (B-V)_{0,i} \rangle}^h \right)^2 \sigma_{E_{B-V}^h}^2, \end{aligned} \quad (3.8)$$

where $(B-V)_{A,i}$ is the observed $(B-V)_i$ colour corrected for E_{B-V}^G , $(B-V)_{AK,i}$ is the $(B-V)_{A,i}$ colour corrected for $z_{\text{helio}}^{\text{SN}}$, $(B-V)_{0,i}$ is the $(B-V)_{AK,i}$ colour corrected for host galaxy colour excess E_{B-V}^h , and \mathcal{R}_x^G , \mathcal{K}_x^s , and \mathcal{R}_x^h are polynomials on $(B-V)_A$, $(B-V)_{AK}$, and $(B-V)_0$, respectively (see Appendix F). Finally, distance modulus is given by

$$\mu_x = \mu_x^* - \text{ZP}_x, \quad (3.9)$$

$$\sigma_{\mu_x}^2 = \sigma_{\mu_x^*}^2 + \sigma_{\text{ZP}_x}^2. \quad (3.10)$$

3.3.2 Light-curve interpolation

To interpolate the photometry to the epoch of the spectroscopy we use the procedure presented in R19. When this procedure cannot perform a fit (e.g. for light curves with less than six points), we perform a linear interpolation between points. Typical photometry rms errors are of 0.030, 0.022, 0.024, 0.045, and 0.057 mag for B -, V -, I -, J -, and H -band, respectively.

Fig. 3.1 shows the results of the light-curve fitting (solid lines) along with the 10th–90th percentile ranges (shaded regions).

3.3.3 Photospheric velocities

In this work we use the Fe II $\lambda 5169$ line absorption minima as a proxy for photospheric velocities. To measure this minimum, we use the procedure presented in R19. For the SNe in our set, the typical v_{ph} rms error obtained with this process is of 79 km s^{-1} .

3.3.4 Explosion epochs

The explosion epochs of the 24 SNe II we present in this work are, by design of the follow-up campaign, in general well constrained between the last non-detection t_{ln} and the first detection t_{fd} , with a typical $t_{\text{fd}} - t_{\text{ln}}$ range value of 3.9 d. Only four SNe (SN 2017cfa, SN 2017fqo, SN 2017gry, and SN 2017hca) have t_0 constrained in $t_{\text{fd}} - t_{\text{ln}}$ ranges greater than 10 d. In order to improve the t_0 estimation for the SNe in our set, we compute explosion epochs using spectroscopy and the procedure presented in R19. The procedure makes use of the Supernova Identification (SNID; Blondin and Tonry 2007) code along with the template library presented in R19, which contains templates of 59 SNe II with t_0 constrained within 10 d. Given an input spectrum, SNID finds by cross-correlation the spectra from the R19 library that are more similar to the input spectrum. In this process, we give all spectra earlier than 40 d since the first detection as input, $\{\text{spec}\}$. The output of this process is the likelihood of t_0 given $\{\text{spec}\}$, $\mathcal{L}(t_0|\{\text{spec}\})$.

The posterior pdf of t_0 , $p(t_0|\{\text{spec}\})$, combining $\mathcal{L}(t_0|\{\text{spec}\})$ with the uniform prior on t_0 , $p(t_0)$, provided by photometric information, i.e.,

$$p(t_0|\{\text{spec}\}) \propto \mathcal{L}(t_0|\{\text{spec}\})p(t_0). \quad (3.11)$$

Values are summarized in Table 3.3. The typical rms error we obtained for our SN set is of 1.1 d.

3.3.5 Host galaxy colour excess

To estimate E_{B-V}^{h} we use the colour-colour curve (C3) method (Rodríguez et al. 2014; R19). This method, developed by Natali et al. (1994) to estimate colour excesses for open clusters, relies on the assumption that all SNe II have the same C3. R19 found that, among all possible color-color combinations for $BVIJH$ bands, the best combination to estimate colour excesses with the C3 method is the $V-I$ versus $B-V$. Writing equation 14 of R19 for this specific colour-colour combination, we obtain

$$E_{B-V}^{\text{h}} = \langle 1.081(V-I)_{AK,i} - 0.486(B-V)_{AK,i} \rangle - 0.116, \quad (3.12)$$

SN	E_{B-V}^h (mag)	Discovery (JD)	t_{in}^a (d)	t_{fd}^a (d)	$t_{0,\text{SNID}}^a$ (d)	$t_{0,\text{final}}^a$ (d)	References ^d
2016ase	0.008(0.048)	2457453.86	-1.01	0.0	-3.96(4.86)	-0.52(0.29)	ATel 8784
2016hbd	0.111(0.043)	2457665.494	-3.424	-1.017	-0.66(5.97)	-2.19(0.70)	ATel 9593, ATLAS
2016iyk	0.001(0.047)	2457740.283	-3.153	0.0	-5.94(5.56)	-1.77(0.90)	TNS, ATLAS
2017zg	0.078(0.042)	2457785.018	-3.902	0.0	— ^c	-1.95(1.13)	TNS
2017anf	-0.054(0.065)	2457794.012	-0.852	0.0	0.85(7.09)	-0.43(0.25)	TNS, ATLAS
2017ays	0.035(0.067)	2457805.072	-3.924	0.0	-15.67(8.03)	-2.38(1.11)	TNS
2017byz	-0.034(0.077)	2457816.943	-7.853	0.0	-4.95(5.47)	-4.14(2.20)	TNS, ATLAS
2017cfa	0.043(0.069)	2457828.93	-11.97	0.0	-8.10(6.16)	-6.83(3.25)	TNS
2017ffk	0.015(0.054)	2457942.84	-2.01	0.0	— ^c	-1.00(0.58)	TNS
2017fqo	0.147(0.099)	2457957.721	-41.154	0.0	-23.69(4.86)	-23.76(4.84)	TNS
2017gqg	0.027(0.082)	2457980.05	-8.08	-2.02	6.88(5.02)	-3.46(1.47)	TNS, ATLAS
2017gry	0.083(0.065)	2458006.503	-35.911	0.0	3.20(5.52)	-2.72(2.89)	TNS
2017gtd	0.559(0.049)	2458012.62	-8.58	-6.57	— ^c	-7.58(0.58)	TNS, ATLAS
2017gww	-0.028(0.052)	2458023.05	-4.11	-0.16	-13.60(5.75)	-2.73(1.10)	TNS, ATLAS
2017hca	0.159(0.070)	2458025.094	-90.186	0.0	-8.52(5.33)	-9.06(4.77)	TNS
2017hxj	0.331(0.089)	2458065.641	-3.821	-1.811	-0.11(4.73)	-2.77(0.57)	ATel 10960, ATLAS
2017ilo	0.020(0.078)	2458078.91	-1.99	0.0	-2.05(4.98)	-1.01(0.57)	TNS
2017jcu	0.007(0.084)	2458109.743	-8.066	0.0	-6.91(5.39)	-4.73(2.21)	TNS
2017jfa	0.017(0.077)	2458110.94	-4.93	0.0	-3.89(5.31)	-2.60(1.41)	TNS
2018hi	-0.076(0.084)	2458133.67	-3.65	-1.68	0.93(4.53)	-2.59(0.56)	TNS, ATLAS
2018ub	-0.011(0.059)	2458162.88	-22.82	-21.79	-23.81(6.18)	-22.31(0.30)	ATel 11308, TNS, ATLAS
2018dza	0.115(0.057)	2458315.81	-3.98	0.0	0.72(5.00)	-1.77(1.14)	TNS
2018hle	0.117(0.060)	2458408.981	-1.901	0.0	-4.76(4.96)	-1.02(0.55)	TNS
2018kpo	-0.016(0.047)	2458476.872	-0.961	0.0	-2.90(4.54)	-0.51(0.28)	ATel 12326, TNS

Column 1: SN names. Columns 2: host galaxy colour excesses estimated with the $V-I$ versus $B-V$ C3, with rms errors in parenthesis. Column 3: discovery epochs. Column 4 and 5: last non-detection and first detection epochs, respectively. Column 6 and 7: explosion epochs estimated with SNID and the SN II template used in R19, without any prior and with photometric priors, respectively (rms error in parenthesis). Column 8: references for discovery, last non-detection, and first detection epochs.

^aEpochs with respect to the discovery epoch.

^cSpectra before 40 d since explosion not available.

^dTNS: Transient Name Server (<https://wis-tns.weizmann.ac.il/>); ATLAS: Asteroid Terrestrial-impact Last Alert System (<http://www.fallingstar.com/>).

Table 3.3: SN II parameters.

Here, $(V-I)_{AK,i}$ is the $(V-I)_i$ colour corrected for Galactic colour excess and K -correction (see Appendix F), and the weights for the weighted average are

$$w_i = \left[1.168\sigma_{(V-I)_i}^2 + 0.237\sigma_{(B-V)_i}^2 - 1.051\sigma_{V_i}^2 \right]^{-1}. \quad (3.13)$$

The error on E_{B-V}^h is given by

$$\sigma_{E_{B-V}^h}^2 = \frac{1}{\sum_i w_i} + 0.006[\langle (B-V)_{AK,i} \rangle - 0.927E_{B-V}^h]^2 + 0.758(z_{\text{helio}}^{\text{SN}})^2 + \sigma_{E_{B-V}^G}^2 + \sigma_{C3}^2, \quad (3.14)$$

where $\sigma_{C3} = 0.057$ mag is the uncertainty in the C3 method zero-point.

The E_{B-V}^h values are summarized in Column 2 of Table 3.3. The typical rms error for the E_{B-V}^h measurements, without including the C3 intrinsic error, is of 0.063 mag. For six SNe (SN 2017anf, SN 2017byz, SN 2017gww, SN 2018hi, SN 2018ub, and SN 2018kpo) we obtain negative E_{B-V}^h values. They, however, are consistent with zero colour excess within their statistical errors.

3.3.6 PMM calibration

R19 presented an $a_{x,\Delta t}^*$ calibration based on 19 SNe II with two or more measurements of v_{ph} during 35–75 d since explosion. Despite our project was focused on obtaining one spectrum per SN, in our new data set there are seven SNe (SN 2017anf, SN 2017hca, SN 2017hxj, SN 2017ilo, SN 2017jfa, SN 2018hi, and SN 2018kpo) with 2–4 spectra during 35–75 d since explosion, which are useful to improve the calibration of $a_{x,\Delta t}^*$.

For each SN, the $a_{x,\Delta t_i}^*$ values are given by

$$a_{x,\Delta t_i}^* = m_{x,i}^{AK} - A_{x,i}^h + 5 \log \left(\frac{v_{\text{ph},i}}{5000 \text{ km s}^{-1}} \right) + \delta_{\text{SN}}, \quad (3.15)$$

where δ_{SN} is a constant term to normalize the $a_{x,\Delta t_i}^*$ of each SN to the same scale, while the dependence of $a_{x,\Delta t}^*$ on Δt is given in equation 3.2.

Fig. 3.3.6 shows the new $a_{x,\Delta t_i}^*$ we obtain, along with the values reported in R19. In order to obtain the c_x values (the free parameters in $a_{x,\Delta t_i}^*$, see equation 3.2), we performed a least-square minimization, performing 10^4 bootstrap resampling to estimate error in parameters. Values of c_x for $BVIJH$ bands are summarized in Column 2 of Table 3.4.

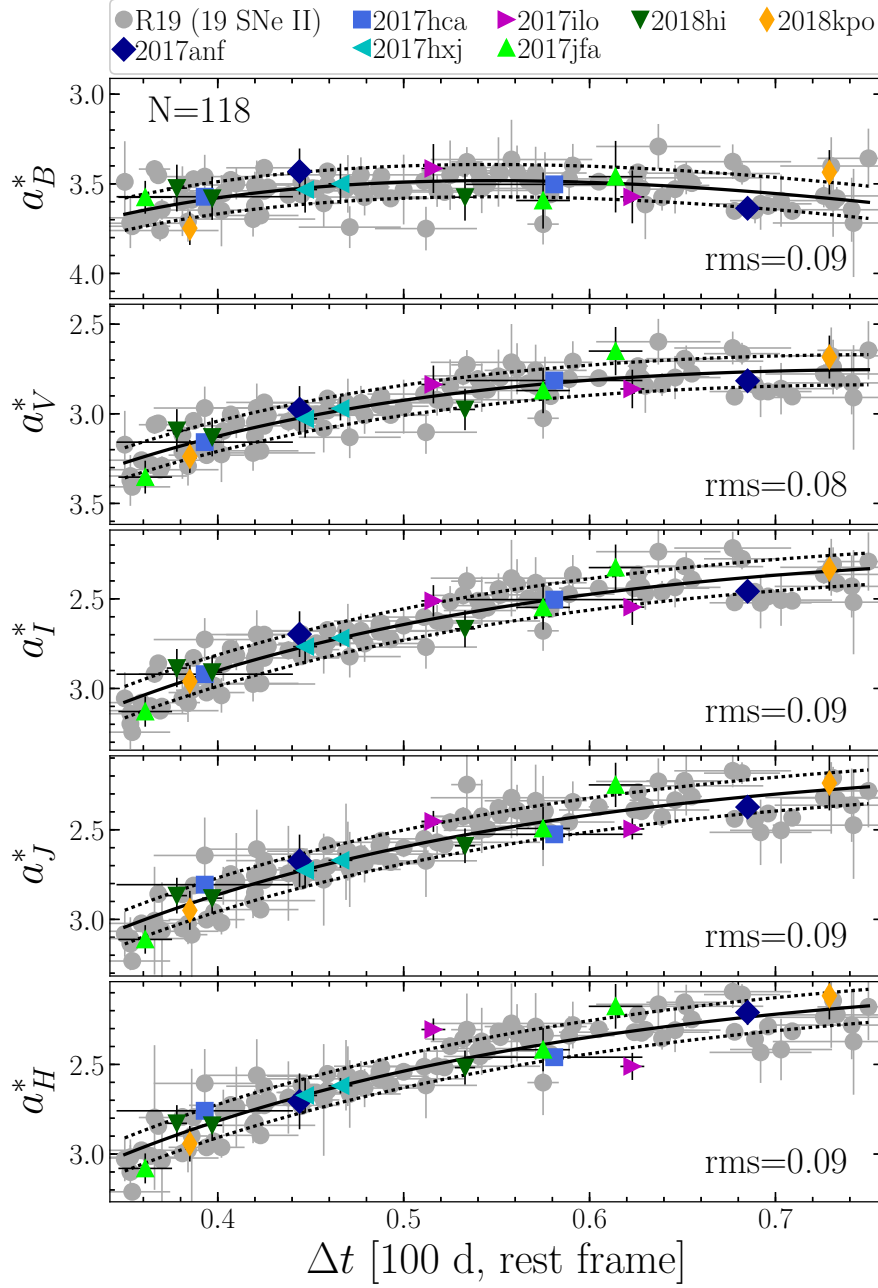


Figure 3.2: Values of a_x^* as a function of Δt for *BVIJH* for seven SNe presented in this work (coloured symbols) and 19 SNe used in the R19 calibration (gray circles). Black solid lines correspond to the parametric fits. Dotted lines indicate values within one rms.

x	c_x^a	$n_{\text{HD},x}^*$	$\sigma_{x,0}$	ZP_x^b
B	3.97(09)	-4.17(41)	0.29(00)	-20.96(13)
V	2.82(09)	-4.45(26)	0.07(00)	-21.01(12)
I	2.27(09)	-4.64(22)	0.09(00)	-20.81(12)
J	2.17(08)	-4.91(22)	0.13(00)	-20.77(09)
H	2.06(08)	-5.02(21)	0.13(00)	-20.79(07)

Note: parameters valid for $35 \text{ d} < \Delta t < 75 \text{ d}$. The rms errors are in parenthesis in units of 0.01.

Table 3.4: PMM parameters using C3 reddenings

3.4 HUBBLE DIAGRAMS

The distance precision of the PMM can be estimated through the Hubble diagram, specifically measuring the scatter around the Hubble law fit, which is given by

$$\mu_x^* = n_{\text{HD},x}^* + 5 \log(cz_{\text{CMB}}). \quad (3.16)$$

Here, cz_{CMB} is the redshift in the cosmic microwave background (CMB) rest frame, μ_x^* is the pseudo-distance modulus (equation 3.6), and $n_{\text{HD},x}^*$ is the HD y-intercept, which is inferred from a set of μ_x^* and cz_{CMB} measurements, minimizing

$$-2 \ln \mathcal{L} = \sum_{\text{SN}} \left[\ln V + \frac{(\mu_x^* - n_{\text{HD},x}^* - 5 \log cz_{\text{CMB}})^2}{V} \right], \quad (3.17)$$

where

$$V = \sigma_{\mu_x^*}^2 + \left(\frac{5}{\ln 10} \frac{\sigma_{cz_{\text{CMB}}}}{cz_{\text{CMB}}} \right)^2 + \sigma_{x,0}^2, \quad (3.18)$$

and $\sigma_{x,0}$ is the intrinsic error, which accounts for the scatter not explained by the errors on μ_x^* and cz_{CMB} .

To compute CMB redshifts, we use the host galaxy heliocentric ones and the formula given in Fixsen et al. (1996). We include a statistical rms error of 382 km s^{-1} due to peculiar velocities (Wang et al. 2006).

The left part of Fig. 3.3 shows the $BVIJH$ HDs using pseudo-distance moduli corrected for host galaxy colour excesses measured with the C3 method. We see that the scatter in the HD decreases as the central wavelength of the band moves toward the near-IR, reaching a rms of 0.21 mag for the H -band. The latter is mainly because the near-IR light is less affected by dust.

3.4.1 Hubble constant

To compute H_0 for *BVIJH* bands, we use the formula

$$H_{0,x} = 10^{(ZP_x - n_{\text{HD},x}^* + 25)/5}. \quad (3.19)$$

The $H_{0,x}$ statistical error, $\sigma_{H_{0,x}}^{\text{stat}}$, is given by

$$\sigma_{H_{0,x}}^{\text{stat}} = H_{0,x} \frac{\ln 10}{5} \left[\frac{\text{rms}(ZP_x)^2}{N_{\text{ZP}}} + \frac{\text{rms}(n_{\text{HD},x}^*)^2}{N_{\text{HD}}} \right]^{1/2}, \quad (3.20)$$

where N_{ZP} and N_{HD} are the number of SNe used to compute ZP_x and $n_{\text{HD},x}^*$, respectively. The $H_{0,x}$ systematic error, $\sigma_{H_{0,x}}^{\text{sys}}$, is given by

$$\sigma_{H_{0,x}}^{\text{sys}} = \left[\left(\frac{5\sigma_{\text{LGV}}/\ln 10}{M\{cz_{\text{CMB},i}\}} \right)^2 + \sigma_{\text{TRGB}}^2 + (\mathcal{R}_{x,0.7}^h \sigma_{\text{C3}})^2 \right]^{1/2}, \quad (3.21)$$

where $M\{cz_{\text{CMB},i}\}$ is the median CMB redshift in the HD, $\sigma_{\text{LGV}} = 187 \text{ km s}^{-1}$ is the Local Group velocity error (Tonry et al. 2000), $\sigma_{\text{TRGB}} = 0.058 \text{ mag}$ is the zero-point systematic error for the Tip of the Red Giant Branch (TRGB) distances (Jang and Lee 2017b), $\sigma_{\text{C3}} = 0.057 \text{ mag}$ is the systematic error of the C3 colour excess, and $\mathcal{R}_{x,0.7}^h$ is the factor to convert host galaxy colour excess into host galaxy broad-band extinction using a typical intrinsic $B-V$ colour of 0.7 mag.

To compute ZP_x , we use the four SNe II used in R19, which are in host galaxies having TRGB distances.

With those SNe, we compute ZP_x as

$$ZP_x = \langle \mu_{x,\text{SN}}^* - \mu_{\text{SN}}^{\text{host}} \rangle, \quad (3.22)$$

where $\mu_{x,\text{SN}}^*$ is the SN pseudo-distance modulus, $\mu_{\text{SN}}^{\text{host}}$ is the SN host galaxy distance modulus. Values of ZP_x and their rms errors for *BVIJH* bands are summarized in Column 5 of Table 3.4.

Column 3 of Table 3.5 list the H_0 values for *BVIJH* bands. We see that the H_0 values for *VIJH* bands are quite consistent with the H_0 value of $71.17 \pm 1.66(\text{stat}) \pm 1.87(\text{sys}) \text{ km s}^{-1} \text{ Mpc}^{-1}$ reported by Jang and Lee (2017a). The latter is because we are using the same TRGB calibration of Jang and Lee (2017b). For the *B*-band, H_0 is at least $\sim 6.5 \text{ km s}^{-1} \text{ Mpc}^{-1}$ higher than the values measured with *VIJH* bands, respectively. As mentioned in R19, it could be a miscalculation of host galaxy colour excesses of the SNe in the calibration set and/or the SNe used in the HD.

x	rms ^a	H_0^a	rms ^b	H_0^b
B	0.41	$79.1 \pm 5.1 \pm 8.9$	0.26	$71.8 \pm 2.4 \pm 2.9$
V	0.26	$72.6 \pm 3.2 \pm 6.5$	0.24	$67.9 \pm 2.4 \pm 2.8$
I	0.22	$69.3 \pm 2.5 \pm 4.2$	0.24	$67.1 \pm 2.3 \pm 2.7$
J	0.22	$70.4 \pm 2.0 \pm 3.2$	0.21	$69.4 \pm 1.9 \pm 2.8$
H	0.21	$69.9 \pm 1.7 \pm 3.0$	0.21	$69.8 \pm 1.6 \pm 2.8$

Note: H_0 values in units of $\text{km s}^{-1} \text{Mpc}^{-1}$, where the first error is statistical and the second one is systematic.

^a Using $V-I$ versus $B-V$ C3 colour excesses.

^b Using the $V-I$ colour-term correction.

Table 3.5: Hubble diagram parameters.

3.4.2 Dependence on $V-I$

In this work, we explore to replace the host galaxy broad-band extinction correction by a colour-term correction. This correction, first applied to SNe II distances by Nugent et al. (2006) and then performed in other works (e.g., Poznanski et al. 2009; Olivares E. et al. 2010; D’Andrea et al. 2010; de Jaeger et al. 2015; de Jaeger et al. 2017a; Gall et al. 2018), accounts for the host galaxy colour excess, and also corrects for any other dependence of the absolute magnitude on the intrinsic colour (de Jaeger et al. 2015).

Among the colours that can be constructed with the $BVIJH$ bands, we choose to work with $V-I$ because the flux in V - and I -band is less affected by line blanketing than the B -band flux, and because the photometry errors for those bands are lower than for near-IR ones. Apply the colour-term correction implies to rewrite equation 3.5 as

$$\mu_{x,i}^* = \mu_{x,i}^{*,AK} - \beta_x \cdot (V-I)_{AK,i}, \quad (3.23)$$

where β_x is a free parameter that represent the strength of the colour-term correction for the x -band.

We also have to replace the weights given in equation 3.7 by

$$w_{x,i} = \left[\sigma_{m_{x,i}}^2 + \left(\frac{5}{\ln 10} \frac{\sigma_{v_{ph,i}}}{v_{ph,i}} \right)^2 + \beta_x^2 \sigma_{(V-I)_i} \right]^{-1}, \quad (3.24)$$

and delete the last line of equation 3.8. In order to compute β_x along with c_x , $n_{\text{HD},x}^*$, and $\sigma_{x,0}$, we minimize equation 3.17. Values of $n_{\text{HD},x}^*$, c_x , β_x , and $\sigma_{x,0}$, along with their rms errors are summarized in Column 2, 3, 4, and 5 of Table 3.6, respectively.

x	$n_{\text{HD},x}^*$	c_x	β_x	$\sigma_{x,0}$	ZP_x
B	$-4.72(15)$	$2.62(29)$	$2.67(18)$	$0.14(05)$	$-20.96(13)$
V	$-4.89(17)$	$2.11(28)$	$1.79(27)$	$0.12(05)$	$-21.01(12)$
I	$-4.90(15)$	$2.11(29)$	$0.81(26)$	$0.13(04)$	$-20.81(12)$
J	$-5.08(18)$	$2.33(28)$	$0.23(19)$	$0.12(03)$	$-20.77(09)$
H	$-5.04(20)$	$2.12(35)$	$0.04(20)$	$0.14(04)$	$-20.79(07)$

Note: Using the $V-I$ colour-term correction. Parameters are valid for $35 \text{ d} < \Delta t < 75 \text{ d}$. The rms errors are in parenthesis in units of 0.01.

Table 3.6: PMM parameters using $V-I$ correction.

Fig. 3.3 shows the HDs for $BVIJH$ bands with PMM pseudo-distances corrected for the $V-I$ colour-term. For B -bands we obtain a HD rms of 0.26 mag, which is 0.32 mag lower in quadrature than the value using C3 host galaxy colour excesses, and compares to the HD rms of 0.24 mag obtained for V - and I -band. For J - and H -band we obtained a HD rms of 0.21 mag, which is 0.12–0.15 mag lower in quadrature than the values obtained for optical bands. Since we obtain better results for BVI bands using the $V-I$ colour-term correction, hereafter we will analyse results obtained with this correction term.

In order to convert pseudo-distance moduli corrected for the $V-I$ colour-term to distance moduli in the Jang and Lee (2017b) scale, we compute new ZP_x values using equation 3.22. These values are listed in Column 6 of Table 3.6, while Table 3.7 summarizes the distance moduli.

The $n_{\text{HD},x}^*$ and $\sigma_{x,0}$ values for $BVIJH$ bands are summarized in Column 3 and 4 of Table 3.4, respectively.

The H_0 values for $BVIJH$ bands using PMM distances corrected for $V-I$ colour-term are listed in Column 5 of Table 3.5. These values range between 67.1 and $71.8 \text{ km s}^{-1} \text{ Mpc}^{-1}$, and are consistent within their errors with the Jang and Lee (2017a) H_0 value. Since the H -band is less affected by dust than the other ones, the H_0 value of $69.8 \pm 1.6(\text{stat}) \pm 2.8(\text{sys}) \text{ km s}^{-1} \text{ Mpc}^{-1}$ is our best estimation.

3.4.3 Second-order dependences

In order to test whether we can improve the PMM distance precision with data we have, we explore possible dependences of the SN II absolute magnitude on two additional parameters: the slope of

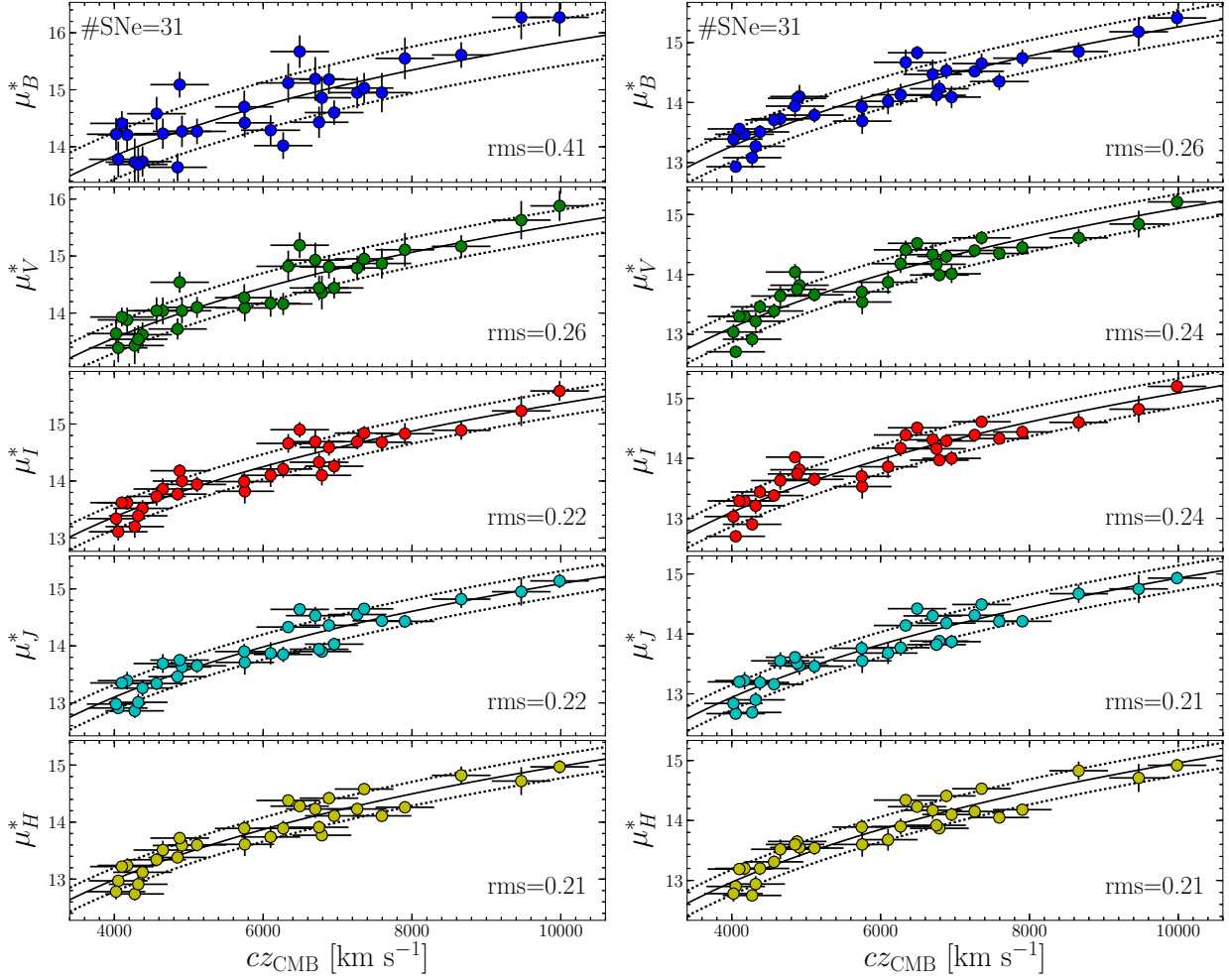


Figure 3.3: Hubble diagrams for 31 SNe II with PMM distances corrected for host galaxy colour excess measured with the C3 method (left) and corrected for the $V-I$ colour-term (right). Solid lines correspond to Hubble law fits. Dotted lines indicate values within one rms.

Galaxy ^a	cz_{CMB} (km s^{-1})	SN	μ_B	μ_V	μ_I	μ_J	μ_H
IC 340	4023(382)	2018hle	33.86(0.14)	33.79(0.14)	33.81(0.13)	33.70(0.13)	33.60(0.12)
NGC 3660	4053(383)	2017byz	33.39(0.09)	33.45(0.09)	33.47(0.08)	33.54(0.07)	33.72(0.06)
ESO 504–G9	4101(415) ^b	2016ase	34.03(0.09)	34.06(0.08)	34.08(0.07)	34.05(0.06)	34.02(0.06)
LEDA 831618	4172(385)	2003bn	33.93(0.08)	34.05(0.08)	34.07(0.07)	34.07(0.14)	34.02(0.11)
NGC 716	4274(383)	2017fqo	33.52(0.17)	33.66(0.13)	33.68(0.10)	33.56(0.08)	33.56(0.08)
2MASX J08494084–0805303	4321(383)	2017hca	33.73(0.13)	33.96(0.14)	33.98(0.14)	33.76(0.12)	33.76(0.12)
MCG –4–12–4	4379(382)	2003E	33.97(0.12)	34.20(0.11)	34.22(0.11)	34.07(0.13)	34.02(0.11)
MCG –1–26–3	4568(384)	2017cfa	34.17(0.13)	34.13(0.13)	34.16(0.11)	34.02(0.10)	34.13(0.10)
NGC 5374	4652(383)	2003bl	34.18(0.14)	34.39(0.16)	34.41(0.16)	34.41(0.14)	34.33(0.15)
IC 221	4850(382)	2017gtd	34.42(0.18)	34.78(0.14)	34.80(0.09)	34.47(0.06)	34.42(0.05)
NGC 7816	4878(383)	2017gww	34.53(0.13)	34.50(0.11)	34.52(0.09)	34.37(0.07)	34.48(0.09)
IC 991	4909(382)	2017ffk	34.55(0.19)	34.57(0.17)	34.59(0.16)	34.34(0.14)	34.38(0.14)
MCG –1–10–19	5111(382)	2018kpo	34.24(0.12)	34.41(0.12)	34.43(0.12)	34.33(0.12)	34.37(0.11)
ESO 155–G36	5746(383)	2017gry	34.40(0.18)	34.46(0.16)	34.48(0.14)	34.62(0.12)	34.71(0.12)
IC 849	5753(383)	2003cn	34.15(0.20)	34.29(0.20)	34.31(0.20)	34.42(0.20)	34.43(0.19)
AGC 203753	6100(386)	2016iyk	34.45(0.20)	34.62(0.19)	34.64(0.18)	34.55(0.18)	34.51(0.18)
PGC 90644	6269(382)	2016hbd	34.58(0.18)	34.93(0.16)	34.95(0.14)	34.63(0.13)	34.72(0.13)
2MASX J03312172+0408161	6337(417) ^b	2017ilo	35.12(0.21)	35.16(0.15)	35.17(0.11)	35.01(0.07)	35.16(0.06)
SDSS J121246.44+002432.6	6491(383)	2017ays	35.28(0.12)	35.27(0.10)	35.29(0.08)	35.29(0.07)	35.05(0.08)
UGC 2705	6700(383)	2017jcu	34.92(0.24)	35.07(0.18)	35.09(0.14)	35.17(0.13)	34.99(0.14)
ESO 448–G4	6751(385)	2018dza	34.57(0.17)	34.92(0.14)	34.94(0.12)	34.69(0.11)	34.74(0.10)
ESO 293–G22	6789(385)	2017hxj	34.70(0.14)	34.73(0.11)	34.75(0.08)	34.73(0.06)	34.69(0.05)
NPM1G +04.0097	6884(382)	2002hj	34.98(0.14)	35.04(0.12)	35.06(0.11)	35.05(0.09)	35.23(0.09)
CGCG 7–19	6954(383)	2017zg	34.54(0.18)	34.76(0.15)	34.78(0.13)	34.74(0.11)	34.92(0.11)
SDSS J133313.38+080325.3	7264(383)	2017anf	35.03(0.10)	35.15(0.09)	35.17(0.07)	35.19(0.06)	34.97(0.07)
CGCG 40–65	7357(383)	2018ub	35.10(0.16)	35.37(0.12)	35.39(0.09)	35.35(0.06)	35.36(0.06)
6dF J2322161–234204	7595(385)	2017gqg	34.78(0.14)	35.09(0.11)	35.11(0.09)	35.09(0.06)	34.87(0.06)
2MASX J08533957–2503294	7905(383)	2018hi	35.19(0.14)	35.20(0.13)	35.22(0.11)	35.07(0.09)	35.00(0.08)
UGC 4864	8662(383)	2003T	35.30(0.15)	35.36(0.15)	35.38(0.15)	35.54(0.14)	35.65(0.14)
UGC 6212	9468(384)	2003ci	35.65(0.24)	35.58(0.23)	35.59(0.22)	35.62(0.22)	35.52(0.23)
CGCG 29–27	9984(383)	2017jfa	35.87(0.16)	35.96(0.14)	35.98(0.12)	35.79(0.11)	35.74(0.10)

Note: The rms errors are in parenthesis, and include the TRGB zero-point systematic error.

^aSorted by increasing redshift.

^bWithout redshift measurement of the host galaxy nucleus, so to compute cz_{CMB} we use the heliocentric SN redshift.

Table 3.7: CMB redshifts and PMM distance moduli.

Correction terms	rms(HD)				
	<i>B</i>	<i>V</i>	<i>I</i>	<i>J</i>	<i>H</i>
$\beta_x \cdot (V-I)_{AK,i}$	0.26	0.24	0.24	0.21	0.21
$\beta_x \cdot (V-I)_{AK,i}, \alpha_x s_2$	0.25	0.24	0.24	0.21	0.21
$\beta_x \cdot (V-I)_{AK,i}, \gamma_x v_{ph,i}$	0.26	0.24	0.24	0.22	0.22
$\beta_x \cdot (V-I)_{AK,i}, \alpha_x s_2, \gamma_x v_{ph,i}$	0.26	0.24	0.24	0.21	0.22

Table 3.8: HD rms for different PMM correction terms.

the *V*-band light curve during the plateau, s_2 , and an extra dependence on v_{ph} . The inclusion of s_2 is justified based on the empirical correlation between s_2 and the SN II absolute magnitude at different epochs (Anderson et al. 2014b; de Jaeger et al. 2015), while the extra dependence on v_{ph} is justified because, as part of SCM formalism, the factor 5 in the last term of equation 3.1 is leaved as a free parameter. In both cases, we consider first-order corrections.

To quantify the benefits of including the s_2 and v_{ph} corrections, we minimize equation 3.17 and compute HD rms values for the following configurations: (1) with $V-I$ colour-term and s_2 correction; (2) with $V-I$ colour-term and v_{ph} correction; and (3) with $V-I$ colour-term, v_{ph} , and s_2 correction.

Table 3.8 lists the HD rms values for *BVIJH* bands and for the corrections mentioned above. Since we do not gain more distance precision including second-order corrections, we conclude that the inclusion of those corrections are not necessary.

3.4.4 Statistical significance of the result

Suppose we have independent measurements of N residuals of a regression with k free parameters. If those measurements come from a normal parent population with standard deviation σ , then the confidence intervals on σ at a confidence level (CL) of $100(1 - \alpha)$ per cent are given by

$$\text{rms} \sqrt{\frac{(N-k)}{Q_{1-\frac{\alpha}{2}, N-1}}} \leq \sigma \leq \text{rms} \sqrt{\frac{(N-k)}{Q_{\frac{\alpha}{2}, N-1}}}, \quad (3.25)$$

where $Q_{p, N-1}$ is the quantile function of the chi-squared distribution with $N-1$ degrees of freedom. To test the normality of the parent population, we check the normality of the residuals. For the latter, we use the Rescaled Moment (RM) test (Imon 2003; Rana et al. 2009), which is suitable to verify normality of regression residuals.

Applying the RM test to the residuals of our HDs ($N = 31$) with distances corrected for the $V-I$ colour-term ($k = 4$), we obtain p -values > 0.22 for $BVIJH$ bands, which indicates that the hypothesis that residuals are normally distributed cannot be rejected (78 per cent CL). For the J - and H -band HD, where $\text{rms} = 0.21$ mag, using equation 3.25 we obtain $0.16 \text{ mag} \leq \sigma \leq 0.27 \text{ mag}$ (95 per cent CL). Therefore, we can set the PMM distance precision with JH bands to be $9.7^{+2.6}_{-2.4}$ per cent (95 per cent CL). This result is consistent with that of R19 where, from the analysis of 15 SNe II, they obtained that the PMM distance precision with the J -band could be as high as 10 per cent (99 per cent CL). Performing the same analysis for optical bands, we obtain $12.0^{+3.2}_{-2.9}$ and $11.1^{+2.9}_{-2.7}$ per cent (95 per cent CL) for B and VI bands, respectively.

3.5 DISCUSSION

3.5.1 Error budget

In R19 it was established that the PMM distance statistical error for the J -band can be reduced if a better method to correct for host galaxy colour excess and using SNe II with better constrained explosion epoch. Those two error sources induce 60.6 per cent of the total statistical error in the R19 work.

In Table 3.9 we show the error budget with the contribution of all terms to the total error. With our new set of SNe II with well constrained explosion epoch, and using the $V-I$ colour-term correction to account for host galaxy colour excess and intrinsic dependence of the absolute magnitude on that color, we reduce the error induced by uncertainties on t_0 and E_{B-V}^h to 13.2 per cent of the total error. The error budget is dominated by errors on the PMM zero-point, the observed photometry (which in our case, does not have template subtraction), and expansion velocities, which correspond to the 67 per cent of the total error. Therefore, in future works it is possible to reduce the errors on PMM distances including more SNe II to compute ZP_x , increasing the quality of the near-IR photometry, and also including more spectral lines (not only Fe II $\lambda 5169$) to estimate v_{ph} .

Error source	Typical error	Error on μ_J (mag)	Per cent of total error
ZP_J	0.045 mag ^a	0.045	23.0
m_J	0.045 mag	0.045	23.0
v_{ph}	79 km s ⁻¹	0.043	21.0
$cz_{\text{helio}}^{\text{SN}}$	75 km s ⁻¹	0.041	19.1
t_0	1.1 days	0.029	9.5
$V-I$	0.037 mag	0.018	3.7
K_J	0.006 mag	0.006	0.4
A_J^G	0.006 mag	0.006	0.4
Total		0.094	100.0

^aIt does not include the TRGB zero-point systematic error.

Table 3.9: Error budget for the PMM J -band distances.

3.5.2 Photometric systematics

As mentioned in Section 3.2.1, we remove the host galaxy background adopting a low-order polynomial fit. The latter is considered acceptable when the host galaxy contamination is not relevant, otherwise template images taken 1.5 years after the SN explosion are necessary to remove the light from the host galaxy. We therefore expect to reduce the HD scatter in all bands once we perform the template subtraction.

Other source of systematics is the difference between the photometric systems of the instruments we use for imaging. This systematic mainly affects the flux measured with optical band than near-IR ones, and mainly the flux measured with the I -band (Pignata et al. 2004). We expect that performing the S -correction (Stritzinger et al. 2002; Krisciunas et al. 2003; Pignata et al. 2004) we can reduce the HD scatter for the B -, V , and specially for the I -band.

3.6 CONCLUSIONS

In this work we used $BVIJH$ photometry and optical spectroscopy of 24 SNe II at $0.013 < z < 0.033$ to compute their distance moduli with the PMM. The main goal was to measure the PMM distance precision with $BVIJH$ bands in order to stablish which one gives the best performance. Removing two SNe from our set, and combining with seven SNe II at $z > 0.013$ used in R19, we constructed

BVIJH HDs with 31 SNe II. To estimate the PMM distance precision from HDs, we computed rms values around the Hubble law fits.

Our main results are the following:

1. Correcting PMM distances for host galaxy colour excess using values measured with the C3 method, we obtained HD rms values of 0.22–0.40 mag for *BVI* bands and 0.21 mag for *J* and *H* ones.
2. Replacing host galaxy color excesses for a $V-I$ colour-term correction, the HD rms for *BVI* bands was reduced to 0.24–0.26 mag for *BVI* bands, while for the *J*- and *H*-band the HD rms remained fixed at 0.21 mag. The HD rms values for *BVIJH* bands were not improved including linear-term corrections on s_2 and v_{ph} .
3. The HD rms for the *J*- and *H*-band we obtained translates into a PMM distance precision of $9.7^{+2.6}_{-2.4}$ per cent (95 per cent CL).
4. Using the *H*-band HD, we obtained $H_0 = 69.8 \pm 1.6(\text{stat}) \pm 2.8(\text{sys}) \text{ km s}^{-1} \text{ Mpc}^{-1}$. This value is consistent with the value of $71.17 \pm 1.66(\text{stat}) \pm 1.87(\text{sys}) \text{ km s}^{-1} \text{ Mpc}^{-1}$ reported by Jang and Lee (2017a), which used the same TRGB calibration of Jang and Lee (2017b) that we used in this work.

Chapter 4

LUMINOUS TYPE II SUPERNOVAE WITH LOW EXPANSION VELOCITIES

4.1 INTRODUCTION

Type II supernovae (SNe II; Minkowski [1941](#)) are the final stage of evolution of stars with an initial mass between 8.0 and 16.5 M_{\odot} (Smartt et al. [2009](#)), that retain a significant fraction of hydrogen in their envelopes before the moment of the collapse of their iron cores. Among SNe II, three special sub-types have been identified based on photometric and spectroscopic characteristics: those showing hydrogen in early spectra that soon disappear (SNe Iib; Woosley et al. [1987](#); Filippenko [1988](#)), those having light curves similar to SN 1987A (1987A-like SNe, e.g., Hamuy et al. [1988](#)), and those showing narrow hydrogen emission lines in the spectra due to the interaction of the ejecta with a circumstellar medium (CSM) (SNe IIn; Schlegel [1990](#)). For the rest of SNe II (77 per cent; Shivvers et al. [2017](#), which show a range in luminosity decline rates) we will refer as normal SNe II.

With the increasing number of discovered SNe II, more exotic events are being revealed. An example of this is LSQ13fn (Polshaw et al. [2016](#)), which has interesting properties: (1) it has bluer colours than normal SNe II, (2) it shows evidence of an early ejecta-CSM interaction, (3) there is a weakness of metal lines in the spectra, and (4) it has low expansion velocities, with values between the subluminal SN II 2005cs (Pastorello et al. [2006](#); Pastorello et al. [2009](#)) and the archetypal SN II 1999em (Hamuy et al. [2001](#); Leonard et al. [2002](#); Elmhamdi et al. [2003](#)), but having a luminosity comparable to the luminous SN II 2004et (Sahu et al. [2006](#); Misra et al. [2007](#); Maguire et al.

2010a). In addition to LSQ13fn, SN 1983K was also reported showing some of the aforementioned characteristics (Niemela et al. 1985; Phillips et al. 1990). SN 1983K and LSQ13fn, being more luminous than the expected from their expansion velocities, break the luminosity-expansion velocity relation found by Hamuy and Pinto (2002) for normal SNe II (and used for distance measurements). Polshaw et al. (2016) suggested a combined effect of a residual thermal energy from the early ejecta-CSM interaction, a low metallicity and a large radius of the progenitor to explain the peculiarities seen in LSQ13fn. In this work we present optical and near-IR photometry of SN 2008bm, SN 2009aj, and SN 2009au, which show similar properties to those seen in SN 1983K and LSQ13fn. Throughout this paper we identify this sample of SNe II using the acronym Luminous with Low Expansion Velocities (LLEV) SNe II.

We organize our work as follows. In Section 4.2 we present the relevant information on our SN data-set and their host galaxies. Photometry along with the description of the data reduction is presented in Section 4.3. In Section 4.4 and 4.5, we contrast the properties of the LLEV SNe II with those of other SNe II. In Section 4.6 we discuss a possible scenario that could explain the peculiar characteristics seen in the LLEV SNe II. We also present an estimation of the fraction of LLEV SNe II in Section 4.6.3 and their impact on the use of normal SNe II as distance indicators in Section 4.6.4. We present our conclusions in Section 4.7.

4.2 SUPERNOVAE AND HOST GALAXIES

Table 4.1 lists the main parameters for SN 2008bm, SN 2009aj, SN 2009au, and their host galaxies. Throughout this work we assume the extinction curve given by Fitzpatrick (1999) with $R_V = 3.1$. We also assume $H_0 = 73 \text{ km s}^{-1} \text{ Mpc}^{-1}$, $\Omega_m = 0.27$, $\Omega_\Lambda = 0.73$, and a recessional velocity error of 382 km s^{-1} due to peculiar velocities (Wang et al. 2006).

4.2.1 SN 2008bm

SN 2008bm was discovered in the galaxy CGCG 71–101 on 2008 March 29.3 UT (Drake et al. 2008). The last non-detection was on January 31.5 UT, therefore the explosion epoch is not well

SN data	1983K	2008bm	2009aj	2009au	LSQ13fn
RA (J2000.0)	12:46:36.41	13:02:58.78	13:56:45.33	12:59:46.00	11:51:17.29
DEC (J2000.0)	−8:21:21.9	+10:30:27.0	−48:29:36.2	−29:36:07.5	−29:36:41.10
Host galaxy	NGC 4699	CGCG 71–101	ESO 221–G18	ESO 443–G21	LEDA 727284
Host type ^a	SAB(rs)b	Sc	Sa?	Scd	Sa ^e
Distance modulus (mag)	31.50 ± 0.35	35.66 ± 0.08	33.89 ± 0.20	33.31 ± 0.22	37.21 ± 0.05
E_{B-V}^{MW} (mag) ^b	0.015 ± 0.002	0.022 ± 0.003	0.124 ± 0.020	0.079 ± 0.013	0.054 ± 0.009
E_{B-V}^{host} (mag)	0.0 ^d	0.00 ± 0.02	0.00 ± 0.01	≥ 0.2	0.0 ^e
Explosion epoch (MJD)	45490.1 ± 1.0	54525.4 ± 28.9	54879.8 ± 6.5	54897.2 ± 4.0	56299.2 ± 1.0
SN heliocentric redshift (km s ^{−1})	1394 ± 162	9628 ± 25	2883 ± 162	2875 ± 30	18900 ± 300 ^e
12+log(O/H) (dex) ^c	8.55 [†]	8.33 ± 0.02*	8.29 ± 0.03*	8.56 ± 0.03*	< 8.50 ± 0.16 [⊗]
s_2 (mag (100 d) ^{−1})	0.78 ± 0.14	2.78 ± 0.14	0.82 ± 0.02	3.04 ± 0.04	1.08 ± 0.08
M_V^{max} (mag)	−18.53 ± 0.36	−17.96 ± 0.12	−18.77 ± 0.21	≤ −17.07 ± 0.25	−17.95 ± 0.21
M_V^{50d} (mag)	−18.43 ± 0.35	−17.75 ± 0.43	−17.81 ± 0.22	≤ −16.08 ± 0.26	−17.33 ± 0.07
$v_{FeII,50d}$ (km s ^{−1})	2362 ± 205	1275 ± 82	2336 ± 181	1549 ± 40	2350 ± 608
⁵⁶ Ni mass (M _⊙)	0.053 ± 0.018	0.012 ± 0.004	0.034 ± 0.009	≥ 0.011	~ 0.02 ^e

^a From NASA/IPAC Extragalactic Database, unless otherwise noted.

^b Galactic colour excesses from Schlafly and Finkbeiner (2011), with an uncertainty of 16% (Schlegel et al. 1998).

^c Oxygen abundances, in the N2 calibration of Marino et al. (2013), measured by Kuncarayakti et al. (2018) (†), Anderson et al. (2016) (*), or Polshaw et al. (2016) (⊗). The latter is a recalibration of the original value reported in the N2 calibration of Pettini and Pagel (2004).

^d Values from Niemela et al. (1985).

^e Values from Polshaw et al. (2016).

Table 4.1: SN and host galaxy parameters of the LLEV SN II sample.

constrained (JD 2454525.9 ± 28.9). The event was classified as an SN IIn a couple of months past explosion based on a spectrum obtained on April 7.1 UT (Stritzinger and Morrell 2008). However, later spectra (see Gutiérrez et al. 2017, hereafter G17) show clear Balmer absorption lines, typically seen in normal SNe II.

CGCG 71–101 has a recessional velocity of 9875 km s^{−1}, which translates into a distance modulus of 35.66 ± 0.08 mag. No Na I D absorption at the redshift of the host galaxy was detected in the SN spectra, indicating a negligible host galaxy colour excess ($E_{B-V}^{host} = 0.00 ± 0.02$ mag, Anderson et al. 2014b, hereafter A14). SN 2008bm is located at a projected distance of 9.3 ± 0.3 kpc from the center of the apparently nearly face-on host galaxy, supporting the low reddening scenario.

4.2.2 SN 2009aj

SN 2009aj was discovered in the galaxy ESO 221–G18 on 2009 February 24.3 UT (Pignata et al. 2009a). Nothing was visible at the SN position on February 11.2 UT, therefore the explosion epoch is constrained to occur at JD 2454880.3 ± 6.5. The event was classified by Stritzinger et al. (2009) as an SN IIn around maximum and reminiscent of SN 1983K.

We do not detect the presence of Na ID at the redshift of the host galaxy in the SN spectra, which indicates a negligible host galaxy reddening. Using the procedure described in A14 and the relation of Poznanski et al. (2012) we obtain $E_{B-V}^{\text{host}} = 0.00 \pm 0.01$ mag, which we adopt as the host galaxy colour excess. ESO 221–G18 has a recessional velocity corrected for the infall of the Local Group toward the Virgo cluster and the Great Attractor of $4380 \pm 112 \text{ km s}^{-1}$, which translates into a distance modulus of 33.89 ± 0.20 mag.

4.2.3 SN 2009au

SN 2009au was discovered in the galaxy ESO 443–G21 on 2009 March 11.2 UT (Pignata et al. 2009b). Nothing was visible at the SN position on March 3.2 UT, therefore the explosion epoch is constrained to occur at $\text{JD } 2454897.7 \pm 4.0$. The event appeared to be a young SN IIn soon after explosion (Stritzinger et al. 2009), however later spectra (see G17) show clear Balmer absorption features.

The distance modulus to ESO 443–G21 is estimated using the Tully-Fisher relation to be 33.44 ± 0.45 mag (Tully et al. 2016). In addition, ESO 443–G21 is member of the galaxy group HDCE 754 (Crook et al. 2007), which has a recessional velocity corrected for Virgo infall of 3287 km s^{-1} , which translates into a distance modulus of 33.27 ± 0.25 mag. We adopt the weighted mean of these values, i.e., $\mu = 33.31 \pm 0.22$ mag, as the distance to ESO 443–G21.

SN 2009au is located at a projected distance of 1.7 ± 0.1 kpc from the center of the nearly edge-on host galaxy, so the SN could be affected by a high amount of extinction. We measured a Na ID pseudo equivalent width (pEW) of $1.33 \pm 0.21 \text{ \AA}$ at the redshift of the host galaxy in the SN spectra, corresponding to $E_{B-V}^{\text{host}} = 0.51 \pm 0.30$ mag using the relation of Poznanski et al. (2012). This value is consistent within the error with the E_{B-V}^{host} values of 0.20 and 0.64 mag obtained with the relations of Turatto et al. (2003). However, since the Na ID pEW becomes insensitive to estimate reddening for $\text{pEW} > 1.0 \text{ \AA}$ (Phillips et al. 2013), the E_{B-V}^{host} value derived for SN 2009au is quite uncertain and, therefore, it has to be taken with caution. On the other hand, SN 2009au has an absolute V -band magnitude at maximum, uncorrected for E_{B-V}^{host} , of -16.45 ± 0.25 mag, while the value expected from its V -band decline rate and the relation given in A14 (left part of Figure 20) is of -17.90 ± 0.83 mag.

If the difference is due to the host galaxy colour excess, then we obtain $E_{B-V}^{\text{host}} = 0.47 \pm 0.28$ mag, quite consistent with the estimation from Na ID pEW. For SN 2009au, we will adopt a minimum value of 0.2 mag for E_{B-V}^{host} .

4.3 OBSERVATIONAL MATERIAL

Optical and near-IR images of SN 2008bm, SN 2009aj, and SN 2009au were obtained over the course of the Carnegie Supernova Project I (CSP-I; Hamuy et al. 2006). Landolt *BV* and Sloan *ugri* images were obtained mostly with the 1-m Swope telescope at Las Campanas Observatory, while near-IR *YJH* images were obtained with both the 1-m Swope and the 2.5-m du Pont telescope.

The CSP-I data reduction is described in Contreras et al. (2010). For optical images, it consists of: bias subtraction, flat-field correction, a linearity correction, and an exposure-time correction for a shutter time delay. For near-IR images, it consists of: dark subtraction, flat-field division, sky subtraction, geometric alignment and combination of the dithered images.

In addition, Landolt *UBVRI* and Sloan *griz* images of SN 2009aj and SN 2009au were also obtained with the 41-cm Panchromatic Robotic Optical Monitoring and Polarimetry Telescopes (PROMPT; Reichart et al. 2005), as part of the Chilean Automatic Supernova Search (CHASE; Pignata et al. 2009c) follow-up program. Data reduction includes bias-subtraction, overscan correction, flat-field correction, and image combination.

Images of the SNe host galaxies 1.2–4.1 years after the SN explosion were obtained in order to remove the host galaxy contamination. Instrumental magnitudes were measured using the point spread function (PSF) technique. Final magnitudes were computed with respect to a local sequence of stars, which are calibrated using Landolt (1992) *UBVRI*, Smith et al. (2002) *ugriz*, and Persson et al. (1998) *JHK* standard stars (*J*- and *K*-band observations are used to derive *Y*-band magnitudes of the standard stars, see Hamuy et al. 2006).

Tables 5.12–5.16 list the photometry of SN 2008bm, SN 2009aj, and SN 2009au, while Fig. 4.1 shows the optical and near-IR light curves of SN 2008bm (top), SN 2009aj (middle), and SN 2009au (bottom).

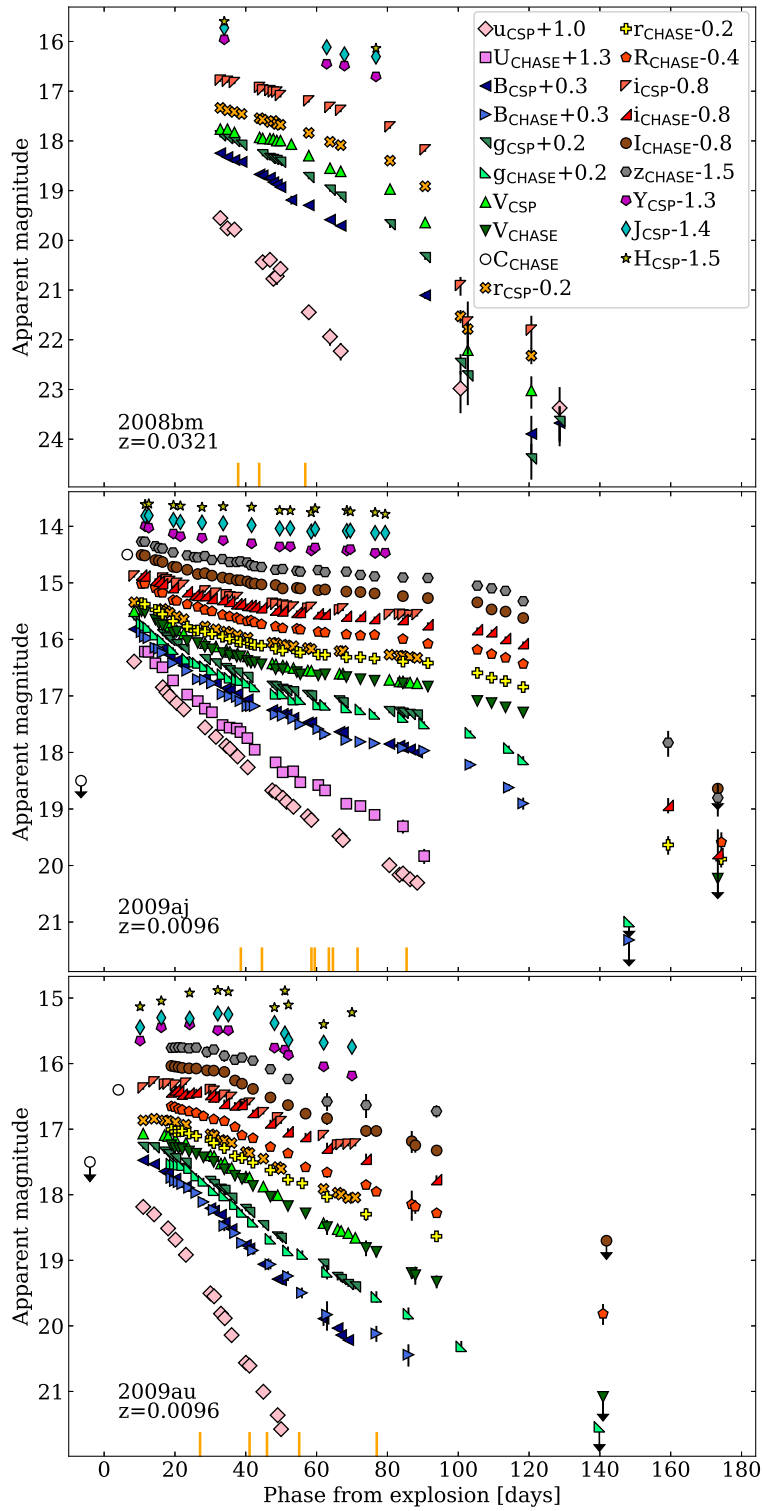


Figure 4.1: Light curves of SN 2008bm (top), SN 2009aj (middle), and SN 2009au (bottom). Bands and magnitude shifts with respect to the original values are in the legend. Arrows indicate upper limits, while orange ticks mark the epochs of the spectroscopy.

4.3.1 Sample of supernovae

In addition to SN 2008bm, SN 2009aj, and SN 2009au, we include SN 1983K (Niemela et al. 1985; Phillips et al. 1990) and LSQ13fn (Polshaw et al. 2016) into the analysis, given the similarity of their photometric and spectral properties (see Section 4.4 and 4.5). For SN 1983K we estimate the explosion epoch through a polynomial fit to the *B*-band rise photometry to be $\text{JD } 2445490.6 \pm 1.0$. The distance modulus to the host of SN 1983K, NGC 4699, is estimated with the Tully-Fisher relation to be 31.45 ± 0.45 mag (Tully et al. 2016). In addition, NGC 4699 is member of the galaxy group HDCE 740 (Crook et al. 2007), which has a distance modulus of 31.57 ± 0.55 mag, so we adopt the weighted average ($\mu = 31.50 \pm 0.35$ mag) as the NGC 4699 distance modulus. Early-time photometry of LSQ13fn was obtained as part of the La Silla-Quest Variability Survey (LSQ; Baltay et al. 2013), where the first detection was on 2013 January 8.2 UT, while the last non detection was on January 6.2 UT, so the explosion epoch is $\text{JD } 2456299.7 \pm 1.0$. The main parameters for SN 1983K, LSQ13fn, and their host galaxies are summarized in Table 4.1.

In the below analysis we also include the optical spectroscopy for SN 2008bm, SN 2009aj, and SN 2009au also obtained by the CSP-I and already published in G17.

4.4 PHOTOMETRIC PROPERTIES

In this section we compare photometric properties of the LLEV SNe II with those of other SNe II. For the analysis in this section, we exclude SN 2009au due to the uncertainty in the E_{B-V}^{host} correction (see Section 4.2.3).

4.4.1 Peak magnitude versus decline rate

Analysing a set of 116 SN II *V*-band light curves, A14 found a correlation between the absolute *V*-band magnitude at maximum (M_V^{max}) and the decline rate of the second, shallower slope in the light curve (s_2), which suggests a continuum in the normal SN II population in this parameter space. Similar peak magnitude-decline rate correlations were also obtained by Sanders et al. (2015),

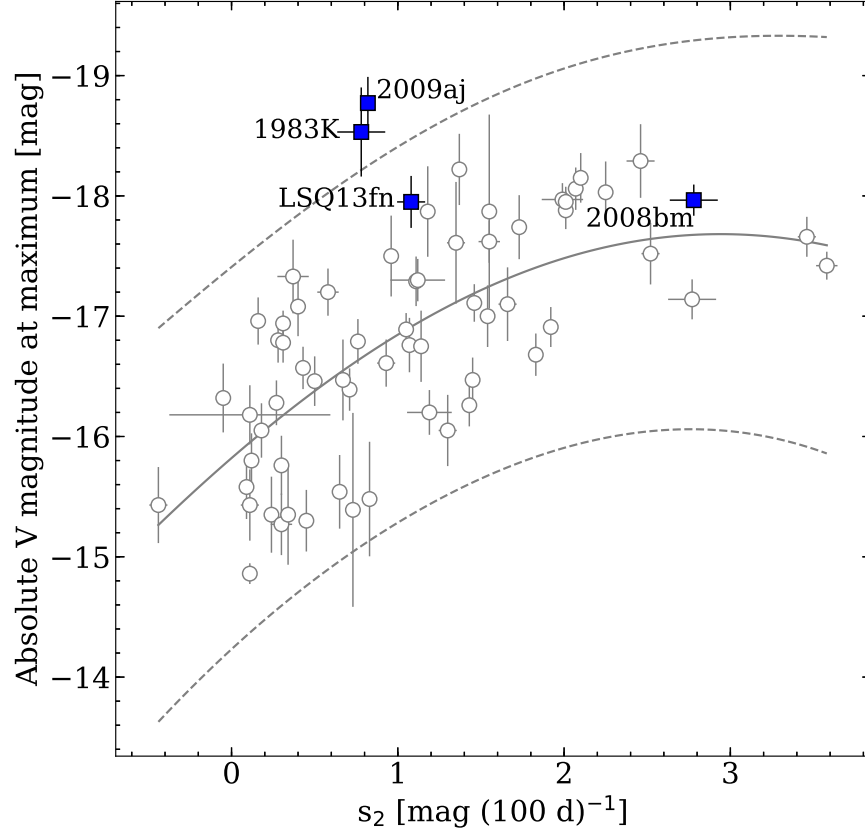


Figure 4.2: Absolute V-band magnitude at maximum versus V-band decline rate during the plateau (s_2), showing the LLEV SNe II in our set (blue squares) and the normal SNe II in the A14 sample corrected for E_{B-V}^{host} (empty circles). The solid line corresponds to the Gaussian process fit, where dashed lines indicate the 3σ error around the fit.

Galbany et al. (2016), and Valenti et al. (2016).

The first V -band photometric points of SN 2009aj and SN 2009au are obtained around the maximum (see Fig. 4.1), so we use those values to estimate M_V^{\max} . In the case of SN 1983K and SN 2008bm, the V -band maximum is not observed because the V -band light curve of SN 1983K is poorly sampled, and the photometry of SN 2008bm is not early enough (see Fig. 4.1). For the latter two cases, we use the first V -band photometric point to compute M_V^{\max} . The V -band light curve of LSQ13fn has a clear maximum, which we use to calculate M_V^{\max} . Values of M_V^{\max} and s_2 for our SN set are listed in Table 4.1.

Fig. 4.2 shows the SNe II in the A14 sample¹ (empty circles; where values are from Table 6 of A14), where we remove those SNe that were not corrected for E_{B-V}^{host} . To characterize the distribution of the A14 sample in the M_V^{\max} versus s_2 space, we perform a Gaussian process fit (solid line). In Fig. 4.2 we plot the LLEV SNe II as blue squares. We see that they have $M_V^{\max} \lesssim -18.0$ mag, where SN 2008bm is a fast decliner (like SN 2009au, which has the highest decline rate in the LLEV SNe II set), while for SN 1983K, SN 2009aj, and LSQ13fn the decline rate is lower, indicating that LLEV SNe II seems not to arise from normal SNe II with a particular light curve decline rate. In addition, We see that SN 2008bm, and LSQ13fn are within 3σ (dashed lines), while SN 1983K and SN 2009aj are outliers in the distribution, i.e., they are significantly brighter than what would be implied from their s_2 decline rates.

4.4.2 Pseudo-bolometric light curves

To compute pseudo-bolometric light curves, we proceed as follows: (1) We convert broad-band magnitudes into fluxes where, for a fair comparison with other SNe II in the literature, we use $BVRI$ and gri magnitudes. (2) For each photometric epoch, we perform linear interpolations between fluxes, which we adopt as a proxy for the spectral energy distribution (SED). (3) We correct the SED for redshift and colour excess, and then we integrate over the wavelength range covered by the filters. (4) We convert the integrated flux into luminosity using the corresponding SN distance.

The top part of Fig. 4.3 shows the $BVRI$ pseudo-bolometric light curves of the LLEV SNe II in our

¹This SN sample contains SN 2008bm and SN 2009au, which we remove since they are in the LLEV SN II sample.

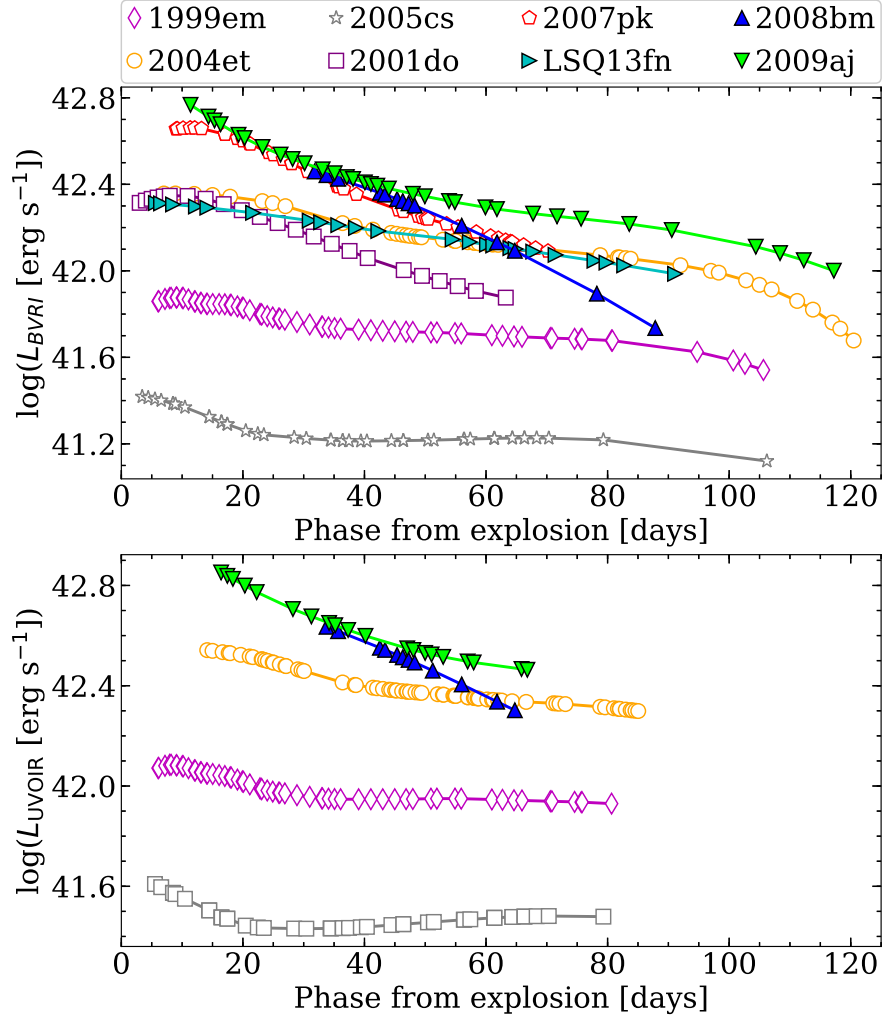


Figure 4.3: $BVRI$ (top) and $UVOIR$ (bottom) pseudo-bolometric light curves of the LLEV SNe II in our set (filled symbols) and a selection of normal SNe II that share some of the properties seen on LLEV SNe II (empty symbols).

sample, except SN 1983K for which the photometry in the necessary bands is not available. For comparison, we also report a selection of normal SNe II from the literature that share some of the properties observed in our LLEV SN II sample: SN 2001do (Faran et al. 2014a), which has a decline rate similar to SN 2008bm and SN 2009au; SN 1999em (Hamuy et al. 2001; Leonard et al. 2002; Elmhamdi et al. 2003), which has a decline rate similar to SN 2009aj and LSQ13fn; SN 2004et (Sahu et al. 2006; Misra et al. 2007; Maguire et al. 2010a) which is one of the most luminous normal SN II; SN 2007pk (Inserra et al. 2013; Hicken et al. 2017), which shows signs of early ejecta-CSM interaction (see Section 4.5.1); and SN 2005cs (Pastorello et al. 2006; Pastorello et al. 2009), which has low expansion velocities (see Section 4.5.3). We see that SN 2008bm and SN 2009aj have luminosities higher than SNe II with a similar decline rate, confirming the result obtained in Fig. 4.2, and comparable to those of the early interacting SN 2007pk at epochs earlier than 40 d since explosion. After that, the luminosity of SN 2008bm decreases linearly, while the evolution of the SN 2009aj luminosity is similar to that of SN 2004et. LSQ13fn, as reported by Polshaw et al. (2016), has a luminosity similar to SN 2004et. We also compute the pseudo-bolometric light curve using ultraviolet, optical, and near-IR (UVOIR) photometry, from u/U - up to H -band (the bottom part of Fig. 4.3). The latter suggests that SN 2008bm and SN 2009aj are not only brighter in the optical (top part of Fig. 4.3) but also in all the wavelength range between ultraviolet and near-IR.

4.4.3 Colour evolution

Normal SNe II are found to form a continuum population in observed colours, showing a large diversity at all epochs. While there are some (red) normal SNe II that clearly show the effects of strong host galaxy reddening, most of the colour dispersion has been concluded to arise from intrinsic colour differences between normal SNe II (de Jaeger et al. 2018, hereafter D18).

The top part of Fig. 4.4 shows the $B-V$ colour curves of the normal SNe II analysed in D18² (empty circles) and corrected for E_{B-V}^{host} (using values of A14), along with the LLEV SNe II in our set. We note that the LLEV SNe II are systematically bluer than normal SNe II in all the phase range reported in the plot. The latter could be due to low metallicity progenitors (where the lower the progenitor metallicity, the bluer the color; Dessart et al. 2014), or a flux contribution due to an ejecta-CSM

²We remove SN 2009au from the D18 sample since it is in our LLEV SN II sample.

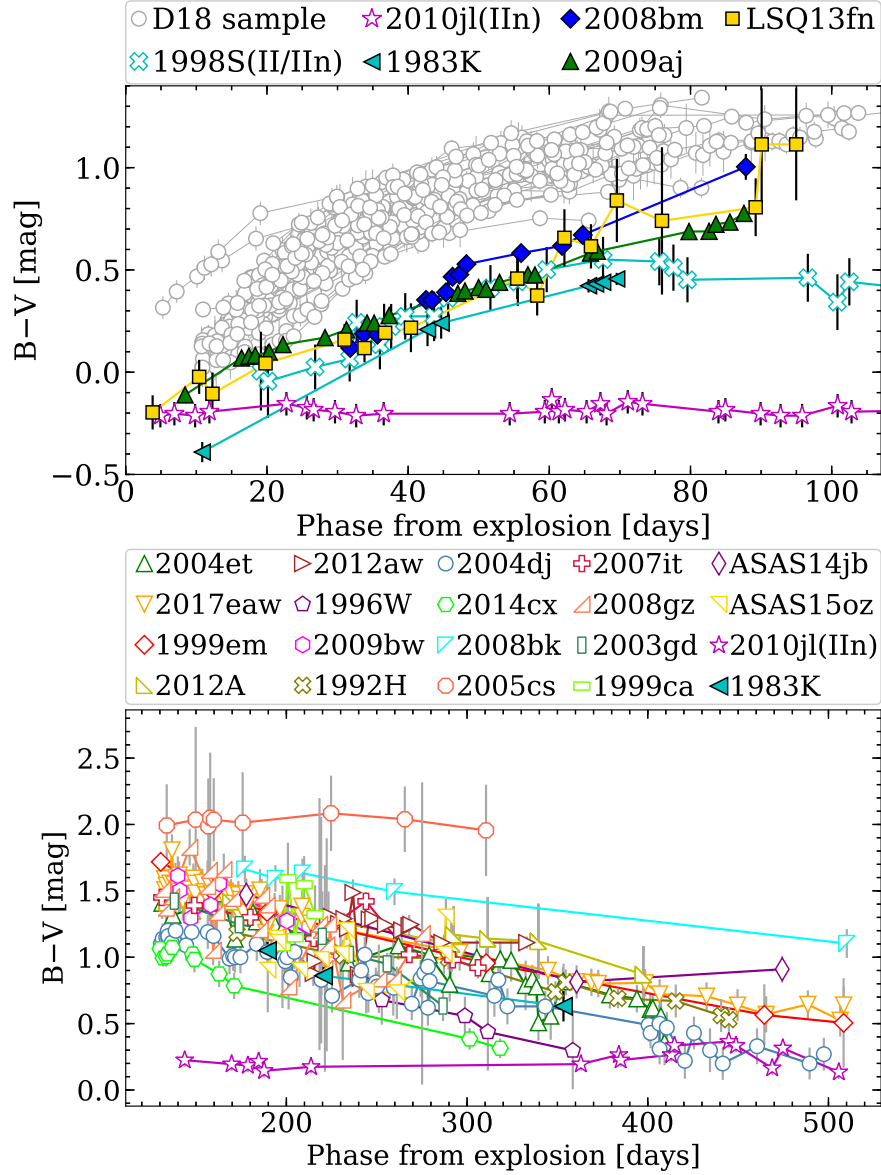


Figure 4.4: Top: evolution of the $B-V$ colour, corrected for E_{B-V}^{host} , during the first ~ 100 d of the LLEV SNe II in our set (filled symbols) compared with the normal SNe II in the D18 sample (empty circles). Bottom: evolution of the $B-V$ colour, corrected for E_{B-V}^{host} , during the radioactive tail of SN 1983K (filled triangle) and of normal SNe II from the literature with B - and V -band photometry during 190–350 d since explosion. We also include SN II/IIn 1998S (top, cyan crosses) and SN IIn 2010jl (top and bottom, magenta stars) to depict the effect of a long lasting ejecta-CSM interaction over the $B-V$ colour.

interaction, which makes colors bluer than normal SNe II as in the case of SN II/IIIn 1998S (Fassia et al. 2001) and SN IIIn 2010jl (Fransson et al. 2014), which are included in Fig. 4.4 for comparison.

The bottom part of Fig. 4.4 shows the $B-V$ colour evolution during the radioactive tail of SN 1983K, compared with normal SNe II that we found in the literature with B - and V -band photometry during 190–350 d since explosion (i.e., the phase range covered by SN 1983K during the radioactive tail). We see that the $B-V$ colour evolution of SN 1983K is consistent with the rest of normal SNe II in the plot and quite different to the SN IIIn 2010jl. The latter suggests that for SN 1983K, the flux during the radioactive tail is dominated by the $^{56}\text{Co} \rightarrow ^{56}\text{Fe}$ decay.

4.4.4 Nickel mass

As was shown by Hamuy (2003), the mass of nickel synthesized during the SN II explosion correlates with the absolute V -band magnitude at 50 d since explosion ($M_V^{50\text{d}}$). The latter correlation is because both quantities depend, among other parameters, on the explosion energy. Therefore, with this correlation we can roughly estimate the expected $M_V^{50\text{d}}$ value for an SN II, not contaminated for extra source of photons (e.g., photons from an ejecta-CSM interaction), measuring its nickel mass.

Assuming that the observed flux during the radioactive tail is due to the $^{56}\text{Co} \rightarrow ^{56}\text{Fe}$ decay, and that all the γ -rays from that decay are fully thermalized, the nickel mass can be estimated with

$$M_{\text{Ni}} = 7.866 \times 10^{-44} L_t \exp \left[\frac{(t - t_0)/(1 + z) - 6.1 \text{ d}}{111.26 \text{ d}} \right] M_{\odot} \quad (4.1)$$

(Hamuy 2003), where L_t is the bolometric luminosity (in erg s^{-1}) measured at epoch t (in d), and t_0 and z are the explosion epoch and heliocentric redshift of the SN, respectively.

To estimate L_t for the LLEV SNe II in our set, we use

$$\log L_t = [-(V_{0,t} + \text{BC}) + 5 \log D - 8.14]/2.5, \quad (4.2)$$

(Hamuy 2003), where $V_{0,t}$ is the V -band magnitude at epoch t during the radioactive tail corrected by extinction, D is the SN distance (in cm), and BC is the bolometric correction. For the latter, we assume the same BC for SNe II ($\text{BC} = 0.26 \pm 0.06 \text{ mag}$; Hamuy 2001). For SN 2009aj we convert Rri to V -band photometry using nebular spectra of normal SNe II, nearly at the same epoch

of the photometry. Finally, we compute nickel masses using equation 4.1 and assuming full γ -ray trapping. This assumption for the LLEV SNe II is partially supported by the fact that for SN 1983K we measure a V -band radioactive tail slope of $1.01 \pm 0.02 \text{ mag (100 d)}^{-1}$, which is consistent with the slope of $0.98 \text{ mag (100 d)}^{-1}$ expected for the full γ -ray trapping scenario.

Fig. 4.5 show the location of the LLEV SNe II (blue squares) in the nickel mass versus $M_V^{50\text{d}}$ space. In order to compare these SNe with the distribution given by the A14 sample (empty circles), we fit a power law (solid line), where the dashed lines indicate the $\pm 3\sigma$ limits. We see that all LLEV SNe II in the plot are outliers, i.e., at 50 d since explosion they are brighter than those explosions producing the same amount of nickel. The latter, along with the color evolution for LLEV SNe II (Fig 4.4), indicates that for these objects there is a source of photons, still relevant at 50 d since explosion, which becomes negligible at the radioactive tail. We speculate that the source of these photons is the early interaction between the SN ejecta and the CSM.

4.5 SPECTROSCOPIC PROPERTIES

In the previous section, we found evidence in favour of an early ejecta-CSM interaction scenario for LLEV SNe II. In this section, analysing the spectroscopic data, we present further evidence that reinforces this scenario.

4.5.1 Early ejecta-CSM interaction

The top half of Fig. 4.6 shows the earliest spectra of SN 1983K, SN 2009aj, SN 2009au, and LSQ13fn (left), along with zooms around $H\delta$, $H\gamma$ and $H\beta$ (middle) and $H\alpha$ (right). We can see that all of them show $H\alpha$ and $H\beta$ in emission with no prominent absorption features, which is characteristic of an SN II ejecta interacting with a CSM. The spectral feature located between $H\gamma$ and $H\beta$ (prominent in SN 1983K and LSQ13fn, but weaker in SN 2009aj and SN 2009au spectra) corresponds to He II $\lambda 4686$ possibly blended with N III $\lambda 4640$ (Niemela et al. 1985) and C III $\lambda 4648$ (Polshaw et al. 2016). The high temperature needed to produce the N III/C III/He II feature could come from the conversion of kinetic energy into thermal energy during an ejecta-CSM interaction,

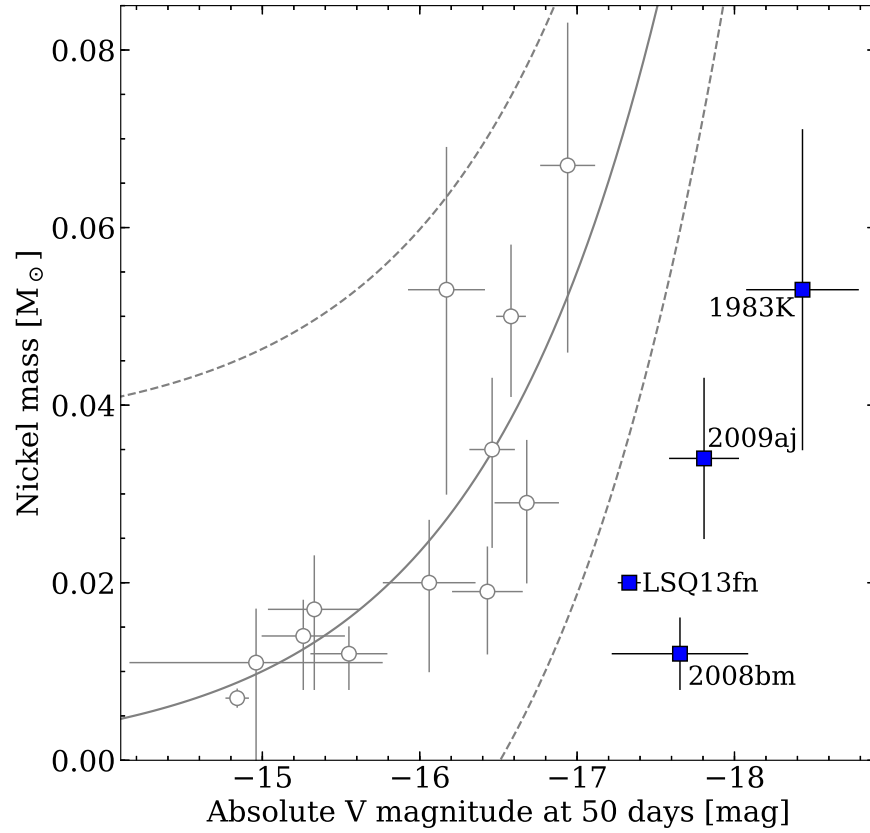


Figure 4.5: Nickel mass versus absolute V -band magnitude at 50 d since explosion, showing the SNe II in the A14 sample (empty circles) and the LLEV SNe II in our set (blue squares). The solid line corresponds to a power law fit, where dashed lines indicate the 3σ error around the fit.

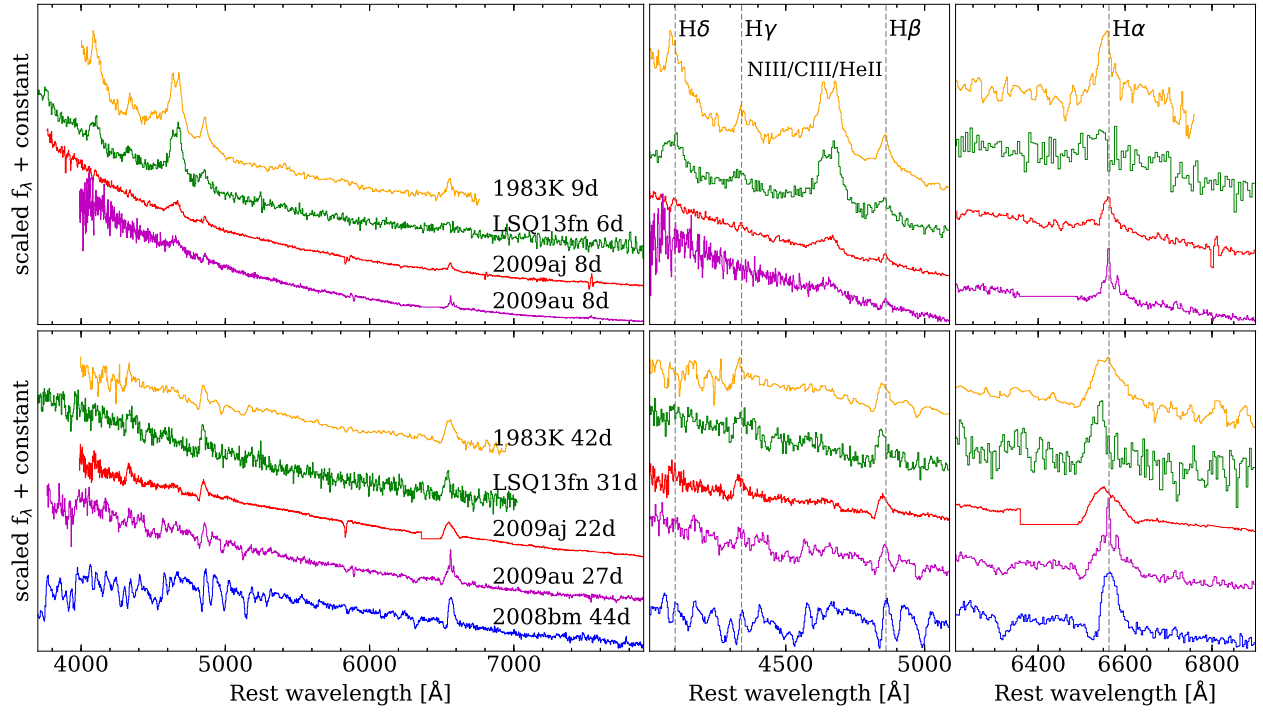


Figure 4.6: Earliest spectra showing emission lines (top left) along with the first spectra showing Balmer absorptions (bottom left) for our LLEV SN II sample, and zooms around H δ , H γ , and H β (middle panels) and H α (right panels). Epochs on left panels are since the explosion. Spectra were corrected for redshift and colour excess.

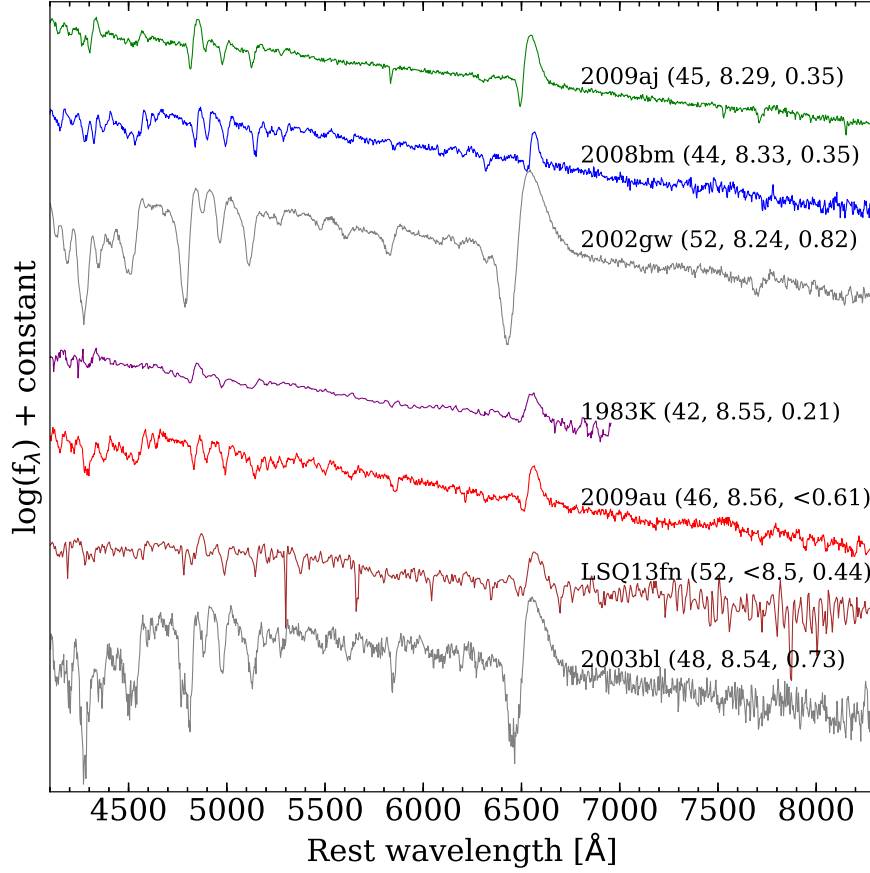


Figure 4.7: Spectra at around 50 d since explosion of the LLEV SNe II in our set. We also include spectra of SN 2002gw and SN 2003bl (gray lines), which have H II region oxygen abundances similar to the LLEV SNe II in our set. Spectra were corrected for redshift and reddening. Values in parenthesis are the epoch since the explosion, the oxygen abundance, and the $B-V$ colour, respectively.

which favours this scenario.

In the bottom half of Fig. 4.6 we can see that for SN 1983K, SN 2009aj, SN 2009au, and LSQ13fn there is no evidence of an ejecta-CSM interaction in spectra at 42, 22, 27, and 31 d since explosion, respectively. The latter indicates that the early epochs interaction lasts up to 3–6 weeks since explosion. The spectrum of SN 2008bm at 44 d since explosion does not show evidence of an ejecta-CSM interaction, which is consistent with the estimation we obtained for its duration from the other LLEV SNe II.

4.5.2 Weakness of metal lines

Polshaw et al. (2016) reported the weakness of metal lines in the spectra of LSQ13fn compared to normal SNe II. In that work, one of the parameters that they suggested to explain the weakness of metal lines is a low metallicity of the SN progenitor. In fact, Dessart et al. (2014) explored theoretically the dependence on the SN II progenitor metallicity of some spectral features. The general behaviour they obtained is: the lower the progenitor metallicity, the weaker the metal lines. A lower metallicity also implies a lower line blanketing and therefore a color bluer than other SNe II with a higher metallicity, which in principle could explain the blue colour we observe in LLEV SNe II.

Anderson et al. (2016) reported the oxygen abundance ($12 + \log(\text{O}/\text{H})$) of the H II regions coincident or near to the site of explosion of 119 SNe II (among them were: SN 2008bm, SN 2009aj, and SN 2009au), which is used as a proxy for the metallicity of their progenitors. Values for the LLEV SNe II in our set, using the N2 calibration of Marino et al. (2013), are listed in Table 4.1. SN 2008bm and SN 2009aj are among the 10 per cent of SNe II with the lowest oxygen abundances (≤ 8.33 dex) in the Anderson et al. (2016) sample (which has an average value of 8.49 dex). Therefore, for those SNe the progenitor metallicity could contribute to the observed weakness of metal lines in their spectra.

Fig. 4.7 shows the spectra of SN 1983K, SN 2008bm, SN 2009aj, SN 2009au, and LSQ13fn at around 50 d since explosion. In Fig. 4.7 we also include the spectra (at around 50 d since explosion) of SN 2002gw and SN 2003bl (G17), which have an H II region oxygen abundances similar to SN 2008bm and SN 2009aj, and SN 1983K and SN 2009au, respectively. Similar to the spectrum of LSQ13fn, the spectra of SN 1983K, SN 2008bm, SN 2009aj, and SN 2009au show weak metal lines in the range between 5300 and 6400 Å compared to the spectra of SN 2002gw and SN 2003bl. We therefore conclude that progenitor metallicity is not likely to be the dominant parameter producing the weakness of metal lines in these LLEV SNe II.

The strength of metal lines not only depends on the progenitor metallicity, but also on the temperature of the line formation region and, when the SN is surrounded by a CSM, on the contribution to the flux generated from the ejecta-CSM interaction (Leloudas et al. 2015). Regarding the temperature,

Anderson et al. (2016) show that the pEW of the Fe II λ 5018 line in normal SNe II spectra increases with the $V-I$ and $V-i$ colour, which are used as a proxy for temperature. The LLEV SNe II spectra in Fig. 4.7, with $B-V$ colour values of 0.21–0.35 mag, are bluer than the spectra of SN 2002gw and SN 2003bl (with $B-V = 0.82$ and 0.73 mag, respectively). This indicates that the weakness of metal lines seen in the LLEV SNe II spectra could be due to the high temperatures at the line formation region, which modifies the opacity.

To explore the effect on the pEW due to the contribution of the ejecta-CSM interaction, in Fig. 4.8 we plot the Fe II λ 5018 line pEW at 50 d since explosion, as a function of the oxygen abundance and the $B-V$ colour (corrected for E_{B-V}^{host}) at 50 d since explosion. Due to line dilution we expect that LLEV SNe II will move away from the normal SNe II which not show such interaction with the CSM. As visible in the plot, LLEV SNe II (blue squares) indeed seem to form a separated set of objects from the rest of SNe II (gray circles). With the aim to confirm this visual finding, we run the mean-shift algorithm to search for clusters in this space. We perform simulations where points are moved within their errors (assuming a normal distribution), and we find that in 56 per cent of the realizations the LLEV SNe II form a separated group with respect to the rest of SNe II. Although, given the low number of LLEV SNe II, this result has to be taken with caution, the fact that these SNe 56 per cent of the time cluster in a different parameter space region, could indicate that the higher temperature and the line dilution induced by the ejecta-CSM interaction are the dominant factors to reduce the strength of metal lines.

To quantify the effect of line dilution to first order, we select SN 2008M (A14, G17) because it is one of the bluest normal SNe II in the D18 sample. With this, we can isolate as best as possible the effect of CSM dilution on the pEW of the metal lines from the similar effect of temperature we have analysed previously. Fig. 4.9 shows the spectrum of SN 2009aj at 39 d since explosion (red line) and a spectrum of SN 2008M nearly at the same epoch and scaled to the SN 2009aj distance (gray line). Spectra of SN 2009aj and SN 2008M have Fe II λ 5018 pEW of 7.1 and 9.7 Å, respectively. In order to include the contribution of a CSM to the flux of SN 2008M, we model the CSM as a blackbody. Using a radius of 10^{15} cm and a temperature of 7200 K, the continuum of SN 2008M plus the CSM (blue line) fits to the continuum of SN 2009aj. The Fe II λ 5018 pEW of the composite spectrum is of 5.7 Å, which matches better to the value for SN 2009aj. Therefore, even when the SN 2008M

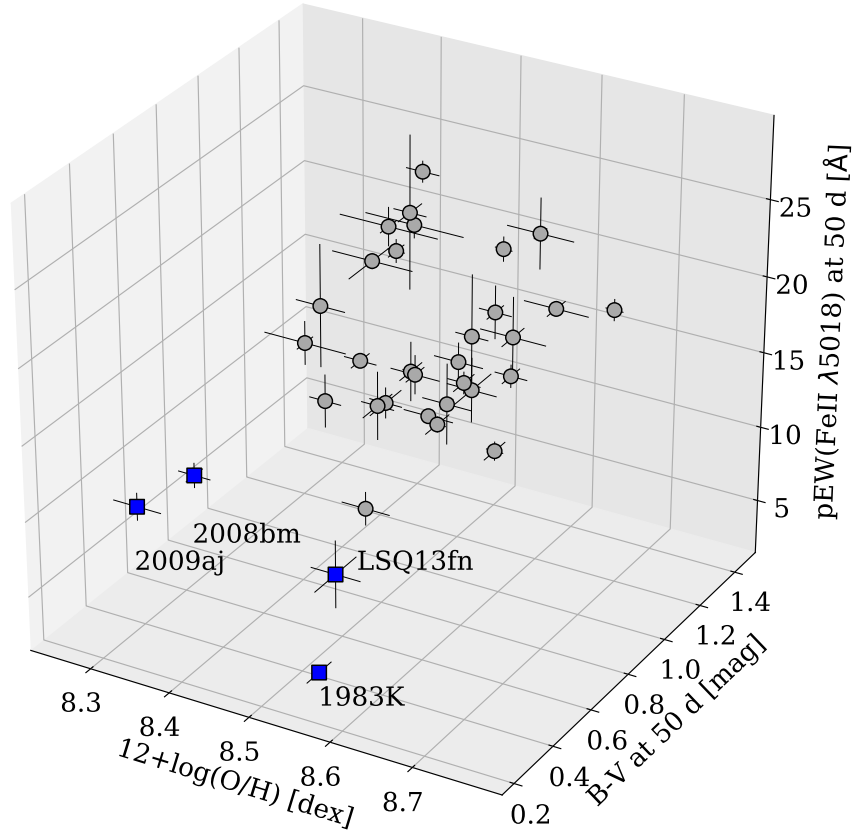


Figure 4.8: pEW of the Fe II $\lambda 5018$ line at 50 d since explosion, as a function of the oxygen abundance and the $B-V$ colour (corrected for redshift and reddening) at 50 d since explosion, for the LLEV SNe II in our set (blue squares) and the normal SNe II in the A14 sample (circles).

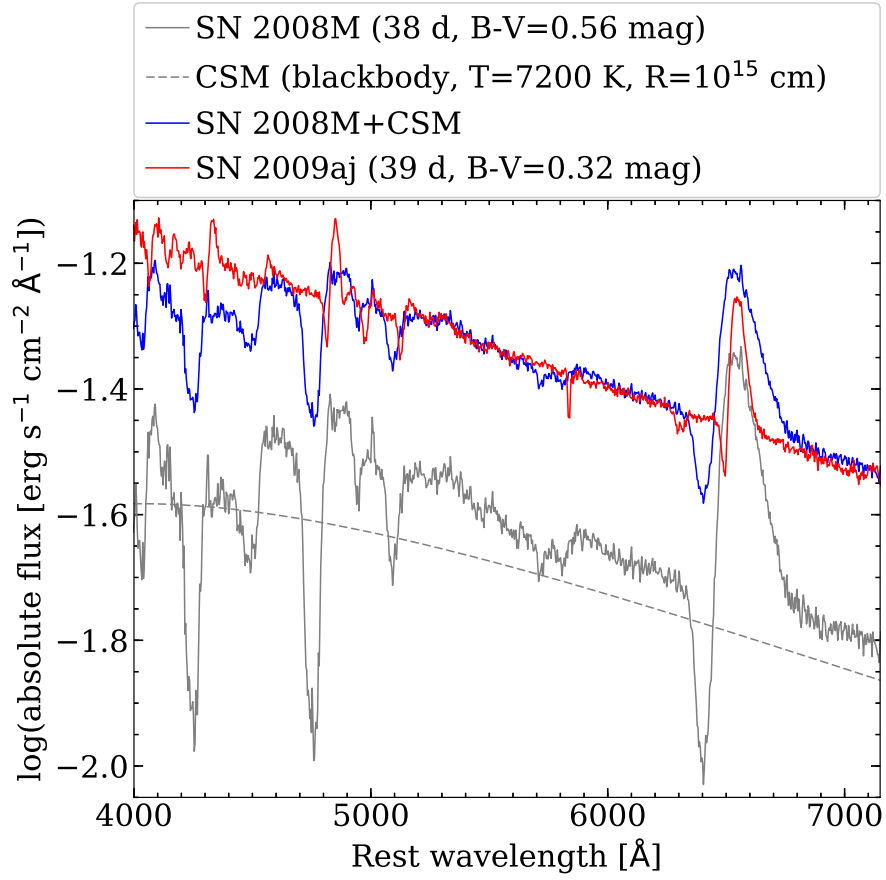


Figure 4.9: Comparison of the spectrum of SN 2009aj at 39 d since explosion (red line) with a composite spectrum (blue line), which is the sum of the SN 2008M spectrum at 38 d since explosion (gray line) and a blackbody continuum (dashed line).

spectrum is not as blue as the spectrum of SN 2009aj, and the oxygen abundance at the site of SN 2008M (8.43 dex; Anderson et al. 2016) is higher than the value for SN 2009aj, the flux contribution due to the ejecta-CSM interaction seems to be the more efficient driver of the observed weakness of metal lines in its spectra.

4.5.3 Expansion velocities

Fig. 4.10 shows the evolution of the expansion velocities, measured through the Fe II $\lambda 5169$ minimum absorption lines (v_{FeII}), of the LLEV SNe II in our set (coloured symbols) and the normal SNe II in the G17 sample³ (empty circles). Expansion velocities for LLEV SNe II are below the 1σ limit (dotted line) of the G17 sample (2820 km s^{-1} at 50 d since explosion). In particular, SN 1983K and LSQ13fn have expansion velocities similar to SN 2009aj (which has $v_{\text{FeII}} \approx 2340 \text{ km s}^{-1}$ at 50 d since explosion), SN 2009au has expansion velocities quite similar to SN 1999br (orange dashed line), which is one of the SNe II with the lowest expansion velocities in the G17 sample (1550 km s^{-1} at 50 d since explosion), while SN 2008bm has expansion velocities even lower (1280 km s^{-1} at 50 d since explosion). These low expansion velocities can be explained by the loss of kinetic energy by the ejecta due to their interaction with CSM.

4.6 DISCUSSION

4.6.1 A break in the magnitude-velocity relation

As we have seen in Section 4.4.1 and 4.5.3, LLEV SNe II are characterized by having luminous peak magnitudes and low expansion velocities. This is not expected in a scenario where more energetic SN II explosions that produce high luminosities also have high expansion velocities. This trend is shown in Fig. 4.11, where we plot the *V*-band absolute magnitude and the expansion velocity, both at 50 d post explosion, for the A14 SN sample (gray circles). To characterize the distribution of the A14 sample in this space, we perform a Gaussian process fit (solid line), where dashed lines indicate

³The original G17 sample includes SN 2008bm, SN 2009aj, and SN 2009au, which we remove since they are in our LLEV SN II sample.

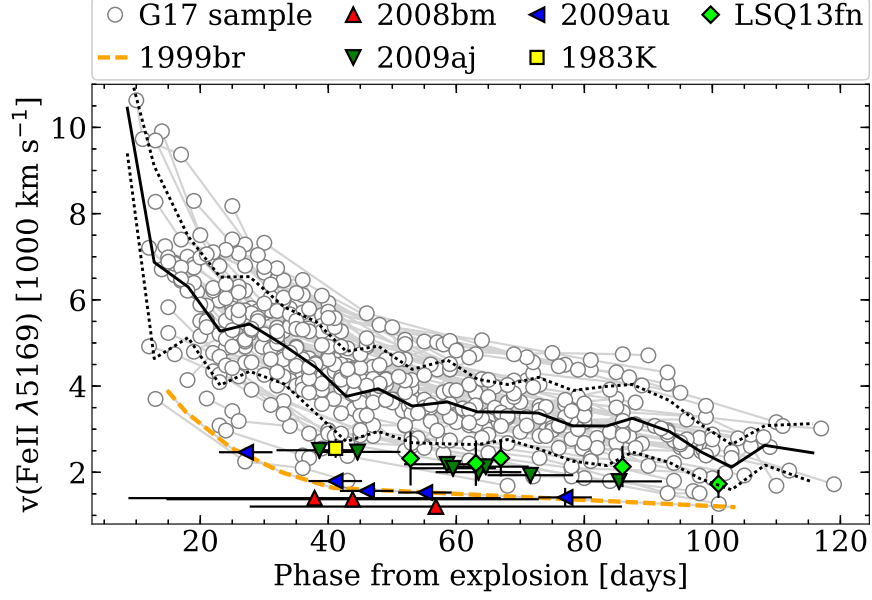


Figure 4.10: Evolution of the expansion velocities, measured through the Fe II $\lambda 5169$ minimum absorption lines, of the LLEV SNe II in our set (filled symbols) and the normal SNe II in the G17 sample (empty circles). Black solid and dotted lines correspond to the mean values and standard deviations, respectively, of the expansion velocities in the G17 sample. Orange dashed line correspond to the expansion velocities for SN 1999br.

the $\pm 3\sigma$ error around the fit. We can see that the LLEV SNe II (blue squares) populate a region where the only known member was LSQ13fn, marking a discrepancy of 2–3 mag with respect to the trend obtained with the A14 sample. At this point, it is not clear whether the LLEV SNe II can be considered as a new sub-type of SN II, or whether they are part of a continuum in the SN II distribution induced by an increasing ejecta-CSM interaction.

To test the latter, we include in Fig. 4.11 all SNe II with evidence of early ejecta-CSM interaction that we found in the literature (and with available spectroscopy or expansion velocities): SN 1979C (Branch et al. 1981; de Vaucouleurs et al. 1981), SN 1980K (Buta 1982), SN 1998S (Fassia et al. 2000; Fassia et al. 2001), SN 2001fa (Faran et al. 2014a; Hicken et al. 2017), SN 2007pk (Inserra et al. 2013; Hicken et al. 2017), SN 2008fq (Taddia et al. 2013; Faran et al. 2014a), SN 2009bw (Inserra et al. 2012), SN 2013fs (Yaron et al. 2017; Bullivant et al. 2018), SN 2014G (Bose et al. 2016; Terreran et al. 2016), and ASASSN-15oz (Bostroem et al. 2019). These SNe II, as we can see in Fig. 4.11, are brighter than the trend obtained with the A14 sample, with SN 1980K, SN 1998S, SN 2007pk, and SN 2008fq being brighter than the 3σ limit. However, they do not fill the

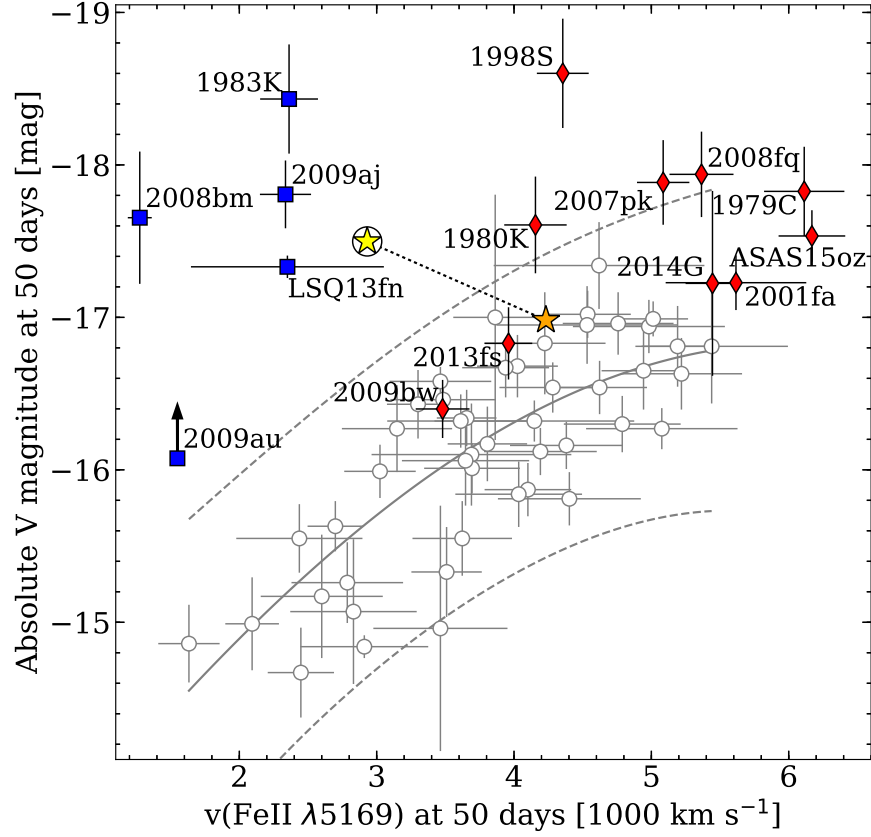


Figure 4.11: Absolute V -band magnitude versus expansion velocity, both at 50 d since explosion, showing the LLEV SN II set (blue squares), the normal SNe II in the A14 sample (empty circles), and some luminous SNe II with evidence of ejecta-CSM interaction from the literature (red diamonds). The solid line corresponds to the Gaussian process fit, while dashed lines indicate the 3σ error around the fit. We also plot the location of our SN II model (see Section 4.6.2) without (orange star) and with (circled yellow star) CSM.

gap between the distribution of SNe II and the LLEV SNe II. This suggests that the LLEV SNe II could indeed be a new sub-type of SNe II.

4.6.2 Interaction of the ejecta with a massive CSM

As mentioned in the previous paragraphs, a scenario where the SN II ejecta interacts with a CSM medium could explain all the characteristics observed in our SN set. In fact, during the ejecta-CSM interaction, part of the kinetic energy is converted into thermal energy and photons, which slows down the ejecta, increases the temperature and luminosity, and veils the spectral lines.

In order to test whether the ejecta-CSM interaction is responsible of converting a normal SN II into a LLEV SN II, we perform hydrodynamical simulations. We focus on the modelling of SN 2009aj here because its explosion epoch and host galaxy colour excess are better constrained than those for SN 2008bm and SN 2009au. We adopt the same numerical method as in Moriya et al. (2017) and Moriya et al. (2018) and use the radiation hydrodynamics code STELLA (Blinnikov et al. 1998; Blinnikov et al. 2000; Blinnikov et al. 2006) for our numerical light curve modelling.

We take the $14 M_{\odot}$ progenitor model in Moriya et al. (2018) and attached a dense CSM above the progenitor by adopting the β law wind velocity. We take one model with the mass-loss rate of $3 \times 10^{-2} M_{\odot} \text{ yr}^{-1}$, the terminal wind velocity of 10 km s^{-1} , $\beta = 5$, and the dense CSM radius of 10^{15} cm . This dense CSM has a mass of $3.6 M_{\odot}$. When we explode the progenitor in this system with the explosion energy of $8 \times 10^{50} \text{ erg}$, we obtain the *UBVRI* absolute light curves and expansion velocities as in Fig. 4.12. We can see that the observed absolute magnitudes and expansion velocities of SN 2009aj (empty symbols) match well to the numerical results (solid lines for the model with CSM and dashed lines for those without CSM).

The effect on the luminosity-velocity relation produced by the interaction of the ejecta with a massive CSM is depicted in Fig. 4.11. We can see that the SN II model without CSM (orange star), consistent with the rest of the observed SNe II, is translated outside of the 3σ limit in direction to the location of the LLEV SNe II if we include a massive CSM (circled yellow star).

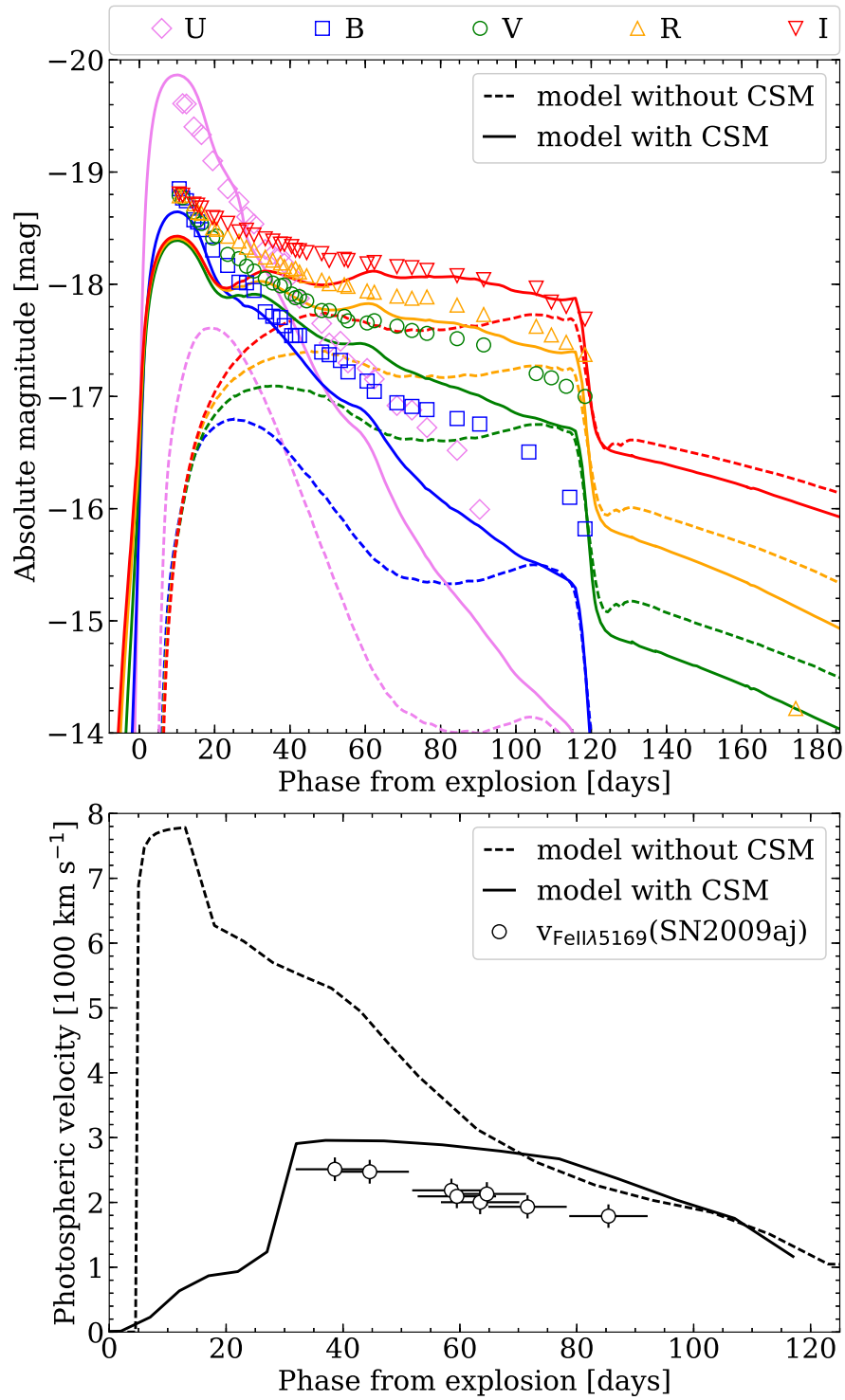


Figure 4.12: Absolute *UBVRI* light curves (top) and expansion velocities (bottom) of our model with CSM (solid lines) and of SN 2009aj (empty symbols). The same model but without CSM (dashed lines) is displayed for comparison.

4.6.3 The observed fraction of LLEV SNe II

In order to estimate a first approximation of the fraction of LLEV within the normal SN II family, we use the monitoring campaign carried out by the CHASE survey. Since LLEV SNe II are typically more luminous than normal SNe II, and given that the CHASE is a magnitude-limit survey, the estimation of the fraction of LLEV SNe II we will provide should be regarded as an upper limit.

During March 2008–December 2014, CHASE reported the discovery of 46 normal SNe II and 3 SNe IIn. In addition, we include 58 normal SNe II and 6 SNe IIn discovered by other surveys during the same period, which were discovered by CHASE independently. In order to identify possible LLEV SNe II in the CHASE normal SN II sample, we check the classification reports (and classification spectra, if they are available). We select as possible LLEV SNe II those SNe whose classification spectra best match to a subluminal SN II (e.g., SN 2005cs), or have low expansion velocities (e.g., $H_\alpha \lesssim 5000 \text{ km s}^{-1}$). From this list, we discard those SNe having absolute magnitude⁴ (at the moment of the discovery or in posterior confirmation epochs) consistent with subluminal SNe II ($\gtrsim -16.0 \text{ mag}$; Lisakov et al. 2018), and those having spectra earlier than 3 weeks since explosion but not showing signs of ejecta-CSM interaction. From the CHASE SN IIn sample we select as possible LLEV SN II those SNe IIn that spectroscopically do not evolve as an SN IIn but as a normal SN II with narrow P-Cygni profiles (as in the case of SN 2008bm, SN 2009au, and LSQ13fn). For this, we use the information available on the literature.

Among the 104 normal SNe II, 15 show spectral characteristics consistent with low expansion velocities, of which 7 are published subluminal SNe II, 2 have reports based on spectra earlier than 3 weeks since explosion, but not showing signs of ejecta-CSM interaction, and 3 have absolute magnitudes (corrected for E_{B-V}^{host} inferred from Na ID at the redshift of the host galaxy) $> -15.5 \text{ mag}$. Only SN 2009aj (which we study in this work) shows narrow P-Cygni profiles and high luminosities, while for SN 2008ch we do not have enough information to confirm or discard it. Among the 9 SNe IIn, 6 of them evolve as SNe IIn (with published spectroscopy). Only SN 2009au shows a posterior evolution different than an SN IIn, while for SN 2008gm and SN 2011fh there is not enough information to confirm or discard them. If we consider SN 2009aj and SN 2009au as the

⁴Discovery and confirmation magnitudes reported by CHASE are obtained from unfiltered images, which are similar to R -band magnitudes.

only LLEV SNe II in the CHASE sample, then its fraction could be as high as 1.9 per cent. On the other hand, if we consider all the unconfirmed candidates (SN 2008ch, SN 2008gm, and SN 2011fh) as LLEV SNe II, then the upper limit increases to 4.7 per cent. Therefore, the fraction of LLEV SNe II in the CHASE SN II sample could be as high as 1.9–4.7 per cent. The low fraction of LLEV SNe II points toward an uncommon progenitor. The latter should have a high mass loss rate close in time to core collapse in order to generate a sufficiently massive shell ($\sim 4 M_{\odot}$) close to the progenitor to produce the LLEV SNe II we observe.

4.6.4 Impact on SNe II as distance indicators

Since the LLEV SNe II do not follow the luminosity-velocity relation observed for normal SNe II, we have to analyse their impact over the use of normal SNe II as distance indicators.

As mentioned in Rodríguez et al. (2019), the SN II distance precision using the Photospheric Magnitude Method (Rodríguez et al. 2014) could be up to 0.26 mag within a 99 per cent of confidence level. In this case, the location of the LLEV SNe II (≥ 2 mag brighter than the expected from their expansion velocities) in the Hubble diagram (HD) will be $\geq 7.7\sigma$ below the Hubble law fit. Therefore easy to discard with an a sufficient amount of data. If we include the LLEV SNe II to compute the Hubble law fit, and considering a fraction of 4.7 per cent, the scatter in the HD increases to 0.50 mag, so even in this case the LLEV SNe II will be $\geq 4.0\sigma$ below the Hubble law fit. Therefore, in a HD, the LLEV SNe II can be easily detected and treated as outliers.

Since the oxygen abundance of LLEV SNe II is not necessarily low, we do not have evidence that those SNe are related to low metallicity galaxies, so we do not expect that the fraction of LLEV SNe II will increase with redshift (e.g., $z > 0.5$) as consequence of the evolution of the metallicity of the Universe. However, we expect to find a higher fraction of LLEV SNe II due to the Malmquist bias. For example, for the Large Synoptic Survey Telescope (LSST) the r -band 5σ limiting magnitude is estimated to be ~ 24.3 mag, so for $z \geq 0.5$ we expected to detect SNe II with $M_r \lesssim -18.0$ mag. In this case, the observed fraction of LLEV SNe II could be as high as 10–22 per cent, so the LLEV SNe II will be only ≥ 2.7 – 3.8σ below the Hubble law, which makes it difficult to recognize them as outliers. This means that the existence of LLEV SNe II have to be taken into

account if normal SNe II at high redshifts are used to derive cosmological parameters. Nevertheless, as we shown in this work, the current sample have expansion velocities which are in the lower end of the normal SN II distribution, therefore a cut on expansion velocities could greatly reduce their contamination.

4.7 CONCLUSIONS

In this work we presented optical and near-IR photometry of SN 2008bm, SN 2009aj, and SN 2009au. From the analysis of these data together with already published spectroscopy we found that they show similar characteristics than those of SN 1983K and LSQ13fn. In the luminosity-expansion velocity plane this possible family of SNe II, that we call LLEV, forms a separate group which have a V-band absolute magnitudes 2–3 mag brighter than those expected from their expansion velocities by the luminosity-velocity relation observed for normal SNe II.

The ejecta-CSM interaction observed in LLEV SNe II lasts up to 3–6 weeks since the explosion. Subsequently, spectra show P-Cygni profiles characterized by low expansion velocities, and a weakness of metal lines. We found evidence that the metal line weakness, especially in the region between 5300 and 6400 Å, seems not related to the metallicity of the progenitor but with a combined effect of the line dilution due to the contribution of the CSM to the flux, and the higher temperatures than normal SNe II at similar epochs. Through hydrodynamic simulations, which consider a RSG progenitor of $14 M_{\odot}$ with an explosion energy of 8×10^{50} erg, we found that the high luminosity and low expansion velocities seen on SN 2009aj can be explained if the ejecta interacts with a CSM of $\sim 3.6 M_{\odot}$ located very close to the progenitor.

Based on the discoveries by the CHASE survey, we obtained that the fraction of LLEV SNe II can be as high as 1.9–4.7 per cent. This low fraction, together with the high CSM mass we obtain from the hydrodynamic simulations, may indicate an uncommon progenitor with high mass loss rate close in time to core collapse in order to generate a sufficiently massive shell close to the progenitor. Based on the available data, it is unclear whether the LLEV SNe II are a new sub-type of SNe II or whether their location in the luminosity-velocity space (Fig. 4.11) depend on the properties of the CSM, which could form a continuum with the normal SNe II. It is necessary to populate the

luminosity-velocity space with more normal SNe II (and LLEV SNe II) in order to reveal the nature of these peculiar SNe II. Finally, we shown that, based on the current sample, LLEV SNe II should not represent a severe contaminant in the use of normal SNe II as standardizable candles.

Chapter 5

CONCLUSIONS

In this work I presented an in-depth analysis of the PMM to measure distances to SNe II. In particular, I tested whether there is an improvement on the PMM distance precision using near-IR instead of optical photometry. In the first part of this study I developed all the necessary tools to measure PMM distances. In order to test these tools, I applied the PMM to 24 SNe II. The main conclusions are the following.

- I computed analytical expressions in the *BVIJHK*-bands during the photospheric phase for the total-to-selective broad-band extinction ratios and *K*-corrections, through synthetic photometry obtained from a library of SN II spectra. I also developed routines to: 1) perform non-parametric light curve fits, and 2) compute explosion epochs using all optical spectra earlier than 40 d since the first detection.
- I revisited the C3 method to compute host galaxy colour excesses for SNe II presented in Rodríguez et al. (2014), now including *J*- and *H*-band photometry. I found that, among all possible colour-colour combinations with the *BVIJH* bands, the *V*–*I* versus *B*–*V* curve is the best combination to estimate $E_h(B-V)$, with an error of 0.1 mag.
- Using nine SNe II at $cz > 2000 \text{ km s}^{-1}$, I obtained HD rms values of 0.15–0.28 mag for *BVIJH* bands and, calibrating the PMM distances using four SNe II in galaxies with TRGB distances, I derived H_0 values ranging between 67.1 and 74.9 $\text{km s}^{-1} \text{ Mpc}^{-1}$.
- Adding six SNe II with host galaxy distances measured with TRGB, Cepheids, or SN Ia (total

15), which distances were converted to redshifts through the Hubble law, I obtained a HD rms of 0.15–0.26 mag in the optical bands, which reduces to 0.13 mag in the J -band. With this evidence, I set the PMM distance precision with the J -band below 10 per cent with a confidence level of 99 per cent.

In the second part of this work I presented new optical and near-IR data of 24 SNe II at $0.013 < z < 0.033$. I used this new data to compute distance moduli with the PMM. Combining this SN set with seven SNe II at $z > 0.013$ used in the first part of this work, I constructed $BVIJH$ HDs with 31 SNe II. The main results are the following.

- Correcting PMM distances for host galaxy colour excess using values measured with the C3 method, I obtained HD rms values of 0.22–0.40 mag for $BVIJ$ bands and of 0.21 mag for the H -band.
- Replacing host galaxy color excesses for a $V-I$ colour-term correction, the HD rms values for BVI bands are reduced to 0.24–0.26 mag, while for the J - and H -band the HD rms value is of 0.21 mag. The HD rms values for $BVIJH$ bands were not improved including linear-term corrections on s_2 and v_{ph} .
- The HD rms value that I obtained for the J - and H -band translates into a PMM distance precision of $9.7^{+2.6}_{-2.4}$ per cent (95 per cent CL).
- Using the H -band HD, I obtained $H_0 = 69.8 \pm 1.6(\text{stat}) \pm 2.8(\text{sys}) \text{ km s}^{-1} \text{ Mpc}^{-1}$. This value is consistent with the value of $71.17 \pm 1.66(\text{stat}) \pm 1.87(\text{sys}) \text{ km s}^{-1} \text{ Mpc}^{-1}$ reported by Jang and Lee (2017a), which used the same TRGB calibration of Jang and Lee (2017b) that we used in this work.

Finally, in the third part of this work I presented optical and near-IR photometry of SN 2008bm, SN 2009aj, and SN 2009au. From the analysis of these data together with already published spectroscopy I found that they show similar characteristics than those of SN 1983K and LSQ13fn. The main findings are the following.

- In the luminosity-expansion velocity plane this possible family of SNe II, that I call LLEV, forms a separate group which have a V -band absolute magnitudes 2–3 mag brighter than those expected from their expansion velocities by the luminosity-velocity relation observed for normal SNe II.

- The ejecta-CSM interaction observed in LLEV SNe II lasts up to 3–6 weeks since the explosion. Subsequently, spectra show P-Cygni profiles characterized by low expansion velocities, and a weakness of metal lines. I found evidence that the metal line weakness, especially in the region between 5300 and 6400 Å, seems not related to the metallicity of the progenitor but with a combined effect of the line dilution due to the contribution of the CSM to the flux, and the higher temperatures than normal SNe II at similar epochs.
- Through hydrodynamic simulations, which consider a RSG progenitor of $14 M_{\odot}$ with an explosion energy of 8×10^{50} erg, we found that the high luminosity and low expansion velocities seen on SN 2009aj can be explained if the ejecta interacts with a CSM of $\sim 3.6 M_{\odot}$ located very close to the progenitor.
- Based on the discoveries by the CHASE survey, I obtained that the fraction of LLEV SNe II can be as high as 1.9–4.7 per cent. This low fraction, together with the high CSM mass we obtain from the hydrodynamic simulations, may indicate an uncommon progenitor with high mass loss rate close in time to core collapse in order to generate a sufficiently massive shell close to the progenitor. Based on the available data, it is unclear whether the LLEV SNe II are a new sub-type of SNe II or whether their location in the luminosity-velocity space (Fig. 4.11) depend on the properties of the CSM, which could form a continuum with the normal SNe II. It is necessary to populate the luminosity-velocity space with more normal SNe II (and LLEV SNe II) in order to reveal the nature of these peculiar SNe II.
- I shown that, based on the current sample, LLEV SNe II should not represent a severe contaminant in the use of normal SNe II as distance indicators with the PMM.

APPENDIX

A MODEL SELECTION

For the model selection we consider two criteria: the “an information criterion” (AIC, Akaike 1974), which is based on information theory, and the Bayesian information criterion (BIC, Schwarz 1978), which is based on Bayesian inference. From a set of R models, the AIC selects the model that have the least information loss with respect to the unknown true model, while the BIC selects the model with the highest likelihood \mathcal{L} , given by

$$\mathcal{L}(\text{model}|\{X_i\}) = \prod_{i=1}^N p(X_i|\text{model}). \quad (5.1)$$

Here, X_i is the i -th observed data, $p(X_i|\text{model})$ is the probability density function (pdf) of X_i given the model, and N is the number of observed data points. Quantitatively, the AIC and BIC search for a balance between overfitting and underfitting penalizing the likelihood. For the AIC and the BIC, the best model is one which minimizes the quantity

$$\text{AIC} \equiv -2 \ln \mathcal{L}_{\max} + 2Nk/(N - k - 1) \quad (5.2)$$

(corrected for small sample sizes, Sugiura 1978), and

$$\text{BIC} \equiv -2 \ln \mathcal{L}_{\max} + k \ln N \quad (5.3)$$

(Schwarz 1978), respectively, where \mathcal{L}_{\max} is the maximum likelihood achievable by the model, and k is the number of parameters of the model.

It is known that a model selection based only on the minimum AIC value reached for a certain model does not provide enough evidence to prefer that model over the other ones (e.g., Akaike 1978;

Burnham and Anderson 2002). Instead, it is necessary to include into the analysis the strength of evidence in favour of each model. To quantify the latter, it has been proposed to use the likelihood of the model given the data (e.g., Akaike 1978) which, normalized by the sum of likelihoods of all R models, defines the Akaike weights

$$w_i = \frac{e^{-0.5(\text{AIC}_i - \text{AIC}_{\min})}}{\sum_{r=1}^R e^{-0.5(\text{AIC}_r - \text{AIC}_{\min})}} \quad (5.4)$$

(e.g., Burnham and Anderson 2002). Here, AIC_{\min} is the minimum AIC value reached among the R models used in the analysis. The same idea is applicable for the BIC (Burnham and Anderson 2002), which defines the Bayesian weights

$$P_i = \frac{e^{-0.5(\text{BIC}_i - \text{BIC}_{\min})}}{\sum_{r=1}^R e^{-0.5(\text{BIC}_r - \text{BIC}_{\min})}}. \quad (5.5)$$

For the AIC and BIC, the evidence ratios defined as w_i/w_j and p_i/p_j , respectively, allow comparison of the evidence in favour of the i -th model as the best model versus the j -th model. As reference, if evidence ratios are greater than 13.0, then there is a strong evidence in favour of the i -th model over the j -th model (e.g., Liddle 2007). If several models have substantial support as the best (e.g., evidence ratios < 13.0), then, by the principle of parsimony, we select the one with less parameters.

In the case of least-square regressions, with random errors normally distributed and with constant variance,

$$-2 \ln \mathcal{L}_{\max} = N \ln 2\pi \hat{\sigma}^2 + N \quad (5.6)$$

(e.g., Burnham and Anderson 2002, p. 17), where $\hat{\sigma}^2$ is the average of squared residuals around the model. The AIC and BIC in this case can be expressed as

$$\text{AIC} = \ln \hat{\sigma}^2 + (N + k - 1)/(N - k - 1), \quad (5.7)$$

$$\text{BIC} = \ln \hat{\sigma}^2 + k/N \cdot \ln N. \quad (5.8)$$

Since $\hat{\sigma}^2$ is computed from data, it must be considered as a model parameter.

In the case of nonparametric regressions (NPR), like `loess`, k is not defined. Instead, it has been proposed to use the trace of the smoother matrix, $\text{tr}(H)$, which is a quantity analogous to the number of parameters in a parametric regression (Cleveland et al. 1992; Hurvich et al. 1998). Replacing

$k = \text{tr}(H) + 1$ in equation (5.7) allows us to obtain the AIC version for NPR presented by Hurvich et al. (1998).

To check the normality of random errors, it is necessary to carry out a normality test. As we do not measure random errors directly, we use residuals instead. However, widely used normality tests like the Shapiro and Wilk (1965) and the Jarque and Bera (1987) test, when applied over residuals, have little power to reject the null hypothesis even when the random errors are not normal (Das and Imon 2016). Imon (2003) proposed a statistic more suitable to verify normality for regressions, which is based on the Jarque and Bera (1987) test and on the use of unbiased moments. The statistic of the test, called Rescaled Moment (RM), is defined as

$$\text{RM} \equiv Nc^3 [\hat{\mu}_3^2 / \hat{\mu}_2^3 / 6 + c \cdot (\hat{\mu}_4 / \hat{\mu}_2^2 - 3)^2 / 24] \quad (5.9)$$

(Rana et al. 2009), where $\hat{\mu}_i$ is the i -th sample moment, and $c \equiv N / (N - k)$. Under the null hypothesis of a normal distribution, the RM statistic is asymptotically distributed as a chi-square distribution with two degrees of freedom.

B SN II SPECTRA LIBRARY

In order to compute total-to-selective broadband extinction ratios (Section 2.5 and 2.7) and K -corrections (Section 2.6) for SNe II, it is necessary to know their SED. The latter can be estimated through theoretical models (e.g., Sanders et al. 2015; de Jaeger et al. 2015; de Jaeger et al. 2017a) or, as in Olivares (2008) and in this work, through spectroscopic observations.

In practice, spectra are not always taken with the slit oriented along the parallactic angle (PA), so their shape can be modified due to differential refraction (Filippenko 1982). Even when the slit is oriented along the PA, contamination due to the light from the host galaxy can produce spurious SEDs. Therefore we have to check the flux calibration of spectra before using them as proxies for the SED. To do the latter, we compute colour indices from the spectra and then we compare them with those obtained using the observed photometry. If the spectrum is well flux-calibrated, then colour differences should be small.

Photometric colour indices at the epoch of the spectra can be computed through the light curve

fitting procedure presented in Section 2.4, while to compute a $x_1 - x_2$ colour from a spectrum we use

$$x_1 - x_2 = -2.5 \log \left(\frac{\int d\lambda S_{x_1, \lambda} F_\lambda \lambda}{\int d\lambda S_{x_2, \lambda} F_\lambda \lambda} \right) + \text{ZP}_{x_1 - x_2}. \quad (5.10)$$

Here, λ is the wavelength in the observer's frame, F_λ is the observed SED of the source, $S_{x_1, \lambda}$ and $S_{x_2, \lambda}$ are the transmission functions of the photometric band x_1 and x_2 , respectively, and $\text{ZP}_{x_1 - x_2}$ is the zero point of the colour scale, which can be computed using a star with good spectrophotometric observations.

We use the Vega SED published by Bohlin and Gilliland (2004)¹ and the magnitudes published by Fukugita et al. (1996): $B_{\text{Vega}} = 0.03$, $V_{\text{Vega}} = 0.03$, and $I_{\text{Vega}} = 0.024$ mag, and by Cohen et al. (1999): $J_{\text{Vega}} = -0.001$, $H_{\text{Vega}} = 0.000$, and $K_{\text{Vega}} = -0.001$ mag. We adopt the transmission functions given in Hamuy et al. (2001). For $B - V$, $V - I$, $J - H$, and $H - K$ we obtained $\text{ZP}_{B - V} = 0.425$, $\text{ZP}_{V - I} = 0.320$, $\text{ZP}_{J - H} = 0.131$, and $\text{ZP}_{H - K} = -0.077$ mag, respectively.

Among the SN II spectra available from different sources, we select those: (1) observed in the photospheric phase, and (2) covered by B - and V -band photometry. To check the flux-calibration in the blue and red part of the optical spectra, we compute $\Delta_{x_1 - x_2} \equiv (x_1 - x_2)_{\text{phot}} - (x_1 - x_2)_{\text{spec}}$ using the $B - V$ and $V - I$ colours, respectively, while for the near-IR spectra we use the $J - H$ and $H - K$ colours, respectively. We also compute the intrinsic $B - V$ colour to represent the shape of the SED. For optical spectra we compute this quantity from dereddened and deredshifted spectra, while for near-IR we compute the intrinsic $B - V$ colour from the photometry (see Section C).

Fig. 5.1 shows the values of $\Delta_{B - V}$ and $\Delta_{V - I}$ (top), and $\Delta_{J - H}$ and $\Delta_{H - K}$ (bottom), along with the intrinsic $B - V$ values for the collected spectra. For the SN II spectra library, we select spectra with $|\Delta_{x_1 - x_2}| < 0.1$ mag. Finally, we correct spectra for redshift and for Galactic and host galaxy extinction, assuming a Fitzpatrick (1999) extinction curve with $R_V = 3.1$ for both our Galaxy and hosts.

Table 5.10 summarizes the details of the spectra in the library: SN name (Column 1), Galactic colour excess (Column 2), heliocentric redshift (Columns 3), host galaxy colour excess (Column 4), and references for the data (Column 5).

¹http://ftp.stsci.edu/cdbs/current_calspec/alpha_lyr_stis_008.fits

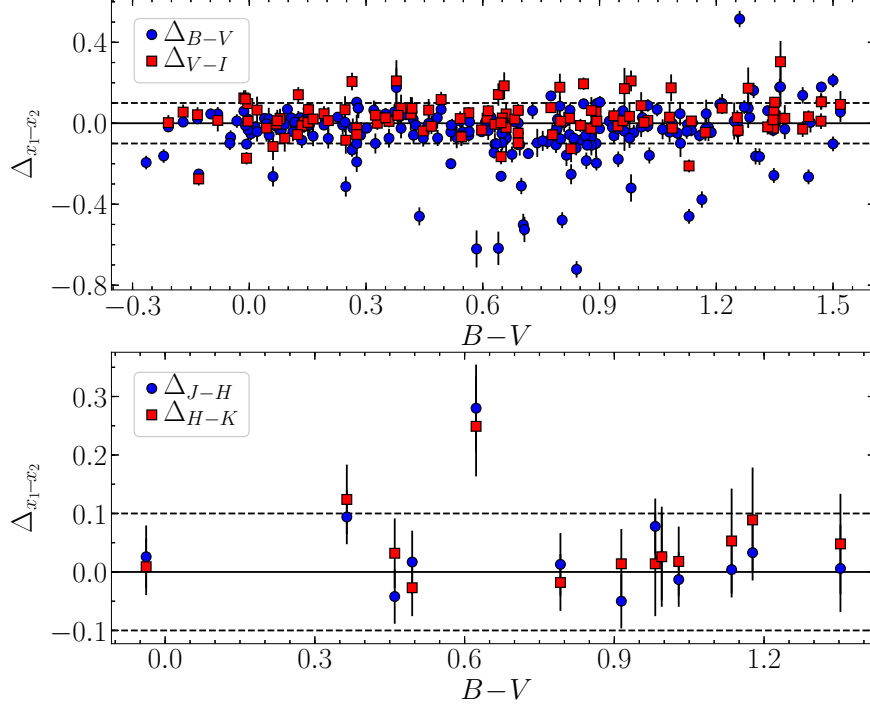


Figure 5.1: Differences between photometric and spectroscopic colours, along with the intrinsic $B-V$ colour. Dashed lines indicate differences within ± 0.1 mag.

C C3 LINEARITY

Assuming that a C3 can be well represented by a polynomial fit, the linearity of a C3 can be demonstrated if there is a high fraction of SNe II showing C3s with straight line as optimal polynomial. Due to the scarcity of K -band photometry, we use only $BVIJH$ photometry for this analysis.

With $BVIJH$ photometry set it is possible to define a total of ten colour indices and, therefore, 90 colour-colour plots (i.e., discarding one-to-one correlations). Among them, only 36 combinations give us non-superfluous information, which we analyse for host galaxy colour excess estimation.

Before computing intrinsic C3 slopes, photometry must be corrected for Galactic and host galaxy extinction, and for K -correction. Since we need the prior knowledge of the intrinsic $B-V$, we need to know in advance the value of host galaxy colour excess. For the latter, we apply zero order correction as prior values. The intrinsic $B-V$ can be computed easily from the relation between the

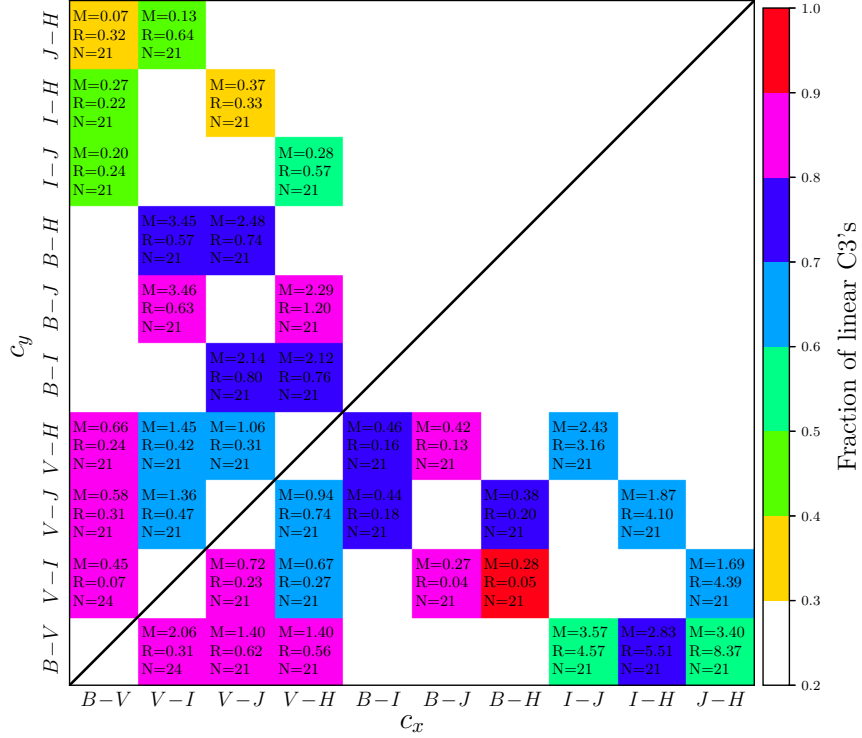


Figure 5.2: Fraction of linear C3s (colourbar) for different colour combinations, along with the median (M) and the rms (R) of the C3 slopes measured from N SNe in our set. Empty spaces correspond to superfluous colour combinations.

observed and the intrinsic $B-V$ colour, i.e.,

$$\begin{aligned}
 (B-V)_{\text{obs}} &= B-V + (R_B^G - R_V^G) \cdot E_G(B-V) \\
 &+ (K_B^S/z - K_V^S/z) \cdot z + (R_B^h - R_V^h) \cdot E_h(B-V),
 \end{aligned} \tag{5.11}$$

where $(B-V)_{\text{obs}}$ is the observed $B-V$. In Sections 2.5, 2.6, and 2.7 we found that R_V^G , K_B^S/z , K_V^S/z are linear on $B-V$, while R_B^G , R_B^h and R_V^h are quadratic on $B-V$. Therefore, solving a quadratic equation, we can obtain $B-V$ in terms of $(B-V)_{\text{obs}}$, $E_G(B-V)$, z , $E_h(B-V)$, and the fit parameters of R_B^G , R_V^G , K_B^S/z , K_V^S/z , R_B^h , and R_V^h .

For each SN and for each colour combination, we adjust a polynomial fit. The optimum degree is determined using the AIC/BIC and the principle of parsimony.

Fig. 5.2 shows the fraction of SNe that are well represented by a straight line. In 20 of the 36 colour combinations, the number of SNe displaying a linear C3 is over 70 per cent.

Assuming the C3 linearity for different combinations, we compute slopes of all SNe in our set. For each colour combination we compute the median and rms of the C3 slopes. Fig. 5.3 shows this process for the $V-I$ versus $B-V$ C3s.

D SNID EXPLOSION EPOCHS

To estimate phases of SNe II with SNID, we follow similar procedures done by Blondin and Tonry (2007), Silverman et al. (2012), and Gutiérrez et al. (2017).

Among the spectra available from different sources, we select spectra: (1) of SNe II with explosion epoch constrained within 10 d through photometric information, where for these SNe we assume the midpoint between the last non-detection and the first detection as the explosion epoch ($t_{0,\text{ln}}$), (2) spanning a rest-frame wavelength range from 4100 Å to 7000 Å with a $S/N \gtrsim 10 \text{ Å}^{-1}$, and (3) within 40 d since the explosion epoch. We do not include spectra at > 40 d since explosion because in the literature it is less abundant than spectra at earlier epochs (see, for example, Fig. 5 in Gutiérrez et al. 2017) which could bias the age determination toward earlier epochs, and also because at late time the spectral evolution is slower than at early phases, which makes more difficult to accurately determine ages with SNID (Blondin and Tonry 2007). If for a given epoch a SN has several spectra within one day, then we keep that with higher S/N . With the aforementioned constraints, we generate a SNID template library with 242 spectra of 56 SNe II, where each spectrum is corrected by heliocentric redshift. Details of this SN II templates library are summarized in Table 5.11.

Fig 5.4 shows the phase distribution of the templates. The library has, on average, 6 spectra per day, while almost all the variation is within ± 2 rms around the mean.

To create the template library, we run the `logwave` routine (which is part of the SNID program) with the options `w0=3000 w1=8400 nw=1024`. This generates SNID spectral templates with a bin in the logarithmic wavelength space of $\ln(8400/3000)/1024 \approx 0.001$, equivalent to 300 km s^{-1} .

Once the template library is created, the next step is to test how good are the phases since explosion computed with SNID and our new library. To do this, we run SNID with each library spectrum as input, using the `avoid` option to avoid templates of the same SN. We record all phases and `rlap`

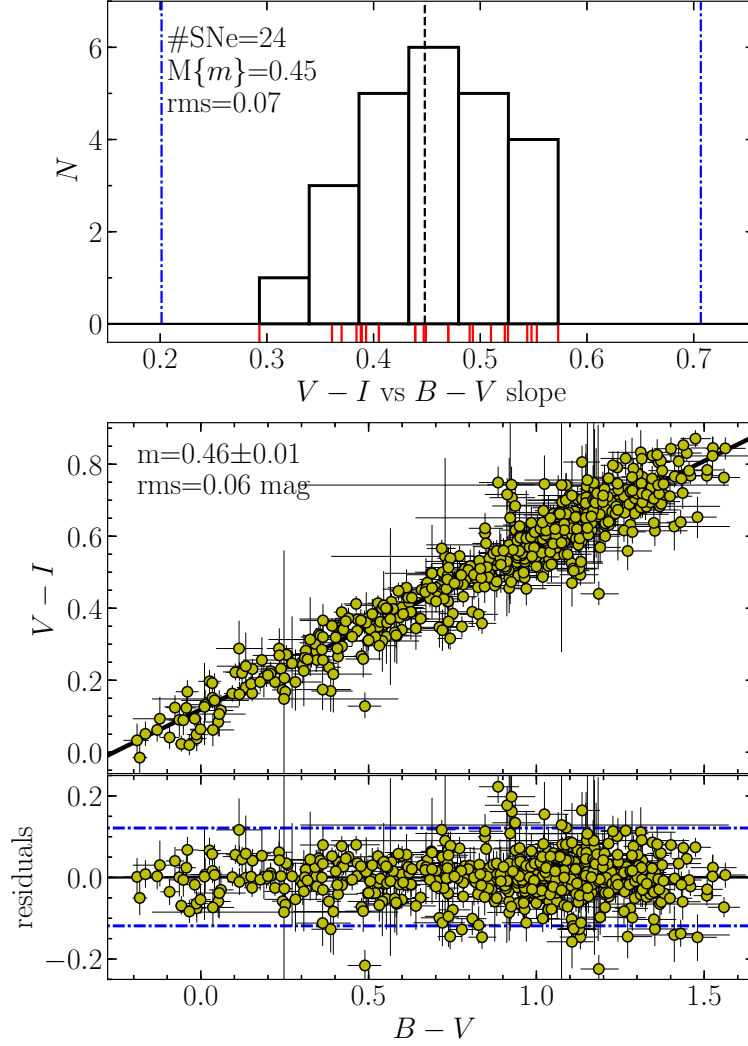


Figure 5.3: Top: $V-I$ versus $B-V$ C3 slopes distribution for the SNe in our set. Red ticks mark the specific slope values, and black dashed line marks the median of the slopes. Bottom: $V-I$ versus $B-V$ diagram showing the 24 SNe II dereddened using host galaxy colour excesses from the C3 method, along with residuals. In both panels, blue dash-dotted lines are the inner fences.

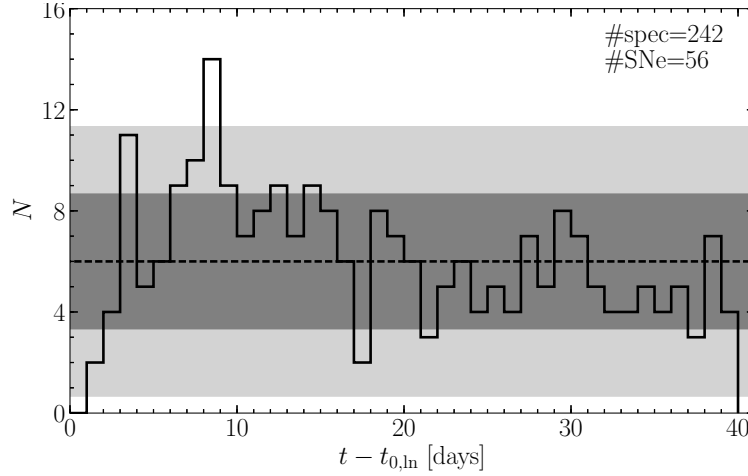


Figure 5.4: Phase distribution of the templates in our SNID SN II library. The dashed line indicates the average of spectra per bin, while dark gray and light gray regions contain values within ± 1 rms and ± 2 rms around the mean, respectively.

values (which indicate the correlation strength) of the templates found to be similar to the input spectrum and with a redshift within ± 0.01 . The top panel of Fig. 5.5 shows the 2D histogram of differences between phases since explosion estimated from last non-detection and from SNID, versus r_{lap} . To correlate r_{lap} with a rms error in phase, we compute the rms of phase differences in bins of width $2 r_{\text{lap}}$, which is shown at bottom of Fig. 5.5. To convert r_{lap} to a rms error, we fit a $1/r_{\text{lap}}$ polynomial of order 2 (determined by the AIC/BIC), given by

$$\text{rms} = (3.0 + 72.0/r_{\text{lap}} - 75.0/r_{\text{lap}}^2) \text{ d.} \quad (5.12)$$

In general, only one spectrum (e.g., the earliest) is used to estimate explosion epochs with SNID (e.g., Anderson et al. 2014b; Gutiérrez et al. 2017). We expect, however, that including all available spectra of a SN in the analysis will result in a best estimation of the explosion epoch. To explore this possibility, we select all SNe in our library with five or more spectra and perform the following procedure:

1. For each SN we randomly choose one spectrum, computing the explosion epoch ($t_{0,\text{SNID}}$) and $t_{0,\text{SNID}} - t_{0,\text{ln}}$.
2. We compute the median (i.e., the offset) and the rms of the $t_{0,\text{SNID}} - t_{0,\text{ln}}$ distribution.
3. We repeat steps 1 and 2 10^2 times, recording the median of the offsets and the rms values.

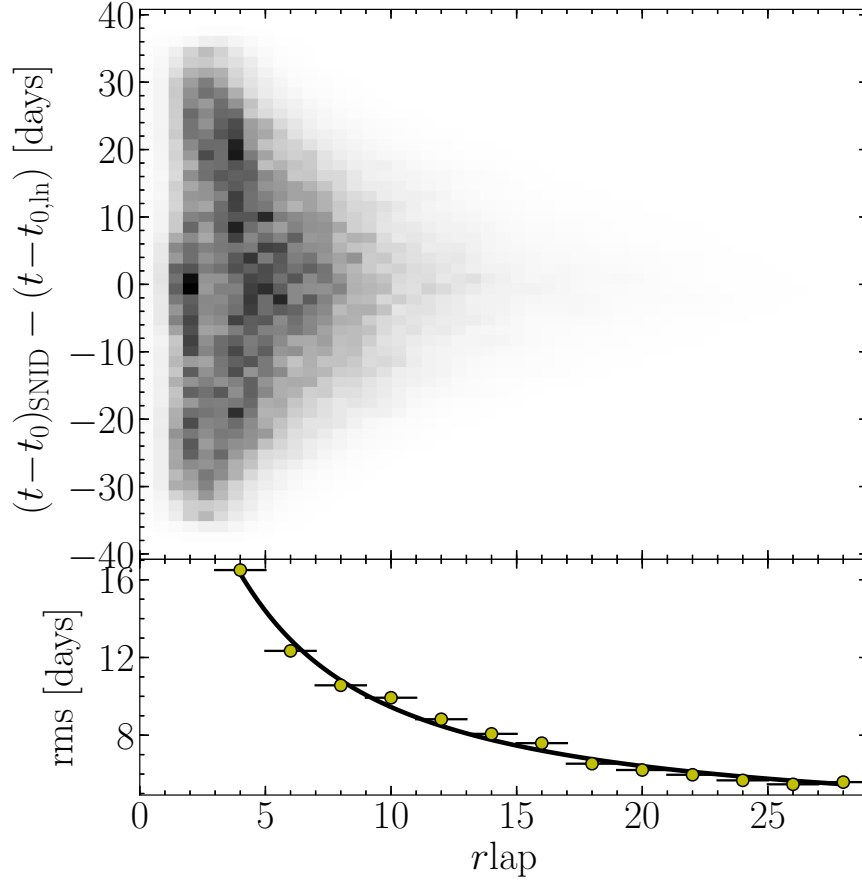


Figure 5.5: 2D histogram of differences between phases since explosion estimated from last non-detection $(t-t_{0,\text{ln}})$ and from SNID $(t-t_0)_{\text{SNID}}$ versus the r_{lap} parameter (top), and the rms of phase differences versus r_{lap} (bottom).

# of input spectra	$\text{Md}(t_{0,\text{SNID}} - t_{0,\text{ln}})$ (d)	$\text{rms}(t_{0,\text{SNID}} - t_{0,\text{ln}})$ (d)
1	$-0.6^{+1.0}_{-0.6}$	$5.0^{+0.9}_{-0.6}$
2	$-0.7^{+0.9}_{-0.7}$	$4.1^{+0.9}_{-0.4}$
3	$-0.6^{+0.6}_{-0.9}$	$4.1^{+0.2}_{-0.4}$

Table 5.1: Result of SNID simulations.

4. We repeat steps 1–3, but now randomly choosing two and then three spectra per SN as input.

Table 5.1 shows the result of the aforementioned process, i.e., the offset and the rms as a function of the number of input spectra. Using only one spectrum we obtain a typical rms of 5.0 d, which is similar than the rms of 5.2 d reported by Gutiérrez et al. (2017). We see that using more than one spectrum the rms is reduced down to 4.1 d. The median of the offsets is around -0.6 d, independent of the number of input spectra in the analysis. This offset means that explosion epochs computed with SNID are 0.6 d earlier than those estimated with the non-detection. Hereafter, for the explosion epochs derived with SNID we assume an intrinsic error of 5.0 d when only one spectrum is used, or 4.1 d whether more spectra are available.

E THE DISTANCE TO NGC 6946

The distance to NGC 6946, host of SN 2004et, was measured with the TRGB method by Tikhonov (2014, hereafter T14), Murphy et al. (2018, hereafter M18), and Anand et al. (2018, hereafter A18), and correspond to $\mu = 29.39 \pm 0.14$ mag in the Jang and Lee (2017b) calibration. The PMM *J*-band distance for SN 2004et obtained in this work ($\mu_J = 28.83 \pm 0.12$ mag) is in conflict with the TRGB estimation. To investigate the reason for this discrepancy, we compute distances to other two SNe II that exploded in NGC 6946: SN 1980K and SN 2002hh. These SNe have near-IR photometry, but we did not include them into the analysis because they do not have photometry in the five bands we use (i.e., *BVIJH*).

Using data given in Table 5.2, we obtain $\mu_J = 28.73 \pm 0.18$ and 28.77 ± 0.11 mag for SN 1980K and SN 2002hh, respectively, which are consistent with the distance computed with SN 2004et. There is then a tension of at least ~ 4 rms between the PMM and the TRGB distance. This discrepancy

SN	Δt (d)	J (mag)	v_{ph} (km s ⁻¹)	$E_h(B-V)$ (mag)	References*
1980K	54.4 ^{+7.7} _{-7.2}	11.29 ^{+0.06} _{-0.05}	4013 ⁺¹⁶⁵ ₋₁₄₃	0.0	1, 2, 3, 4, 5
2002hh	44.5 ^{+2.0} _{-2.0}	12.30 ^{+0.04} _{-0.04}	4714 ⁺⁵³ ₋₅₆	2.74 \pm 0.11 [†]	6, 7, 8, 9

[†] The colour excess was computed adopting the Cardelli et al. (1989) extinction curve and $R_V = 1.9$ (Pozzo et al. 2006). For that extinction curve, we obtained $R_J^h = 0.402$.

* (1) IAUC 3532; (2) Thompson (1982); (3) Dwek et al. (1983); (4) Schmidt et al. (1992); (5) WISEREP; (6) IAUC 8005; (7) IAUC 8024; (8) Pozzo et al. (2006); (9) Faran et al. (2014b).

Table 5.2: Observed quantities of SN 1980K and SN 2002hh.

could be due to: (1) all three SNe II are intrinsically brighter at least 0.56 mag than the SNe II we use for the calibration, or (2) there are issues with the TRGB distances reported by T14, M18, and A18. We noted that the latter two independent studies used almost the same data but obtained significantly different values of the TRGB F814W magnitude ($F814W_{\text{TRGB}}$): 26.00 ± 0.04 mag in M18 and 25.84 ± 0.11 mag in A18. T14 used another set of image data, which is closer to center of the galaxy than those used in M18 and A18, and obtained a lower $F814W_{\text{TRGB}}$ value (25.79 ± 0.05 mag). At this moment, the origin of this large discrepancy is unclear. Taking into account this, we safely remove SN 2004et from the calibration and the final sample.

F AKA CORRECTION

Given the apparent x -band magnitude observed at epoch t_i , $m_{x,i}$, the x -band magnitude corrected for effects of Galactic colour excess E_{B-V}^G , redshift $z_{\text{helio}}^{\text{SN}}$, and host galaxy colour excess E_{B-V}^h is given by

$$m_{x,i}^{\text{AKA}} = m_{x,i} - A_{x,i}^G - K_{x,i} - A_{x,i}^h, \quad (5.13)$$

where

$$A_{x,i}^G = -2.5 \log \left[\frac{\int d\lambda S_{x,\lambda} f_{\lambda',i} \lambda' 10^{-0.4(R_{\lambda'}^h E_{B-V}^h + R_{\lambda}^G E_{B-V}^G)}}{\int d\lambda S_{x,\lambda} f_{\lambda',i} \lambda' 10^{-0.4R_{\lambda'}^h E_{B-V}^h}} \right] \quad (5.14)$$

is the Galactic broad-band extinction,

$$K_{x,i} = -2.5 \log(1 + z_{\text{helio}}^{\text{SN}}) + K_{x,i}^S \quad (5.15)$$

is the K -correction, with

$$K_{x,i}^s = 2.5 \log \left[\frac{\int d\lambda S_{x,\lambda} f_{\lambda,i} \lambda 10^{-0.4R_{\lambda}^h E_{B-V}^h}}{\int d\lambda' S_{x,\lambda} f_{\lambda',i} \lambda' 10^{-0.4R_{\lambda'}^h E_{B-V}^h}} \right], \quad (5.16)$$

and

$$A_{x,i}^h \equiv -2.5 \log \left[\frac{\int d\lambda S_{x,\lambda} f_{\lambda,i} \lambda 10^{-0.4R_{\lambda}^h E_{B-V}^h}}{\int d\lambda S_{x,\lambda} f_{\lambda,i} \lambda} \right], \quad (5.17)$$

is the host galaxy broad-band extinction. In the previous expressions, λ is the wavelength in the observer's frame, $\lambda' = \lambda / (1 + z_{\text{helio}}^{\text{SN}})$ is the wavelength in the SN rest frame, $S_{x,\lambda}$ is the x -band transmission function, $f_{\lambda,i}$ is the spectral energy distribution (SED) of the SN at epoch t_i , and R_{λ}^G and R_{λ}^h are the extinction curve for our Galaxy and for the hosts galaxy, respectively. For the latter, we adopt the Fitzpatrick (1999) extinction curve with $R_V = 3.1$.

Using a SN II spectra library, R19 showed that the quotients

$$\mathcal{R}_{x,i}^G \equiv A_{x,i}^G / E_{B-V}^G, \quad (5.18)$$

$$\mathcal{K}_{x,i}^s \equiv K_{x,i}^s / z_{\text{helio}}^{\text{SN}}, \quad (5.19)$$

and

$$\mathcal{R}_{x,i}^h \equiv A_{x,i}^h / E_{B-V}^h, \quad (5.20)$$

can be expressed as polynomials on the intrinsic $B-V$ colour. These expressions rely on the prior knowledge of E_{B-V}^h . Since the latter value is not always available, we need new expressions for $\mathcal{R}_{x,i}^G$ as a function of the observed $B-V$ corrected only for E_{B-V}^G , hereafter $(B-V)_A$, and $\mathcal{K}_{x,i}^s$ as a function of the observed $B-V$ corrected for E_{B-V}^G and $z_{\text{helio}}^{\text{SN}}$, hereafter $(B-V)_{AK}$.

To compute the parameters of the polynomial fit for $\mathcal{R}_{x,i}^G$ as a function of $(B-V)_A$ and $\mathcal{K}_{x,i}^G$ as a function of $(B-V)_{AK}$, we use the same spectra library used in R19. For each spectrum we perform 100 simulations picking randomly E_{B-V}^G values between 0.0 and 0.4 mag, $z_{\text{helio}}^{\text{SN}}$ values between 0.0 and 0.04, and E_{B-V}^h values between 0.0 and 0.4 mag. Tables 5.3–5.5 lists the parameters obtained with the polynomial fitting.

Summarizing, with the knowledge of E_{B-V}^G and a measurement of the apparent $B-V$ colour at time t_i , $(B-V)_i$, we can compute the Galactic broad-band extinction using

$$A_{x,i}^G = E_{B-V}^G \sum_j g_{x,j} (B-V)_{A,i}^j, \quad (5.21)$$

x	$g_{x,0}$	$g_{x,1}$	$g_{x,2}$	rms
B	4.082	-0.097	-0.036	0.012
V	3.088	-0.042	-0.004	0.008
I	1.720	-0.004	—	0.005
J	0.8129	—	—	0.0013
H	0.5181	—	—	0.0005

Note: $\mathcal{R}_{x,(B-V)_A}^G = g_{x,0} + g_{x,1}(B-V)_A + g_{x,2}(B-V)_A^2$.

Fits are valid for $E_{B-V}^G \leq 0.4$ mag, $z_{\text{helio}}^{\text{SN}} \leq 0.04$, and $E_{B-V}^h \leq 0.4$ mag.

Table 5.3: Fits parameters for $\mathcal{R}_{x,(B-V)_A}^G$

x	$k_{x,0}$	$k_{x,1}$	rms
B	-0.227	6.116	0.499
V	-0.870	3.089	0.380
I	-0.479	1.443	0.543
J	-0.655	—	0.318
H	-0.743	—	0.165

Note: $\mathcal{K}_{x,(B-V)_{AK}}^S = k_{x,0} + k_{x,1}(B-V)_{AK}$.

Fits are valid for $z_{\text{helio}}^{\text{SN}} \leq 0.04$ and $E_{B-V}^h \leq 0.4$ mag.

Table 5.4: Fits parameters for $\mathcal{K}_{x,(B-V)_{AK}}^S$

x	$h_{x,0}$	$h_{x,1}$	$h_{x,2}$	rms
B	4.081	-0.101	-0.046	0.010
V	3.089	-0.033	-0.010	0.007
I	1.723	-0.006	—	0.004
J	0.8138	—	—	0.0012
H	0.5186	—	—	0.0004

Note: $\mathcal{R}_{x,(B-V)_0}^h = h_{x,0} + h_{x,1}(B-V)_0 + h_{x,2}(B-V)_0^2$.

Fits are valid for $E_{B-V}^h \leq 0.4$ mag.

Table 5.5: Fits parameters for $\mathcal{R}_{x,(B-V)_A}^h$

where $(B-V)_{A,i}$ is the solution of the quadratic equation

$$(B-V)_{A,i} = (B-V)_i - [0.994 - 0.055(B-V)_{A,i} - 0.032(B-V)_{A,i}^2] \cdot E_{B-V}^G. \quad (5.22)$$

Similarly, with the knowledge of $z_{\text{helio}}^{\text{SN}}$ and $(B-V)_{A,i}$, we can compute the K -correction using

$$K_{x,i} = -2.5 \log(1 + z_{\text{helio}}^{\text{SN}}) + z_{\text{helio}}^{\text{SN}} \sum_j k_{x,j} (B-V)_{AK,i}^j, \quad (5.23)$$

where

$$(B-V)_{AK,i} = \frac{(B-V)_{A,i} - 0.643 z_{\text{helio}}^{\text{SN}}}{1 + 3.027 z_{\text{helio}}^{\text{SN}}}. \quad (5.24)$$

And finally, with the knowledge of E_{B-V}^h and $(B-V)_{AK,i}$, we can compute the host galaxy broad-band extinction using

$$A_{x,i}^h = E_{B-V}^h \sum_j h_{x,j} (B-V)_{0,i}^j, \quad (5.25)$$

where $(B-V)_{0,i}$ is the solution of the quadratic equation

$$(B-V)_{0,i} = (B-V)_{AK,i} - [0.992 - 0.068(B-V)_{0,i} - 0.036(B-V)_{0,i}^2] \cdot E_{B-V}^h. \quad (5.26)$$

G ADDITIONAL TABLES

x	$c_{0,x}$	$c_{1,x}$	$c_{2,x}$	rms	$p(\text{RM})$
$R_x^G = c_{0,x} + c_{1,x}(B-V) + c_{2,x}(B-V)^2$					
B	$4.074^{+0.003}_{-0.003}$	$-0.107^{+0.014}_{-0.012}$	$-0.046^{+0.010}_{-0.011}$	0.009	0.42
V	$3.089^{+0.002}_{-0.002}$	$-0.048^{+0.003}_{-0.002}$...	0.006	0.32
I	$1.722^{+0.002}_{-0.002}$	$-0.004^{+0.002}_{-0.002}$...	0.003	0.86
J	$0.8135^{+0.0008}_{-0.0008}$	0.0012	0.67
H	$0.5184^{+0.0003}_{-0.0003}$	0.0004	0.43
K	$0.3484^{+0.0001}_{-0.0001}$	0.0001	0.46
$K_x^S/z = c_{0,x} + c_{1,x}(B-V)^{\dagger,\diamond}$					
B	$0.51^{+0.06}_{-0.06}$	$6.23^{+0.09}_{-0.09}$...	0.41	0.23
V	$-0.51^{+0.05}_{-0.05}$	$2.87^{+0.07}_{-0.07}$...	0.35	0.13
I	$-0.40^{+0.11}_{-0.11}$	$1.14^{+0.17}_{-0.17}$...	0.46	0.53
J	$-0.77^{+0.09}_{-0.09}$	0.21	0.63
H	$-0.82^{+0.05}_{-0.05}$	0.14	0.58
K	$-1.40^{+0.05}_{-0.05}$	0.15	0.61
$R_x^h = c_{0,x} + c_{1,x}(B-V) + c_{2,x}(B-V)^2$					
B	$4.085^{+0.002}_{-0.003}$	$-0.097^{+0.011}_{-0.010}$	$-0.049^{+0.008}_{-0.009}$	0.008	0.97
V	$3.092^{+0.002}_{-0.002}$	$-0.034^{+0.007}_{-0.007}$	$-0.009^{+0.006}_{-0.005}$	0.006	0.26
I	$1.724^{+0.002}_{-0.002}$	$-0.005^{+0.002}_{-0.002}$...	0.003	0.95
J	$0.8140^{+0.0008}_{-0.0009}$	0.0012	0.60
H	$0.5187^{+0.0002}_{-0.0003}$	0.0004	0.36
K	$0.3485^{+0.0001}_{-0.0001}$	0.0001	0.58

Fits are valid for $-0.2 < B-V < 1.5$ and $-0.05 < B-V < 1.35$ for BVI and JHK , respectively (\dagger), and $z < 0.032$ (\diamond). Errors are the 99 per cent CI.

Table 5.7: Fits parameters for R_x^G , K_x^S/z , and R_x^h .

SN	$E_h(B-V)$ $\{B-V, V-I\}$	O10	Discovery (JD)	t_{ln}^a (d)	t_{fd}^a (d)	$t_{0,\text{SNID}}^a$ (d)	$t_{0,\text{final}}^a$ (d)	References ^d
1999em	$0.035^{+0.105}_{-0.105}$ (0.082)	0.106(0.052)	2451480.94	-8.99	-1.43	-6.37(4.16)	$-5.57^{+2.96}_{-2.63}$	IAUC7294, E03
2002gd	$0.154^{+0.111}_{-0.106}$ (0.084)	...	2452553.37	-4.09^b	-2.84^b	0.73(4.48)	$-3.42^{+0.46}_{-0.53}$	IAUC7986, IAUC7990
2002gw	$0.202^{+0.106}_{-0.108}$ (0.084)	0.132(0.061)	2452560.77	-31.218	-1.637	-4.29(4.28)	$-5.74^{+3.22}_{-4.73}$	IAUC7995, IAUC7996
2002hj	$0.086^{+0.106}_{-0.106}$ (0.083)	0.068(0.100)	2452567.98	-11.48	0.0	-11.61(4.40)	$-8.56^{+4.18}_{-2.37}$	IAUC8006
2003B	$0.064^{+0.117}_{-0.122}$ (0.093)	0.004(0.081)	2452645.0	...	-8.41	-22.83(4.32)	$-22.83^{+5.61}_{-5.57}$	IAUC8042, IAUC8058
2003E	$0.299^{+0.148}_{-0.148}$ (0.115)	0.358(0.100)	2452644.8	-39.0	0.0	-9.25(4.40)	$-9.36^{+5.54}_{-5.56}$	IAUC8044
2003T	$0.144^{+0.135}_{-0.137}$ (0.106)	0.175(0.100)	2452664.9	-20.0	0.0	-11.91(5.19)	$-11.57^{+6.18}_{-5.54}$	IAUC8058
2003bl	$0.107^{+0.121}_{-0.127}$ (0.097)	0.004(0.052)	2452701.0	-262.2	0.0	-13.53(5.79)	$-13.64^{+7.23}_{-7.35}$	IAUC8086
2003bn	$0.019^{+0.113}_{-0.114}$ (0.089)	0.038(0.052)	2452697.98	-6.48	-5.15	-4.42(4.46)	$-5.80^{+0.52}_{-0.55}$	IAUC8088
2003ci	$0.098^{+0.138}_{-0.135}$ (0.107)	0.147(0.100)	2452719.9	-16.0	0.0	-21.56(4.57)	$-14.28^{+3.15}_{-1.45}$	IAUC8097
2003cn	$0.072^{+0.105}_{-0.110}$ (0.084)	0.003(0.081)	2452727.9	-22.0	0.0	-6.77(4.55)	$-7.16^{+4.88}_{-5.67}$	IAUC8101
2003hn	$0.181^{+0.134}_{-0.132}$ (0.104)	0.192(0.081)	2452877.2	-20.7	0.0	-11.07(4.31)	$-11.03^{+5.37}_{-5.32}$	IAUC8186
2004et	$0.053^{+0.124}_{-0.126}$ (0.097)	0.048(0.081)	2453275.5	-4.983	-4.017	-1.83(4.29)	$-4.48^{+0.38}_{-0.40}$	IAUC8413
2005ay	$0.045^{+0.120}_{-0.121}$ (0.094)	...	2453456.58	-7.459	0.0	-8.23(4.29)	$-5.03^{+3.19}_{-1.97}$	IAUC8500, IAUC8502
2005cs	$0.054^{+0.115}_{-0.116}$ (0.090)	0.045(0.052)	2453550.407	-1.977	-0.997	-6.18(4.28)	$-1.52^{+0.42}_{-0.37}$	IAUC8553, P09
2008in	$-0.031^{+0.142}_{-0.137}$ (0.109)	...	2454827.29	-2.84	-2.34	-3.91(4.27)	$-2.60^{+0.21}_{-0.19}$	CBET1636, R11
2009N	$0.289^{+0.164}_{-0.165}$ (0.128)	...	2454856.36	-21.86	0.0	-3.29(4.27)	$-4.50^{+3.47}_{-4.74}$	CBET1670
2009ib	$0.120^{+0.133}_{-0.133}$ (0.104)	...	2455049.8	-166.25	0.0	-9.04(4.55)	$-9.25^{+5.52}_{-5.63}$	CBET1902
2009md	$0.145^{+0.133}_{-0.133}$ (0.104)	...	2455170.31	-15.81	0.0	... ^c	$-7.91^{+6.32}_{-6.32}$	CBET2065, F11
2012A	$0.108^{+0.127}_{-0.126}$ (0.099)	...	2455933.887	-9.387	0.0	... ^c	$-4.69^{+3.75}_{-3.75}$	CBET2974
2012aw	$0.039^{+0.124}_{-0.122}$ (0.096)	...	2456003.36	-1.591	-0.011	-1.44(4.20)	$-0.81^{+0.63}_{-0.63}$	CBET3054, ATel3996
2012ec	$0.085^{+0.124}_{-0.119}$ (0.095)	...	2456150.539	-135.289	0.0	-3.69(4.33)	$-4.75^{+3.62}_{-5.08}$	CBET3201
2013ej	$-0.028^{+0.130}_{-0.127}$ (0.100)	...	2456498.95	-1.91	-1.325	-10.22(4.21)	$-1.64^{+0.25}_{-0.22}$	CBET3606, ATel5237, CF
2014G	$0.315^{+0.145}_{-0.144}$ (0.112)	...	2456672.074	-3.724	-0.963	-0.43(4.65)	$-2.26^{+1.03}_{-1.17}$	CBET3787

Column 1: SN names. Columns 2: host galaxy colour excesses estimated with the $V-I$ versus $B-V$ C3, where errors correspond to the 80 per cent CI, and the rms in parenthesis. Column 3: host galaxy colour excesses from Olivares E. et al. (2010) recalibrated by R14, with rms in parenthesis. Column 4: discovery epochs. Column 5 and 6: last non-detection and first detection epochs, respectively. Column 7 and 8: explosion epochs estimated with SNID and our SN II template library, without any prior (rms error in parenthesis) and with photometric priors, respectively. Column 9: references for discovery, last non-detection, and first detection epochs.

^a Epochs with respect to the discovery epoch.

^b Value obtained through polynomial fits to pre-maximum VRI photometry.

^c Optical spectra not published.

^d E03: Elmhamdi et al. (2003); P09: Pastorello et al. (2009); R11: Roy et al. (2011); F11: Fraser et al. (2011); CF: C. Feliciano report on the *Bright Supernova* website (<http://www.rochesterastronomy.org/snimages/>).

Table 5.8: SN II parameters.

Galaxy	cz_{CMB} (km s $^{-1}$)	SN	μ_B	μ_V	μ_I	μ_J	μ_H
NGC 6946	-141(382)	2004et	28.40 $^{+0.60}_{-0.60}$ (0.47)	28.57 $^{+0.45}_{-0.45}$ (0.35)	28.67 $^{+0.27}_{-0.27}$ (0.21)	28.83 $^{+0.15}_{-0.15}$ (0.12)	28.75 $^{+0.11}_{-0.11}$ (0.09)
M74	359(383)	2013ej	30.21 $^{+0.56}_{-0.56}$ (0.44)	30.08 $^{+0.42}_{-0.42}$ (0.33)	30.02 $^{+0.25}_{-0.25}$ (0.20)	29.94 $^{+0.14}_{-0.14}$ (0.11)	29.94 $^{+0.11}_{-0.11}$ (0.09)
M51a	636(382)	2005cs	29.62 $^{+0.51}_{-0.51}$ (0.40)	29.57 $^{+0.39}_{-0.39}$ (0.30)	29.54 $^{+0.24}_{-0.24}$ (0.19)	29.61 $^{+0.14}_{-0.14}$ (0.11)	29.61 $^{+0.11}_{-0.11}$ (0.09)
NGC 1637	670(382)	1999em	30.22 $^{+0.47}_{-0.47}$ (0.37)	30.26 $^{+0.36}_{-0.36}$ (0.28)	30.29 $^{+0.23}_{-0.23}$ (0.18)	30.30 $^{+0.15}_{-0.15}$ (0.12)	30.33 $^{+0.13}_{-0.13}$ (0.10)
NGC 3938	1038(382)	2005ay	31.65 $^{+0.53}_{-0.53}$ (0.41)	31.66 $^{+0.40}_{-0.40}$ (0.31)	31.68 $^{+0.25}_{-0.25}$ (0.20)	31.75 $^{+0.15}_{-0.15}$ (0.12)	31.79 $^{+0.13}_{-0.13}$ (0.10)
NGC 3239	1084(383)	2012A	29.81 $^{+0.57}_{-0.57}$ (0.45)	30.01 $^{+0.45}_{-0.45}$ (0.35)	30.13 $^{+0.30}_{-0.30}$ (0.24)	30.35 $^{+0.23}_{-0.23}$ (0.18)	30.33 $^{+0.21}_{-0.21}$ (0.16)
NGC 1448	1102(382)	2003hn	30.89 $^{+0.58}_{-0.58}$ (0.45)	31.02 $^{+0.45}_{-0.45}$ (0.35)	31.10 $^{+0.29}_{-0.29}$ (0.22)	31.14 $^{+0.19}_{-0.19}$ (0.15)	31.19 $^{+0.16}_{-0.16}$ (0.13)
NGC 1097	1105(382)	2003B	31.60 $^{+0.53}_{-0.53}$ (0.41)	31.67 $^{+0.42}_{-0.42}$ (0.32)	31.75 $^{+0.28}_{-0.28}$ (0.22)	31.95 $^{+0.21}_{-0.21}$ (0.17)	31.91 $^{+0.19}_{-0.19}$ (0.15)
M95	1127(383)	2012aw	30.00 $^{+0.54}_{-0.54}$ (0.42)	30.06 $^{+0.41}_{-0.41}$ (0.32)	30.07 $^{+0.25}_{-0.25}$ (0.19)	30.01 $^{+0.14}_{-0.14}$ (0.11)	29.98 $^{+0.11}_{-0.11}$ (0.09)
NGC 1084	1196(382)	2012ec	31.16 $^{+0.54}_{-0.54}$ (0.42)	31.24 $^{+0.43}_{-0.43}$ (0.33)	31.32 $^{+0.29}_{-0.29}$ (0.23)	31.37 $^{+0.21}_{-0.21}$ (0.16)	31.36 $^{+0.19}_{-0.19}$ (0.15)
NGC 1559	1304(382)	2009ib	31.81 $^{+0.59}_{-0.59}$ (0.46)	31.85 $^{+0.47}_{-0.47}$ (0.37)	31.87 $^{+0.32}_{-0.32}$ (0.25)	31.86 $^{+0.26}_{-0.26}$ (0.20)	31.73 $^{+0.38}_{-0.38}$ (0.29)
NGC 4487	1385(383)	2009N	31.00 $^{+0.70}_{-0.70}$ (0.55)	31.10 $^{+0.53}_{-0.53}$ (0.42)	31.18 $^{+0.32}_{-0.32}$ (0.25)	31.30 $^{+0.19}_{-0.19}$ (0.15)	31.25 $^{+0.16}_{-0.16}$ (0.13)
NGC 3448	1528(382)	2014G	31.62 $^{+0.62}_{-0.62}$ (0.49)	31.92 $^{+0.47}_{-0.47}$ (0.37)	32.05 $^{+0.28}_{-0.28}$ (0.22)	32.05 $^{+0.21}_{-0.21}$ (0.17)	32.26 $^{+0.18}_{-0.18}$ (0.14)
NGC 3389	1656(383)	2009md	31.89 $^{+0.67}_{-0.67}$ (0.53)	32.06 $^{+0.55}_{-0.55}$ (0.43)	32.13 $^{+0.43}_{-0.43}$ (0.34)	32.22 $^{+0.39}_{-0.39}$ (0.31)	32.17 $^{+0.37}_{-0.37}$ (0.29)
M61	1913(383)	2008in	31.81 $^{+0.60}_{-0.60}$ (0.47)	31.58 $^{+0.45}_{-0.45}$ (0.35)	31.53 $^{+0.27}_{-0.27}$ (0.21)	31.39 $^{+0.15}_{-0.15}$ (0.12)	31.35 $^{+0.11}_{-0.11}$ (0.09)
NGC 7537	2303(383)	2002gd	32.61 $^{+0.49}_{-0.49}$ (0.38)	32.61 $^{+0.37}_{-0.37}$ (0.29)	32.63 $^{+0.24}_{-0.24}$ (0.19)	32.72 $^{+0.16}_{-0.16}$ (0.13)	32.75 $^{+0.14}_{-0.14}$ (0.11)
NGC 922	2878(382)	2002gw	32.81 $^{+0.48}_{-0.48}$ (0.37)	33.08 $^{+0.37}_{-0.37}$ (0.29)	33.22 $^{+0.24}_{-0.24}$ (0.19)	33.32 $^{+0.17}_{-0.17}$ (0.14)	33.38 $^{+0.16}_{-0.16}$ (0.13)
LEDA 831618	4172(385)	2003bn	33.79 $^{+0.51}_{-0.51}$ (0.40)	33.93 $^{+0.39}_{-0.39}$ (0.30)	34.00 $^{+0.24}_{-0.24}$ (0.19)	33.99 $^{+0.21}_{-0.21}$ (0.16)	34.01 $^{+0.17}_{-0.17}$ (0.13)
MCG -04-12-4	4379(382)	2003E	33.44 $^{+0.64}_{-0.64}$ (0.50)	33.78 $^{+0.49}_{-0.49}$ (0.38)	34.00 $^{+0.30}_{-0.30}$ (0.24)	33.94 $^{+0.22}_{-0.22}$ (0.17)	33.93 $^{+0.17}_{-0.17}$ (0.14)
NGC 5374	4652(383)	2003bl	33.85 $^{+0.54}_{-0.54}$ (0.42)	34.13 $^{+0.43}_{-0.43}$ (0.34)	34.27 $^{+0.30}_{-0.30}$ (0.24)	34.35 $^{+0.23}_{-0.23}$ (0.18)	34.30 $^{+0.22}_{-0.22}$ (0.17)
IC 849	5753(383)	2003cn	34.10 $^{+0.51}_{-0.51}$ (0.40)	34.22 $^{+0.42}_{-0.42}$ (0.33)	34.24 $^{+0.32}_{-0.32}$ (0.25)	34.37 $^{+0.28}_{-0.28}$ (0.22)	34.40 $^{+0.26}_{-0.26}$ (0.20)
NPM1G +04.0097	6884(382)	2002hj	34.94 $^{+0.47}_{-0.47}$ (0.37)	35.00 $^{+0.36}_{-0.36}$ (0.28)	35.08 $^{+0.23}_{-0.23}$ (0.18)	35.08 $^{+0.15}_{-0.15}$ (0.12)	35.26 $^{+0.13}_{-0.13}$ (0.11)
UGC 4864	8662(383)	2003T	35.36 $^{+0.59}_{-0.59}$ (0.46)	35.33 $^{+0.47}_{-0.47}$ (0.36)	35.32 $^{+0.32}_{-0.32}$ (0.25)	35.45 $^{+0.24}_{-0.24}$ (0.18)	35.56 $^{+0.22}_{-0.22}$ (0.16)
UGC 6212	9468(384)	2003ci	36.07 $^{+0.62}_{-0.62}$ (0.49)	35.81 $^{+0.49}_{-0.49}$ (0.40)	35.69 $^{+0.33}_{-0.33}$ (0.29)	35.61 $^{+0.26}_{-0.26}$ (0.25)	35.51 $^{+0.24}_{-0.24}$ (0.24)

Note: We adopt $R_V = 3.1$ for both our Galaxy and hosts. Errors correspond to the 80 per cent CI, with the rms in parenthesis, and include the TRGB zero-point systematic error.

Table 5.9: CMB redshifts and PMM distance moduli.

SN	$E_G(B-V)^a$ (mag)	cz_{helio} (km s ⁻¹)	$E_h(B-V)^b$ (mag)	References ^d	SN	$E_G(B-V)^a$ (mag)	cz_{helio} (km s ⁻¹)	$E_h(B-V)^b$ (mag)	References ^d
1990E	0.022	1362	0.616	1	2003Z	0.033	1289	0.065	5, 7
1992ba	0.050	1135	0.049	2	2003bl	0.023	4295	0.103	2
1996W	0.036	1617	0.252	3	2003bn	0.056	3897	0.019	2
1999br	0.020	957	0.151	4	2003cn	0.018	5430	0.078	2
1999ca	0.094	2791	0.054	2	2003ef	0.040	4093	0.272	2
1999cr	0.085	6134	0.168	2	2003gd	0.060	657	0.166	5, 2
1999em ^c	0.035	800	0.036	5, 2	2003hg	0.064	4186	0.440	2
2000dc	0.068	3117	0.372	6	2003hl	0.062	2123	0.328	5, 2
2000dj	0.062	4744	0.106	5	2003hn	0.012	1305	0.184	2
2001X	0.034	1480	0.061	5	2003ho	0.033	4091	0.764	2
2001cm	0.012	3412	0.183	5	2003ib	0.041	7442	0.165	2
2001cy	0.179	4478	0.016	6	2003ip	0.052	5398	0.114	2
2001do	0.163	3124	0.318	6	2003iq	0.062	2331	0.127	5, 2
2001fa	0.067	5182	0.125	6	2004du	0.082	5025	0.123	5
2001hg	0.031	2387	0.119	5	2005ay	0.018	850	0.047	5
2002an	0.031	3870	0.000	5	2005cs	0.032	463	0.054	5, 8, 9
2002ca	0.020	3277	0.086	5	2009N	0.018	905	0.288	10, 2
2002gd	0.058	2536	0.157	5, 2	2009dd	0.017	757	0.107	3
2002gw	0.016	3143	0.203	2	2009ib	0.026	1304	0.119	11
2002hj	0.101	7079	0.088	2	2012aw ^c	0.024	778	0.041	12
2002hx	0.045	9299	0.115	2	2012ec ^c	0.023	1407	0.088	13
2003B	0.023	1141	0.064	2	2013ej ^c	0.060	657	-0.028	14, 15, 16
2003E	0.041	4484	0.297	2	2014G	0.010	1160	0.313	17

^a Values from Schlafly and Finkbeiner (2011).

^b Values computed in this work.

^c SN with useful near-IR spectra.

^d (1) Schmidt et al. (1993); (2) Gutiérrez et al. (2017); (3) Inserra et al. (2013); (4) Pastorello et al. (2004); (5) Faran et al. (2014b); (6) Faran et al. (2014a); (7) Spiro et al. (2014); (8) Pastorello et al. (2006); (9) Pastorello et al. (2009); (10) Takáts et al. (2014); (11) Takáts et al. (2015); (12) Dall’Ora et al. (2014); (13) Barbarino et al. (2015); (14) Valenti et al. (2014); (15) Dhungana et al. (2016); (16) Yuan et al. (2016); (17) Terreran et al. (2016).

Table 5.10: SN II spectra library.

SN	t_d (d)	$t_{ln} - t_d$ (d)	$t_{fd} - t_d$ (d)	$t - t_{0,ln}$ (d)	References ^c
1986L	2446711.1	-5.6	0.0	6,7,[27:33]	IAUC 4260, 1
1988A	2447179.299	-3.099	-1.968	13	IAUC 4533, IAUC 4540, 1
1990E	2447937.62	-5.12	0.0	9,19	IAUC 4965, 2
1999br	2451280.9	-8.0	0.0	15,18,25,33	IAUC 7141, IAUC 7143, 3
1999em	2451480.94	-8.99	-1.43	[7:10],12,[14:16],21,26,29,31,35,39	IAUC 7294, 4, 5, 1
1999gi	2451522.32	-6.64	0.0	4,6,7,30,35,38	IAUC 7329, IAUC 7334, 5
1999go	2451535.7	-8.0	0.0	9,10,14	IAUC 7337, 6
2000dc	2451765.8	-7.0	0.0	20	IAUC 7476, 7
2000dj	2451795.9	-10.413	0.0	23	IAUC 7490, IAUC 7491, 5
2000el	2451869.53	-33.83	-28.93	39	IAUC 7523, IAUC 7531, 6
2001X	2451968.3	-10.3	0.0	9,27,36	IAUC 7591, 5
2001do	2452135.7	-4.0	0.0	31,39	IAUC 7682, 7
2001fa	2452200.9	-5.0	0.0	[4:7],30,31	IAUC 7737, 7, 8
2002an	2452297.02	-4.98	0.0	16,22,25	IAUC 7805, IAUC 7808, 9, 5
2002ce	2452375.378	-5.678	0.0	4	IAUC 7875, 6
2002gd ^a	2452553.37	-4.09	-2.84	6,8,12,23,27,31,35,38	IAUC 7986, IAUC 7990, 5, 1
2003Z	2452669.2	-9.0	0.0	10,28,30	IAUC 8062, 5, 10
2003bn	2452697.98	-6.48	-5.15	14,18,37	IAUC 8088, 1
2003ej	2452779.8	-9.0	0.0	6,14,19,40	IAUC 8134, 1
2003hg	2452869.9	-9.0	0.0	8,32	IAUC 8184, 9, 1
2003hl	2452872.0	-9.0	0.0	12,33	IAUC 8184, 5, 1
2003iq	2452921.458	-2.988	0.0	9,16,21,29	IAUC 8219, 5, 1
2004ci	2453173.497	-4.597	-1.697	6	IAUC 8357, 6
2004er	2453273.9	-4.02	0.0	12,30	IAUC 8412, IAUC 8415, 1
2004et	2453275.5	-4.983	-4.017	9,20,24,30,35,38	IAUC 8413, 11, 5
2004fc	2453299.89	-7.0	-4.766	9,33	IAUC 8422, 1, 6
2004fx	2453316.94	-16.02	-10.01	19,31	IAUC 8431, 1, 6
2005ay	2453456.58	-7.459	0.0	7,8,19,23,25	IAUC 8500, IAUC 8502, 12, 5, 8
2005cs	2453550.407	-1.977	-0.997	4,5,9,11,[13:15],17,34,36	IAUC 8553, 13, 5, 14
2005dz	2453623.71	-7.91	0.0	6,20	IAUC 8598, 9, 1
2006Y	2453770.08	-6.99	0.0	26,32	IAUC 8668, 1
2006bc	2453819.15	-8.063	0.0	9	IAUC 8693, 1
2006bp	2453835.1	-1.423	-0.453	4,8,10,16,22,26,34	IAUC 8700, 15, 15
2006it	2454009.67	-4.98	0.0	11,14	IAUC 8758, 1
2006iw	2454011.798	-2.061	0.0	19	CBET 663, 1, 16
2007hv	2454352.87	-10.37	0.0	7	CBET 1056, 8
2007il	2454353.95	-8.01	0.0	12,26	CBET 1062, 1
2007pk	2454414.81	-4.98	0.0	3,4,6,7,28,38	CBET 1129, 17, 8
2008bh	2454548.66	-10.09	0.0	13,26,38	CBET 1311, 1
2008br	2454564.265	-4.942	0.0	7,21,29,36	CBET 1332, 1
2008ho	2454796.61	-8.84	0.0	18,23	CBET 1587, 1
2008if	2454812.71	-9.98	0.0	11,[13:17],22,29	CBET 1619, 1
2008il	2454827.64	-4.95	0.0	3	CBET 1634, 1
2009ao	2454894.62	-8.0	0.0	28,34	CBET 1711, 1
2009bz	2454919.98	-7.95	0.0	9,23,27,36	CBET 1748, 1
2009dd	2454935.47	-11.412	-4.389	[11:13],15,18,21,23	CBET 1746, CBET 1765, 17, 8
2010id	2455455.83	-5.01	-1.087	4,16	CBET 2467, ATel 2862, 18, 18
2012aw	2456003.36	-1.591	-0.011	[2:15],24,29,40	CBET 3054, ATel 3996, 19
2013am	2456373.138	-1.44	0.0	2,12,16,23,29	CBET 3440, 20, 21, 20
2013by ^a	2456406.042	-3.17	-2.29	4,36	CBET 3506, 22
2013ej	2456498.95	-1.91	-1.325	4,[7:21],23,25,26,28,35,37,39	CBET 3606, ATel 5237, CF ^b , 23,24,25,26
2013fs	2456572.96	-2.14	-1.223	[2:4],6,11,18,20,22,27,29,31,32,39	CBET 3671, 27, 24, 27
2013hj	2456638.8	-3.1	0.0	9,19	CBET 3757, 24
2014G	2456672.074	-3.724	-0.963	3,4,10,14,17,26,37,39	CBET 3787, 28
LSQ14gv	2456674.8	-4.1	0.0	8	PESSTO SDDR2, 29
2014cy	2456900.5	-1.7	0.0	10	CBET 3964, 29, 24

Column 1: SN names. Column 2: discovery epochs. Column 3 and 4: last non-detection and first detection epochs, respectively, with respect to the discovery epoch. Column 5: spectra phase values with respect to the explosion epoch, which we assume as the midpoint between the last non-detection and the first detection. Adjacent ages are listed in brackets. Column 6: references for data.

^a Explosion time constraint obtained through polynomial fit to pre-maximum *VRI* photometry.

^b C. Feliciano report on the *Bright Supernova* website (<http://www.rochesterastromy.org/snimages/>)

^c (1) Gutiérrez et al. (2017); (2) Schmidt et al. (1993); (3) Pastorello et al. (2004); (4) Elmhamdi et al. (2003); (5) Faran et al. (2014b); (6) Shivvers et al. (2017); (7) Faran et al. (2014a); (8) Hicken et al. (2017); (9) Harutyunyan et al. (2008); (10) Spiro et al. (2014); (11) Sahu et al. (2006); (12) Gal-Yam et al. (2008); (13) Pastorello et al. (2009); (14) Pastorello et al. (2006); (15) Quimby et al. (2007); (16) Sako et al. (2018); (17) Inserra et al. (2013); (18) Gal-Yam et al. (2011); (19) Dall’Ora et al. (2014); (20) Tomasella et al. (2018); (21) Zhang et al. (2014); (22) Valenti et al. (2015); (23) Valenti et al. (2014); (24) Childress et al. (2016); (25) Dhungana et al. (2016); (26) Yuan et al. (2016); (27) Yaron et al. (2017); (28) Terreran et al. (2016); (29) Valenti et al. (2016).

Table 5.11: SNID templates.

JD	<i>B</i> (mag)	<i>V</i> (mag)	<i>u</i> (mag)	<i>g</i> (mag)	<i>r</i> (mag)	<i>i</i> (mag)	<i>Y</i> (mag)	<i>J</i> (mag)	<i>H</i> (mag)
2454558.73	17.947(10)	17.762(10)	18.552(24)	17.701(09)	17.536(08)	17.579(12)
2454559.84	17.257(15)	17.125(21)	17.096(59)
2454560.75	18.025(11)	17.763(09)	18.759(32)	17.757(08)	17.584(08)	17.602(09)
2454562.72	18.085(11)	17.828(09)	18.783(29)	17.815(08)	17.618(08)	17.628(11)
2454564.75	18.122(11)	17.890(09)	17.657(07)
2454569.82	18.373(15)	17.928(10)	17.743(08)	17.726(18)
2454570.69	18.395(13)	17.951(09)	19.440(43)	18.080(09)	17.772(08)	17.776(10)
2454572.74	18.442(18)	17.956(15)	19.392(80)	18.156(17)	17.820(11)	17.790(13)
2454573.70	18.530(21)	17.960(16)	19.774(114)	18.175(15)	17.798(11)	17.816(14)
2454574.69	18.575(28)	17.993(17)	19.721(145)	18.196(17)	17.860(12)	17.820(15)
2454575.72	18.631(29)	17.993(21)	19.575(138)	18.232(22)	17.877(14)	17.890(17)
2454578.79	18.890(68)	18.066(31)
2454583.71	18.995(20)	18.297(10)	20.447(73)	18.540(10)	18.039(09)	17.997(10)
2454588.76	17.749(26)	17.515(35)	...
2454589.71	19.286(17)	18.549(12)	20.938(152)	18.793(10)	18.217(09)	18.127(11)
2454592.73	19.408(19)	18.612(12)	21.229(156)	18.934(12)	18.285(10)	18.186(16)
2454593.78	17.786(24)	17.658(42)	...
2454602.68	18.004(16)	17.704(17)	17.637(43)
2454606.66	...	18.969(35)	...	19.489(42)	18.597(19)	18.519(16)
2454616.58	20.806(50)	19.642(21)	...	20.150(23)	19.113(15)	18.981(19)
2454626.56	21.981(386)	22.278(184)	21.729(112)	21.712(168)
2454628.61	...	22.209(403)	...	22.530(441)	21.984(237)	22.445(476)
2454646.56	23.595(407)	23.018(298)	...	24.199(331)	22.521(141)	22.608(308)
2454654.55	23.375(367)	...	22.371(482)	23.445(331)

Errors, in parenthesis and in units of 0.001 mag, are 1σ .

Table 5.12: CSP photometry of SN 2008bm.

JD	<i>B</i> (mag)	<i>V</i> (mag)	<i>u</i> (mag)	<i>g</i> (mag)	<i>r</i> (mag)	<i>i</i> (mag)	<i>Y</i> (mag)	<i>J</i> (mag)	<i>H</i> (mag)
2454888.71	15.520(05)	15.502(07)	15.392(08)	15.441(06)	15.543(08)	15.681(10)
2454891.84	15.300(12)	15.217(16)	15.113(14)
2454892.82	15.325(13)	15.209(13)	15.104(14)
2454896.80	15.871(07)	15.668(10)	15.847(09)	15.719(08)	15.661(08)	15.717(11)
2454897.84	15.941(08)	15.729(07)	15.935(11)	15.777(08)	15.700(11)	15.746(13)
2454898.76	15.978(06)	15.762(05)	16.003(08)	15.822(05)	15.733(07)	15.776(09)
2454899.80	15.429(21)	15.287(16)	15.128(15)
2454900.74	16.073(07)	15.840(08)	16.126(09)	15.895(07)	15.794(09)	15.809(10)
2454901.77	15.477(18)	15.324(17)	15.140(15)
2454902.71	16.167(07)	15.897(06)	16.238(09)	15.983(05)	15.842(07)	15.846(08)
2454907.87	15.503(13)	15.335(11)	15.163(13)
2454908.73	16.371(06)	16.066(07)	16.556(08)	16.161(07)	15.972(09)	15.944(09)
2454911.80	16.469(09)	16.125(14)	16.724(11)	16.236(12)	16.021(18)	15.985(19)
2454913.86	15.548(21)	15.348(16)	15.151(15)
2454914.74	16.563(07)	16.185(08)	16.883(09)	16.319(05)	16.062(12)	16.012(09)
2454915.76	16.598(07)	16.221(08)	16.934(09)	16.357(07)	16.091(06)	16.049(10)
2454917.90	16.661(09)	16.246(09)	17.071(10)	16.400(05)	16.127(09)	16.061(09)
2454920.78	16.760(07)	16.302(08)	17.263(11)	16.476(08)	16.171(08)
2454921.87	15.602(20)	15.380(19)	15.160(14)
2454927.72	16.951(09)	16.425(08)	17.672(15)	16.632(08)	16.259(12)	16.163(14)
2454928.74	16.980(09)	16.442(08)	17.707(16)	16.643(06)	16.267(08)	16.180(10)
2454929.80	15.658(16)	15.438(17)	15.218(14)
2454930.69	17.018(11)	16.463(10)	17.802(17)	16.686(08)	16.293(09)	16.195(09)
2454931.76	17.030(10)	16.484(08)	17.873(32)	16.709(08)	16.306(07)	16.213(10)
2454932.79	15.655(20)	15.434(19)	15.222(17)
2454933.69	17.089(09)	16.508(06)	17.961(20)	16.729(05)	16.321(07)	16.230(06)
2454937.75	17.170(10)	16.551(10)	18.129(16)	16.794(09)	16.353(13)	16.251(09)
2454938.72	15.728(07)	15.492(10)	15.255(09)
2454938.75	17.174(11)	16.556(11)	18.194(16)	16.803(09)	16.373(20)	16.235(14)
2454939.81	15.676(13)	15.447(13)	15.188(16)
2454946.70	17.335(09)	16.608(09)	18.477(17)	16.891(10)	16.408(10)	16.281(09)
2454947.67	17.344(12)	16.608(13)	18.550(20)	16.926(16)	16.405(22)	16.262(20)
2454948.77	15.728(30)	15.483(18)	15.221(15)
2454949.75	15.705(26)	15.476(18)	15.241(17)
2454956.76	15.772(06)	15.518(06)	15.256(08)
2454959.61	15.768(06)	15.517(06)	15.285(08)
2454960.79	17.551(16)	16.717(09)	18.995(76)	17.080(10)	16.471(06)	16.364(09)
2454963.65	17.580(12)	16.745(09)	19.164(82)	17.091(08)	16.489(07)	16.357(10)
2454964.63	17.615(11)	16.745(11)	19.141(36)	17.108(07)	16.493(06)	16.368(08)
2454966.63	17.647(11)	16.766(09)	19.244(28)	17.130(08)	16.511(11)	16.377(10)
2454968.64	17.701(12)	16.777(09)	19.305(29)	17.141(08)	16.527(09)	16.365(15)

Errors, in parenthesis and in units of 0.001 mag, are 1σ .

Table 5.13: CSP photometry of SN 2009aj.

JD	<i>U</i> (mag)	<i>B</i> (mag)	<i>V</i> (mag)	<i>R</i> (mag)	<i>I</i> (mag)	<i>g</i> (mag)	<i>r</i> (mag)	<i>i</i> (mag)	<i>z</i> (mag)
2454890.81	...	15.571(18)	15.503(16)	15.420(16)	15.306(18)	15.509(16)	15.559(15)	15.661(16)	15.770(28)
2454891.72	14.916(19)	15.653(19)	15.522(17)	15.415(16)	15.317(17)	15.545(14)	15.578(14)	15.679(16)	15.772(18)
2454892.71	14.919(21)	15.678(17)	15.585(14)
2454894.71	15.123(19)	15.848(13)	15.650(16)	15.491(16)	15.397(13)	15.715(13)	15.677(14)	15.751(14)	15.851(19)
2454895.71	...	15.867(19)	15.720(14)	15.567(15)	15.406(14)	...	15.699(16)	15.772(14)	15.884(18)
2454896.71	15.193(19)	15.935(15)	15.752(19)	15.575(15)	15.431(14)	15.805(15)	15.755(14)	15.815(13)	15.893(22)
2454899.70	15.426(22)	16.117(17)	15.881(17)	15.705(17)	15.516(15)	15.974(15)	15.878(15)	15.884(14)	15.962(21)
2454900.70	15.863(25)	15.718(18)	15.523(24)
2454903.69	15.676(30)	16.254(19)	16.027(18)	15.780(16)	15.568(15)	16.143(18)	15.972(16)	15.956(14)	16.014(22)
2454905.68	16.194(17)	16.047(15)	16.010(15)	16.044(30)
2454906.68	15.792(27)	16.404(23)	16.065(20)	15.824(19)	15.644(15)	16.216(15)	16.042(16)	16.022(15)	16.050(25)
2454908.68	15.925(32)	16.409(18)	16.132(22)	15.878(17)	15.629(15)	16.274(15)	16.063(17)	16.026(15)	16.026(19)
2454910.67	15.989(35)	16.477(28)	16.175(17)	15.903(19)	15.672(16)	16.335(17)	16.106(14)	16.075(15)	16.096(22)
2454913.66	16.215(30)	16.668(22)	16.243(18)	15.966(19)	15.706(18)	16.413(16)	16.154(14)	16.095(16)	16.079(20)
2454915.65	16.261(33)	16.707(20)	16.282(16)	15.994(16)	15.726(16)	16.478(16)	16.192(13)	16.127(14)	16.132(22)
2454917.69	16.277(38)	16.719(28)	16.307(17)	16.019(19)	15.753(19)	16.502(18)	16.233(15)	16.170(16)	16.132(20)
2454918.72	16.339(37)	16.791(19)	16.299(18)	16.049(17)	15.755(18)	16.520(16)	16.245(15)	16.169(14)	16.119(20)
2454920.68	16.446(39)	16.880(35)	16.380(19)	16.079(20)	15.775(20)	16.563(18)	16.260(15)	16.198(15)	16.139(22)
2454921.68	...	16.878(31)	16.413(19)	16.066(17)	15.808(18)	...	16.282(15)	16.200(16)	16.187(22)
2454922.74	16.652(41)	16.879(29)	16.404(20)	16.099(19)	15.812(21)	16.633(16)	16.297(15)	16.220(16)	16.206(26)
2454924.67	16.441(18)	16.132(18)	15.829(17)	...	16.311(14)	16.240(15)	16.220(21)
2454928.65	16.876(35)	17.026(31)	16.527(19)	16.172(17)	15.838(18)	16.763(19)	16.367(16)	16.281(16)	16.270(24)
2454930.65	17.050(46)	17.050(24)	16.528(19)	16.203(18)	15.899(18)	16.756(18)	16.400(16)	16.297(16)	16.255(26)
2454933.63	17.034(45)	17.101(25)	16.865(19)
2454934.66	16.579(20)	16.212(19)	15.889(16)	...	16.420(16)	16.321(16)	16.288(25)
2454935.63	17.227(68)	17.203(26)	16.619(18)	16.227(17)	15.899(16)	16.858(16)	16.434(15)	16.322(16)	16.302(28)
2454940.70	17.276(73)	17.285(46)	16.638(22)	16.268(16)	15.929(17)	16.950(27)	16.468(16)	16.346(17)	16.274(26)
2454942.63	17.371(50)	17.377(46)	16.618(24)	16.279(24)	15.917(19)	16.958(25)	16.472(19)	16.354(19)	16.310(25)
2454948.63	17.607(61)	17.478(35)	16.667(26)	16.314(19)	15.954(17)	17.003(22)	16.517(14)	16.389(16)	16.302(20)
2454952.60	17.648(78)	17.511(35)	16.705(20)	16.333(19)	15.963(17)	17.037(17)	16.515(15)	16.392(15)	16.360(27)
2454956.60	17.804(79)	17.539(34)	16.731(20)	16.321(16)	15.987(17)	17.118(18)	16.539(15)	16.430(17)	16.385(30)
2454964.61	18.007(105)	17.619(45)	16.778(21)	16.394(17)	16.035(17)	17.175(20)	16.593(14)	16.448(16)	16.405(27)
2454970.60	18.533(115)	17.668(35)	17.288(20)
2454971.66	16.834(26)	16.478(19)	16.070(22)	...	16.619(18)	16.541(25)	16.414(35)
2454983.66	...	17.917(50)	17.451(23)
2454985.62	17.089(22)	16.583(26)	16.145(20)	...	16.793(20)	16.627(22)	16.550(43)
2454989.65	17.127(36)	16.660(30)	16.270(25)	...	16.878(24)	16.665(21)	16.597(40)
2454993.58	17.203(30)	16.725(21)	16.308(21)	...	16.938(17)	16.783(18)	16.642(25)
2454994.51	...	18.321(46)	17.721(24)
2454998.58	...	18.602(89)	17.293(26)	16.834(26)	16.422(29)	17.923(41)	17.044(29)	16.875(21)	16.824(46)
2455028.49	...	>21.017(357)	>20.792(174)
2455039.51	19.835(146)	19.736(118)	19.327(209)
2455053.53	>20.232(251)	...	>19.440(270)	20.590(503)	20.302(273)
2455054.51	19.989(171)	20.087(123)

Errors, in parenthesis and in units of 0.001 mag, are 1σ .

Table 5.14: CHASE photometry of SN 2009aj.

JD	<i>B</i> (mag)	<i>V</i> (mag)	<i>u</i> (mag)	<i>g</i> (mag)	<i>r</i> (mag)	<i>i</i> (mag)	<i>Y</i> (mag)	<i>J</i> (mag)	<i>H</i> (mag)
2454907.82	16.950(16)	16.846(18)	16.632(39)
2454908.70	17.175(10)	17.068(10)	17.185(11)	17.081(08)	17.066(10)	17.173(12)
2454911.77	17.234(10)	...	17.299(12)	17.086(09)	17.041(13)	17.080(14)
2454913.80	16.747(13)	16.700(19)	16.544(34)
2454914.71	17.344(08)	17.092(09)	...	17.153(09)	17.066(11)	17.116(15)
2454915.73	17.377(07)	17.104(09)	17.513(14)	17.191(07)	17.073(09)	17.114(14)
2454917.82	17.455(10)	17.157(12)	17.686(15)	17.253(09)	17.094(11)	17.130(14)
2454920.75	17.575(10)	17.211(08)	17.916(14)	17.322(10)	17.132(11)	17.100(12)
2454921.82	16.704(16)	16.713(31)	16.422(38)
2454927.68	17.906(12)	17.398(11)	18.504(25)	17.599(09)	17.279(09)	17.198(11)
2454928.71	17.943(15)	17.410(10)	18.549(29)	17.647(11)	17.295(10)	17.222(10)
2454929.75	16.792(13)	16.637(18)	16.383(24)
2454930.65	18.006(20)	17.525(16)	18.814(44)	17.719(14)	17.365(12)	17.313(16)
2454931.73	18.123(25)	17.513(17)	18.883(55)	17.736(16)	17.376(15)	17.284(16)
2454932.74	16.792(17)	16.651(18)	16.404(29)
2454933.66	18.224(19)	17.592(14)	19.141(49)	17.856(11)	17.411(10)	17.316(13)
2454937.70	18.466(12)	17.725(10)	19.563(33)	18.027(10)	17.549(11)	17.422(12)
2454938.71	18.518(16)	17.735(11)	19.607(38)	18.074(12)	17.564(14)	17.405(17)
2454942.63	18.760(15)	17.876(13)	20.005(45)	18.274(11)	17.650(10)	17.550(11)
2454945.77	17.058(19)	16.782(18)	16.644(30)
2454946.67	18.987(17)	18.008(14)	20.362(50)	18.447(13)	17.778(12)	17.628(14)
2454947.63	19.003(19)	...	20.575(47)	18.468(16)	17.806(16)	17.686(18)
2454948.71	17.088(17)	16.941(21)	16.391(47)
2454949.70	17.169(21)	17.041(27)	16.605(31)
2454959.62	19.590(91)	18.433(51)	...	18.862(54)	18.111(22)	17.900(26)
2454959.66	17.343(16)	17.081(11)	16.901(11)
2454963.61	19.734(35)	18.526(21)	...	19.064(28)	18.169(13)	18.043(19)
2454964.60	19.840(38)	18.553(20)	...	19.096(19)	18.198(15)	18.037(17)
2454966.60	19.916(31)	18.586(16)	...	19.172(18)	18.251(14)	18.030(17)
2454967.65	17.483(21)	17.145(24)	16.722(39)
2454968.60	...	18.657(20)	...	19.208(19)	18.242(18)	18.028(20)

Errors, in parenthesis and in units of 0.001 mag, are 1σ .

Table 5.15: CSP photometry of SN 2009au.

JD	<i>B</i> (mag)	<i>V</i> (mag)	<i>R</i> (mag)	<i>I</i> (mag)	<i>g</i> (mag)	<i>r</i> (mag)	<i>i</i> (mag)	<i>z</i> (mag)
2454916.65	17.444(26)	17.244(24)	17.052(21)	16.835(36)	17.323(25)	17.206(23)	17.232(30)	17.260(45)
2454917.64	17.490(28)	17.285(23)	17.064(21)	16.845(28)	17.329(24)	17.237(22)	17.200(25)	17.257(40)
2454918.68	17.508(33)	17.288(23)	17.090(24)	16.853(26)	17.340(25)	17.233(18)	17.218(26)	17.251(42)
2454919.70	17.537(25)	17.304(24)	17.105(25)	16.865(34)	17.349(21)	17.230(24)	17.265(25)	17.256(36)
2454921.64	17.594(48)	17.340(25)	17.129(22)	16.872(30)	17.394(26)	17.267(21)	17.248(23)	17.267(45)
2454923.68	17.671(28)	17.375(26)	17.153(26)	16.875(38)	17.507(23)	17.303(23)	17.232(33)	17.256(42)
2454925.70	17.809(38)	17.429(49)	17.202(27)	...	17.588(33)
2454926.69	16.904(50)	17.323(73)
2454927.69	17.373(67)	17.272(56)	...
2454928.61	17.930(28)	17.499(28)	17.250(25)	16.907(35)	17.731(25)	17.412(23)	17.308(28)	17.285(44)
2454931.60	18.174(64)	17.612(56)	17.278(40)	16.927(51)	17.811(50)	17.488(38)	17.406(43)	17.380(76)
2454934.60	18.284(34)	17.710(26)	17.367(27)	17.058(40)	17.944(26)	17.611(23)	17.430(28)	17.442(57)
2454936.58	18.433(37)	17.757(30)	17.495(28)	17.106(38)	18.062(27)	17.641(22)	17.422(31)	17.408(50)
2454939.68	18.549(51)	17.866(33)	17.538(27)	17.186(36)	18.212(31)	17.711(23)	17.544(28)	17.455(40)
2454944.63	18.761(59)	18.030(43)	17.672(35)	17.317(37)	18.471(33)	17.826(27)	17.704(33)	17.585(50)
2454949.58	18.939(59)	18.173(46)	17.770(29)	17.433(43)	18.649(44)	17.971(25)	17.839(38)	17.735(45)
2454953.57	19.196(67)	18.704(41)	18.025(71)
2454954.55	...	18.284(40)	17.981(34)	17.563(45)	17.911(40)	...
2454960.61	19.529(207)	18.494(99)	18.060(64)	17.637(79)	18.977(95)	18.232(51)	18.089(70)	18.078(120)
2454971.63	...	18.812(105)	18.251(48)	17.827(75)	...	18.497(82)	18.258(72)	18.133(167)
2454974.53	...	18.870(68)	18.354(42)	17.828(46)
2454974.54	19.817(107)	19.357(73)
2454983.60	20.140(154)	19.613(82)
2454984.54	...	19.194(74)	18.546(212)	17.984(152)
2454985.54	...	19.227(123)	18.581(91)	18.046(93)
2454991.54	...	19.326(83)	18.682(52)	18.125(64)	...	18.834(40)	18.569(51)	18.226(80)
2454998.52	20.112(69)
2455037.53	>21.339(275)
2455038.55	...	>21.083(267)	20.216(144)
2455039.52	>19.501(185)

Errors, in parenthesis and in units of 0.001 mag, are 1σ .

Table 5.16: CHASE photometry of SN 2009au.

Bibliography

- Akaike, H. (1974). “A New Look at the Statistical Model Identification”. *IEEE Trans. Autom. Control* 19, 716–723.
- Akaike, H. (1978). “On the Likelihood of a Time Series Model”. *J. Royal Stat. Soc. Series D* 27.3/4, 217–235.
- Anand, G. S. et al. (2018). “A Robust Tip of the Red Giant Branch Distance to the Fireworks Galaxy (NGC 6946)”. *AJ* 156, 105.
- Anderson, J. P. et al. (2014a). “Analysis of blueshifted emission peaks in Type II supernovae”. *MNRAS* 441, 671–680.
- Anderson, J. P. et al. (2014b). “Characterizing the V-band Light-curves of Hydrogen-rich Type II Supernovae”. *ApJ* 786, 67.
- Anderson, J. P. et al. (2016). “Type II supernovae as probes of environment metallicity: observations of host H II regions”. *A&A* 589, A110.
- Baltay, C. et al. (2013). “The La Silla-QUEST Low Redshift Supernova Survey”. *PASP* 125, 683.
- Barbarino, C. et al. (2015). “SN 2012ec: mass of the progenitor from PESSTO follow-up of the photospheric phase”. *MNRAS* 448, 2312–2331.
- Baron, E. et al. (1995). “Non-LTE Spectral Analysis and Model Constraints on SN 1993J”. *ApJ* 441, 170.
- Bartel, N. “Angular Diameter Determinations of Radio Supernovae and the Distance Scale”. *Supernovae as Distance Indicators, Proceedings of the Workshop, held in Cambridge, MA, September 27, 28, 1984. Lecture Notes in Physics, Vol. 224, edited by Norbert Bartel. Springer-Verlag, Berlin, 1985., p.107.*
- Blinnikov, S. I. et al. (1998). “A Comparative Modeling of Supernova 1993J”. *ApJ* 496.1, 454–472.
- Blinnikov, S. I. et al. (2000). “Radiation Hydrodynamics of SN 1987A. I. Global Analysis of the Light Curve for the First 4 Months”. *ApJ* 532.2, 1132–1149.
- Blinnikov, S. I. et al. (2006). “Theoretical light curves for deflagration models of type Ia supernova”. *A&A* 453.1, 229–240.

- Blondin, S. and Tonry, J. L. (2007). “Determining the Type, Redshift, and Age of a Supernova Spectrum”. *ApJ* 666, 1024–1047.
- Bohlin, R. C. and Gilliland, R. L. (2004). “Hubble Space Telescope Absolute Spectrophotometry of Vega from the Far-Ultraviolet to the Infrared”. *AJ* 127, 3508–3515.
- Bose, S. and Kumar, B. (2014). “Distance Determination to Eight Galaxies Using Expanding Photosphere Method”. *ApJ* 782, 98.
- Bose, S. et al. (2013). “Supernova 2012aw - a high-energy clone of archetypal Type IIP SN 1999em”. *MNRAS* 433, 1871–1891.
- Bose, S. et al. (2015). “SN 2013ej: A Type IIL Supernova with Weak Signs of Interaction”. *ApJ* 806, 160.
- Bose, S. et al. (2016). “Photometric and polarimetric observations of fast declining Type II supernovae 2013hj and 2014G”. *MNRAS* 455, 2712–2730.
- Bostroem, K. Azalee et al. (2019). “Signatures of Circumstellar Interaction in the Type IIL Supernova ASASSN-15oz”. *MNRAS*, 562.
- Branch, D. et al. (1981). “The type II SN 1979c in M 100 and the distance to the Virgo cluster.” *ApJ* 244, 780–804.
- Brown, P. J. et al. (2010). “The Absolute Magnitudes of Type Ia Supernovae in the Ultraviolet”. *ApJ* 721, 1608–1626.
- Bullivant, C. et al. (2018). “SN 2013fs and SN 2013fr: exploring the circumstellar-material diversity in Type II supernovae”. *MNRAS* 476, 1497–1518.
- Burnham, K. P. and Anderson, D. R. (2002). “Model Selection and Multimodel Inference”. *Model Selection and Multimodel Inference*. 2nd. New York: Springer-Verlag.
- Buta, R. J. (1982). “Photometric observations of the bright type II supernova 1980k in NGC 6946.” *PASP* 94, 578–585.
- Cardelli, J. A. et al. (1989). “The relationship between infrared, optical, and ultraviolet extinction”. *ApJ* 345, 245–256.
- Chambers, K. C. et al. (2016). “The Pan-STARRS1 Surveys”, arXiv:1612.05560.
- Childress, M. J. et al. (2016). “The ANU WiFeS SuperNovA Programme (AWSNAP)”. *PASA* 33, e055.
- Cleveland, W. S. et al. (1992). “Local Regression Models”. *Statistical models in S*. Ed. by J. M. Chambers and T. J. Hastie. London: Chapman and Hall. Chap. 8, 309–376.
- Cohen, M. et al. (1999). “Spectral Irradiance Calibration in the Infrared. X. A Self-Consistent Radiometric All-Sky Network of Absolutely Calibrated Stellar Spectra”. *AJ* 117, 1864–1889.
- Contreras, C. et al. (2010). “The Carnegie Supernova Project: First Photometry Data Release of Low-Redshift Type Ia Supernovae”. *AJ* 139, 519–539.

- Crook, A. C. et al. (2007). “Groups of Galaxies in the Two Micron All Sky Redshift Survey”. *ApJ* 655, 790–813.
- D’Andrea, C. B. et al. (2010). “Type II-P Supernovae from the SDSS-II Supernova Survey and the Standardized Candle Method”. *ApJ* 708, 661–674.
- Dall’Ora, M. et al. (2014). “The Type IIP Supernova 2012aw in M95: Hydrodynamical Modeling of the Photospheric Phase from Accurate Spectrophotometric Monitoring”. *ApJ* 787, 139.
- Das, K. R. and Imon, A. H. M. R. (2016). “A Brief Review of Tests for Normality”. *Am. J. Theor. Appl. Stat.* 5.1, 5–12.
- Dessart, L. and Hillier, D. J. (2005). “Quantitative spectroscopy of photospheric-phase type II supernovae”. *A&A* 437, 667–685.
- Dessart, L. et al. (2008). “Using Quantitative Spectroscopic Analysis to Determine the Properties and Distances of Type II Plateau Supernovae: SN 2005cs and SN 2006bp”. *ApJ* 675, 644–669.
- Dessart, L. et al. (2013). “Type II-Plateau supernova radiation: dependences on progenitor and explosion properties”. *MNRAS* 433, 1745–1763.
- Dessart, L. et al. (2014). “Type II Plateau supernovae as metallicity probes of the Universe”. *MNRAS* 440, 1856–1864.
- Dhungana, G. et al. (2016). “Extensive Spectroscopy and Photometry of the Type IIP Supernova 2013ej”. *ApJ* 822, 6.
- Djorgovski, S. and Davis, M. (1987). “Fundamental Properties of Elliptical Galaxies”. *ApJ* 313, 59.
- Doane, D. and Seward, L. (2016). *Applied Statistics in Business and Economics*. 5th. New York: McGraw-Hill. ISBN: 9781259255885 1259255883 9780077175115 0077175115.
- Drake, A. J. et al. (2008). “Supernova 2008bm”. *CBET* 1320.
- Dwek, E. et al. (1983). “The evolution of the infrared emission from the type II supernova 1980k in NGC 6946 : The dust formation model.” *ApJ* 274, 168–174.
- Eastman, R. G. and Kirshner, R. P. (1989). “Model atmospheres for SN 1987A and the distance to the Large Magellanic Cloud”. *ApJ* 347, 771–793.
- Eastman, R. G. et al. (1996). “The Atmospheres of Type II Supernovae and the Expanding Photosphere Method”. *ApJ* 466, 911.
- Elmhamdi, A. et al. (2003). “Photometry and spectroscopy of the Type IIP SN 1999em from outburst to dust formation”. *MNRAS* 338, 939–956.
- Faran, T. et al. (2014a). “A sample of Type II-L supernovae”. *MNRAS* 445, 554–569.
- Faran, T. et al. (2014b). “Photometric and spectroscopic properties of Type II-P supernovae”. *MNRAS* 442, 844–861.
- Fassia, A. et al. (2000). “Optical and infrared photometry of the Type II In SN 1998S: days 11-146”. *MNRAS* 318, 1093–1104.

- Fassia, A. et al. (2001). “Optical and infrared spectroscopy of the type II_n SN 1998S: days 3-127”. *MNRAS* 325, 907–930.
- Filippenko, A. V. (1982). “The importance of atmospheric differential refraction in spectrophotometry”. *PASP* 94, 715–721.
- Filippenko, A. V. (1988). “Supernova 1987K: Type II in Youth, Type Ib in Old Age”. *AJ* 96, 1941.
- Fitzpatrick, E. L. (1999). “Correcting for the Effects of Interstellar Extinction”. *PASP* 111, 63–75.
- Fixsen, D. J. et al. (1996). “The Cosmic Microwave Background Spectrum from the Full COBE FIRAS Data Set”. *ApJ* 473, 576.
- Flewelling, H. A. et al. (2016). “The Pan-STARRS1 Database and Data Products”, arXiv:1612.05243.
- Fransson, C. et al. (2014). “High-density Circumstellar Interaction in the Luminous Type II_n SN 2010jl: The First 1100 Days”. *ApJ* 797.2, 118.
- Fraser, M. et al. (2011). “SN 2009md: another faint supernova from a low-mass progenitor”. *MNRAS* 417, 1417–1433.
- Fukugita, M. et al. (1996). “The Sloan Digital Sky Survey Photometric System”. *AJ* 111, 1748.
- Gal-Yam, A. et al. (2008). “GALEX Spectroscopy of SN 2005ay Suggests Ultraviolet Spectral Uniformity among Type II-P Supernovae”. *ApJ* 685, L117.
- Gal-Yam, A. et al. (2011). “Real-time Detection and Rapid Multiwavelength Follow-up Observations of a Highly Subluminous Type II-P Supernova from the Palomar Transient Factory Survey”. *ApJ* 736, 159.
- Galbany, L. et al. (2016). “UBVR_Iz Light Curves of 51 Type II Supernovae”. *AJ* 151, 33.
- Gall, E. E. E. et al. (2015). “A comparative study of Type II-P and II-L supernova rise times as exemplified by the case of LSQ13cuw”. *A&A* 582, A3.
- Gall, E. E. E. et al. (2016). “Applying the expanding photosphere and standardized candle methods to Type II-Plateau supernovae at cosmologically significant redshifts . The distance to SN 2013eq”. *A&A* 592, A129.
- Gall, E. E. E. et al. (2018). “An updated Type II supernova Hubble diagram”. *A&A* 611, A25.
- González-Gaitán, S. et al. (2015). “The rise-time of Type II supernovae”. *MNRAS* 451, 2212–2229.
- Gutiérrez, C. P. et al. (2017). “Type II Supernova Spectral Diversity. I. Observations, Sample Characterization, and Spectral Line Evolution”. *ApJ* 850, 89.
- Hamuy, M. A. (2001). “Type II supernovae as distance indicators”. PhD thesis. The University of Arizona.
- Hamuy, M. (2003). “Observed and Physical Properties of Core-Collapse Supernovae”. *ApJ* 582, 905–914.
- Hamuy, M. and Pinto, P. A. (2002). “Type II Supernovae as Standardized Candles”. *ApJ* 566, L63–L65.

- Hamuy, M. et al. (1988). “SN 1987A in the LMC: UBVRI Photometry at Cerro Tololo”. *AJ* 95, 63.
- Hamuy, M. et al. (1996). “The Absolute Luminosities of the Calan/Tololo Type IA Supernovae”. *AJ* 112, 2391.
- Hamuy, M. et al. (2001). “The Distance to SN 1999em from the Expanding Photosphere Method”. *ApJ* 558, 615–642.
- Hamuy, M. et al. (2006). “The Carnegie Supernova Project: The Low-Redshift Survey”. *PASP* 118, 2–20.
- Harutyunyan, A. H. et al. (2008). “ESC supernova spectroscopy of non-ESC targets”. *A&A* 488, 383–399.
- Hatt, D. et al. (2018). “The Carnegie-Chicago Hubble Program. V. The Distances to NGC 1448 and NGC 1316 via the Tip of the Red Giant Branch”. *ApJ* 866, 145.
- Hicken, M. et al. (2017). “Type II Supernova Light Curves and Spectra from the CfA”. *ApJS* 233, 6.
- Hurvich, C. M. et al. (1998). “Smoothing Parameter Selection in Nonparametric Regression Using an Improved Akaike Information Criterion”. *J. Royal Stat. Soc. Series B* 60.2, 271–293.
- Imon, A. H. M. R. (2003). “Regression Residuals, Moments, and Their Use in Tests for Normality”. *Commun. Stat. Theor. Meth.* 32.5, 1021–1034.
- Inserra, C. et al. (2012). “The bright Type IIP SN 2009bw, showing signs of interaction”. *MNRAS* 422.2, 1122–1139.
- Inserra, C. et al. (2013). “Moderately luminous Type II supernovae”. *A&A* 555, A142.
- Jang, I. S. and Lee, M. G. (2017a). “The Tip of the Red Giant Branch Distances to Type Ia Supernova Host Galaxies. V. NGC 3021, NGC 3370, and NGC 1309 and the Value of the Hubble Constant”. *ApJ* 836, 74.
- Jang, I. S. and Lee, M. G. (2017b). “The Tip of the Red Giant Branch Distances to Type Ia Supernova Host Galaxies. IV. Color Dependence and Zero-point Calibration”. *ApJ* 835, 28.
- Jarque, C. M. and Bera, A. K. (1987). “A Test for Normality of Observations and Regression Residuals”. *Int. Stat. Rev.* 55.2, 163–172.
- Jones, M. I. et al. (2009). “Distance Determination to 12 Type II Supernovae Using the Expanding Photosphere Method”. *ApJ* 696, 1176–1194.
- Kasen, D. and Woosley, S. E. (2009). “Type II Supernovae: Model Light Curves and Standard Candle Relationships”. *ApJ* 703, 2205–2216.
- Kirshner, R. P. and Kwan, J. (1974). “Distances to extragalactic supernovae”. *ApJ* 193, 27–36.
- Krisciunas, K. et al. (2003). “Optical and Infrared Photometry of the Nearby Type Ia Supernova 2001el”. *AJ* 125.1, 166–180.
- Krisciunas, K. et al. (2009). “Do the Photometric Colors of Type II-P Supernovae Allow Accurate Determination of Host Galaxy Extinction?” *AJ* 137, 34–41.

- Kuncarayakti, H. et al. (2018). “Constraints on core-collapse supernova progenitors from explosion site integral field spectroscopy”. *A&A* 613, A35.
- Landolt, A. U. (1992). “UBVRI Photometric Standard Stars in the Magnitude Range 11.5 < V < 16.0 Around the Celestial Equator”. *AJ* 104, 340.
- Leloudas, G. et al. (2015). “Supernova spectra below strong circumstellar interaction”. *A&A* 574, A61.
- Leonard, D. C. et al. (2002). “The Distance to SN 1999em in NGC 1637 from the Expanding Photosphere Method”. *PASP* 114, 35–64.
- Li, W. et al. (2011). “Nearby supernova rates from the Lick Observatory Supernova Search - II. The observed luminosity functions and fractions of supernovae in a complete sample”. *MNRAS* 412, 1441–1472.
- Liddle, A. R. (2007). “Information criteria for astrophysical model selection”. *MNRAS* 377, L74–L78.
- Lisakov, S. M. et al. (2018). “Progenitors of low-luminosity Type II-Plateau supernovae”. *MNRAS* 473.3, 3863–3881.
- Maguire, K. et al. (2010a). “Optical and near-infrared coverage of SN 2004et: physical parameters and comparison with other Type IIP supernovae”. *MNRAS* 404, 981–1004.
- Maguire, K. et al. (2010b). “Type II-P supernovae as standardized candles: improvements using near-infrared data”. *MNRAS* 403, L11–L15.
- Marino, R. A. et al. (2013). “The O3N2 and N2 abundance indicators revisited: improved calibrations based on CALIFA and T_e -based literature data”. *A&A* 559, A114.
- McQuinn, K. B. W. et al. (2017). “Accurate Distances to Important Spiral Galaxies: M63, M74, NGC 1291, NGC 4559, NGC 4625, and NGC 5398”. *AJ* 154, 51.
- Minkowski, R. (1941). “Spectra of Supernovae”. *PASP* 53, 224.
- Misra, K. et al. (2007). “Type IIP supernova SN 2004et: a multiwavelength study in X-ray, optical and radio”. *MNRAS* 381, 280–292.
- Moriya, T. J. et al. (2017). “Immediate dense circumstellar environment of supernova progenitors caused by wind acceleration: its effect on supernova light curves”. *MNRAS* 469.1, L108–L112.
- Moriya, T. J. et al. (2018). “Type IIP supernova light curves affected by the acceleration of red supergiant winds”. *MNRAS* 476.2, 2840–2851.
- Munari, U. and Carraro, G. (1996). “On linear fit to ZAMS and reddening determination.” *A&A* 314, 108–111.
- Murphy, J. W. et al. (2018). “The Progenitor Age and Mass of the Black Hole Formation Candidate N6946-BH1”. *ApJ* 860, 117.
- Natali, F. et al. (1994). “The use of the (B-I) color index and applications of the (B-I) versus (B-V) relationship”. *A&A* 289, 756–762.

- Niemela, V. S. et al. (1985). “The supernova 1983k in NGC 4699 - Clues to the nature of Type II progenitors”. *ApJ* 289, 52–57.
- Nugent, P. et al. (2006). “Toward a Cosmological Hubble Diagram for Type II-P Supernovae”. *ApJ* 645, 841–850.
- Olivares E., F. et al. (2010). “The Standardized Candle Method for Type II Plateau Supernovae”. *ApJ* 715, 833–853.
- Olivares, F. (2008). “The Standard Candle Method for Type II-Plateau Supernovae”. MA thesis. Universidad de Chile.
- Pastorello, A. et al. (2004). “Low-luminosity Type II supernovae: spectroscopic and photometric evolution”. *MNRAS* 347, 74–94.
- Pastorello, A. et al. (2006). “SN 2005cs in M51 - I. The first month of evolution of a subluminescent SN II plateau”. *MNRAS* 370, 1752–1762.
- Pastorello, A. et al. (2009). “SN 2005cs in M51 - II. Complete evolution in the optical and the near-infrared”. *MNRAS* 394, 2266–2282.
- Pejcha, O. and Prieto, J. L. (2015). “A Global Model of The Light Curves and Expansion Velocities of Type II-plateau Supernovae”. *ApJ* 799, 215.
- Persson, S. E. et al. (1998). “A New System of Faint Near-Infrared Standard Stars”. *AJ* 116, 2475–2488.
- Pettini, M. and Pagel, B. E. J. (2004). “[OIII]/[NII] as an abundance indicator at high redshift”. *MNRAS* 348.3, L59–L63.
- Phillips, M. M. (1993). “The absolute magnitudes of Type Ia supernovae”. *ApJ* 413, L105–L108.
- Phillips, M. M. et al. (1990). “The Light Curve of the Plateau Type II SN 1983K”. *PASP* 102, 299.
- Phillips, M. M. et al. (2013). “On the Source of the Dust Extinction in Type Ia Supernovae and the Discovery of Anomalously Strong Na I Absorption”. *ApJ* 779.1, 38.
- Pignata, G. et al. (2004). “Photometric observations of the Type Ia SN 2002er in UGC 10743”. *MNRAS* 355.1, 178–190.
- Pignata, G. et al. (2009a). “Supernova 2009aj in ESO 221-18”. *CBET* 1704.
- Pignata, G. et al. (2009b). “Supernova 2009au in ESO 443-21”. *CBET* 1719.
- Pignata, G. et al. (2009c). “The CHilean Automatic Supernova sEarch (CHASE)”. *American Institute of Physics Conference Series*. Ed. by G. Giobbi et al. Vol. 1111. American Institute of Physics Conference Series, 551–554.
- Polshaw, J. et al. (2016). “LSQ13fn: A type II-Plateau supernova with a possibly low metallicity progenitor that breaks the standardised candle relation”. *A&A* 588, A1.
- Poznanski, D. et al. (2009). “Improved Standardization of Type II-P Supernovae: Application to an Expanded Sample”. *ApJ* 694, 1067–1079.

- Poznanski, D. et al. (2012). “An empirical relation between sodium absorption and dust extinction”. *MNRAS* 426, 1465–1474.
- Pozzo, M. et al. (2006). “Optical and infrared observations of the Type IIP SN2002hh from days 3 to 397”. *MNRAS* 368, 1169–1195.
- Quimby, R. M. et al. (2007). “SN 2006bp: Probing the Shock Breakout of a Type II-P Supernova”. *ApJ* 666, 1093–1107.
- Rana, M. S. et al. (2009). “A Robust Rescaled Moment Test for Normality in Regression”. *J. Math. Stat* 5, 54–62.
- Reichart, D. et al. (2005). “PROMPT: Panchromatic Robotic Optical Monitoring and Polarimetry Telescopes”. *Nuovo Cimento C Geophysics Space Physics C* 28.4, 767.
- Riess, A. G. et al. (1996). “A Precise Distance Indicator: Type IA Supernova Multicolor Light-Curve Shapes”. *ApJ* 473, 88.
- Riess, A. G. et al. (2016). “A 2.4% Determination of the Local Value of the Hubble Constant”. *ApJ* 826, 56.
- Rizzi, L. et al. (2007). “Tip of the Red Giant Branch Distances. II. Zero-Point Calibration”. *ApJ* 661, 815–829.
- Rodríguez, Ó. et al. (2014). “Photospheric Magnitude Diagrams for Type II Supernovae: A Promising Tool to Compute Distances”. *AJ* 148, 107.
- Rodríguez, Ó. et al. (2019). “Type II supernovae as distance indicators at near-IR wavelengths”. *MNRAS* 483, 5459–5479.
- Roy, R. et al. (2011). “SN 2008in-Bridging the Gap between Normal and Faint Supernovae of Type IIP”. *ApJ* 736, 76.
- Saha, A. et al. (2006). “Cepheid Distances to SNe Ia Host Galaxies Based on a Revised Photometric Zero Point of the HST WFPC2 and New PL Relations and Metallicity Corrections”. *ApJS* 165, 108–137.
- Sahu, D. K. et al. (2006). “Photometric and spectroscopic evolution of the Type IIP supernova SN 2004et”. *MNRAS* 372, 1315–1324.
- Sako, M. et al. (2018). “The Data Release of the Sloan Digital Sky Survey-II Supernova Survey”. *PASP* 130.6, 064002.
- Sanders, N. E. et al. (2015). “Toward Characterization of the Type IIP Supernova Progenitor Population: A Statistical Sample of Light Curves from Pan-STARRS1”. *ApJ* 799, 208.
- Schlafly, E. F. and Finkbeiner, D. P. (2011). “Measuring Reddening with Sloan Digital Sky Survey Stellar Spectra and Recalibrating SFD”. *ApJ* 737, 103.
- Schlafly, E. F. et al. (2016). “The Optical-infrared Extinction Curve and Its Variation in the Milky Way”. *ApJ* 821, 78.

- Schlegel, D. J. et al. (1998). “Maps of Dust Infrared Emission for Use in Estimation of Reddening and Cosmic Microwave Background Radiation Foregrounds”. *ApJ* 500, 525–553.
- Schlegel, E. M. (1990). “A new subclass of Type II supernovae?” *MNRAS* 244, 269–271.
- Schmidt, B. P. et al. (1992). “Expanding photospheres of type II supernovae and the extragalactic distance scale”. *ApJ* 395, 366–386.
- Schmidt, B. P. et al. (1993). “Photometric and spectroscopic observations of SN 1990E in NGC 1035 - Observational constraints for models of type II supernovae”. *AJ* 105, 2236–2250.
- Schmidt, B. P. et al. (1994). “The distances to five Type II supernovae using the expanding photosphere method, and the value of H_0 ”. *ApJ* 432, 42–48.
- Schwarz, G. (1978). “Estimating the Dimension of a Model”. *Annals of Statistics* 6, 461–464.
- Shapiro, S. S. and Wilk, M. B. (1965). “An Analysis of Variance Test for Normality (Complete Samples)”. *Biometrika* 52.3/4, 591–611.
- Shivvers, I. et al. (2017). “Revisiting the Lick Observatory Supernova Search Volume-limited Sample: Updated Classifications and Revised Stripped-envelope Supernova Fractions”. *PASP* 129.5, 054201.
- Silverman, J. M. et al. (2012). “Berkeley Supernova Ia Program - I. Observations, data reduction and spectroscopic sample of 582 low-redshift Type Ia supernovae”. *MNRAS* 425, 1789–1818.
- Skrutskie, M. F. et al. (2006). “The Two Micron All Sky Survey (2MASS)”. *AJ* 131, 1163–1183.
- Smartt, S. J. et al. (2009). “The death of massive stars - I. Observational constraints on the progenitors of Type II-P supernovae”. *MNRAS* 395, 1409–1437.
- Smartt, S. J. et al. (2015). “PESSTO: survey description and products from the first data release by the Public ESO Spectroscopic Survey of Transient Objects”. *A&A* 579, A40.
- Smith, J. A. et al. (2002). “The u’g’r’i’z’ Standard-Star System”. *AJ* 123, 2121–2144.
- Smith, N. et al. (2011). “Observed fractions of core-collapse supernova types and initial masses of their single and binary progenitor stars”. *MNRAS* 412.3, 1522–1538.
- Sollerman, J. et al. (2005). “Diffuse Interstellar Bands in NGC 1448”. *A&A* 429, 559–567.
- Spiro, S. et al. (2014). “Low luminosity Type II supernovae - II. Pointing towards moderate mass precursors”. *MNRAS* 439, 2873–2892.
- Stritzinger, M. and Morrell, N. (2008). “Supernovae 2008bm, 2008bp, and 2008bq”. *CBET* 1329.
- Stritzinger, M. et al. (2002). “Optical Photometry of the Type Ia Supernova 1999ee and the Type Ib/c Supernova 1999ex in IC 5179”. *AJ* 124, 2100–2117.
- Stritzinger, M. et al. (2009). “Supernovae 2009aj, 2009ao, and 2009au”. *CBET* 1725.
- Sugiura, N. (1978). “Further analysis of the data by akaike’s information criterion and the finite corrections”. *Commun. Stat. Theory Methods* 7.1, 13–26.

- Taddia, F. et al. (2013). “Carnegie Supernova Project: Observations of Type IIn supernovae”. *A&A* 555, A10.
- Takáts, K. and Vinkó, J. (2012). “Measuring expansion velocities in Type II-P supernovae”. *MNRAS* 419, 2783–2796.
- Takáts, K. et al. (2014). “SN 2009N: linking normal and subluminal Type II-P SNe”. *MNRAS* 438, 368–387.
- Takáts, K. et al. (2015). “SN 2009ib: a Type II-P supernova with an unusually long plateau”. *MNRAS* 450, 3137–3154.
- Terreran, G. et al. (2016). “The multifaceted Type II-L supernova 2014G from pre-maximum to nebular phase”. *MNRAS* 462, 137–157.
- Thompson, L. A. (1982). “Upper mass limit for the stellar progenitor to the 1980k supernova in NGC 6946.” *ApJ* 257, L63–L66.
- Tikhonov, N. A. (2014). “Stellar content and distances to the isolated spiral galaxies NGC 6503 and NGC 6946”. *Astronomy Letters* 40, 537–550.
- Tomasella, L. et al. (2013). “Comparison of progenitor mass estimates for the Type IIP SN 2012A”. *MNRAS* 434, 1636–1657.
- Tomasella, L. et al. (2018). “SNe 2013K and 2013am: observed and physical properties of two slow, normal Type IIP events”. *MNRAS* 475, 1937–1959.
- Tonry, J. L. et al. (2000). “The Surface Brightness Fluctuation Survey of Galaxy Distances. II. Local and Large-Scale Flows”. *ApJ* 530, 625–651.
- Tonry, J. and Schneider, D. P. (1988). “A New Technique for Measuring Extragalactic Distances”. *AJ* 96, 807.
- Tukey, J. W. (1977). *Exploratory Data Analysis*. Reading, MA: Addison-Wesley.
- Tully, R. B. and Fisher, J. R. (1977). “A new method of determining distance to galaxies.” *A&A* 500, 105–117.
- Tully, R. B. et al. (2016). “Cosmicflows-3”. *AJ* 152, 50.
- Turatto, M. et al. (2003). “Variety in Supernovae”. *From Twilight to Highlight: The Physics of Supernovae*. Ed. by Wolfgang Hillebrandt and Bruno Leibundgut, 200.
- Valenti, S. et al. (2014). “The first month of evolution of the slow-rising Type IIP SN 2013ej in M74”. *MNRAS* 438, L101–L105.
- Valenti, S. et al. (2015). “Supernova 2013by: a Type IIL supernova with a IIP-like light-curve drop”. *MNRAS* 448, 2608–2616.
- Valenti, S. et al. (2016). “The diversity of Type II supernova versus the similarity in their progenitors”. *MNRAS* 459, 3939–3962.

- Wagoner, R. V. (1981). “Effects of scattering on continuous radiation from supernovae and determination of their distances”. *ApJ* 250, L65–L69.
- Wang, L. et al. (2006). “Nonlinear Decline-Rate Dependence and Intrinsic Variation of Type Ia Supernova Luminosities”. *ApJ* 641, 50–69.
- Woosley, S. E. et al. (1987). “Supernova 1987A in the Large Magellanic Cloud: The Explosion of a approximately 20 M_{sun} Star Which Has Experienced Mass Loss?” *ApJ* 318, 664.
- Yaron, O. et al. (2017). “Confined dense circumstellar material surrounding a regular type II supernova”. *Nature Physics* 13, 510–517.
- Yuan, F. et al. (2016). “450 d of Type II SN 2013ej in optical and near-infrared”. *MNRAS* 461, 2003–2018.
- Zhang, J. et al. (2014). “Optical and Ultraviolet Observations of a Low-velocity Type II Plateau Supernova 2013am in M65”. *ApJ* 797, 5.
- de Jaeger, T. et al. (2015). “A Hubble Diagram from Type II Supernovae Based Solely on Photometry: The Photometric Color Method”. *ApJ* 815, 121.
- de Jaeger, T. et al. (2017a). “A Type II Supernova Hubble Diagram from the CSP-I, SDSS-II, and SNLS Surveys”. *ApJ* 835, 166.
- de Jaeger, T. et al. (2017b). “SN 2016jhh at redshift 0.34: extending the Type II supernova Hubble diagram using the standard candle method”. *MNRAS* 472, 4233–4243.
- de Jaeger, T. et al. (2018). “Observed Type II supernova colours from the Carnegie Supernova Project-I”. *MNRAS* 476, 4592–4616.
- de Vaucouleurs, G. et al. (1981). “The bright SN 1979 C in M 100.” *PASP* 93, 36–44.
- van Dokkum, P. G. (2001). “Cosmic-Ray Rejection by Laplacian Edge Detection”. *PASP* 113, 1420–1427.